STARS

Electronic Theses and Dissertations, 2004-2019

2012

Experimental Study And Modeling Of Mechanical Micro-machining Of Particle Reinforced Heterogeneous Materials

Jian Liu
University of Central Florida

Showcase of Text, Archives, Research & Scholarship

EXPERIMENTAL STUDY AND MODELING OF MECHANICAL MICRO-MACHINING OF
PARTICLE REINFORCED HETEROGENEOUS MATERIALS

by

JIAN LIU
B.S. China University of Mining and Technology, 2006
M.S. University of Central Florida, 2011

A dissertation submitted in partial fulfillment of the requirements
for the degree of Doctor of Philosophy
in the Department of Mechanical and Aerospace Engineering
in the College of Engineering and Computer Science
at the University of Central Florida
Orlando, Florida

Fall Term
2012

Major Professor: Chengying Xu

ABSTRACT

This study focuses on developing explicit analytical and numerical process models for mechanical micro-machining of heterogeneous materials. These models are used to select suitable process parameters for preparing and micro-machining of these advanced materials. The material system studied in this research is Magnesium Metal Matrix Composites (Mg-MMCs) reinforced with nano-sized and micro-sized silicon carbide (SiC) particles.

This research is motivated by increasing demands of miniaturized components with high mechanical performance in various industries. Mg-MMCs become one of the best candidates due to its light weight, high strength, and high creep/wear resistance. However, the improved strength and abrasive nature of the reinforcements bring great challenges for the subsequent micro-machining process.

Systematic experimental investigations on the machinability of Mg-MMCs reinforced with SiC nano-particles have been conducted. The nanocomposites containing 5 Vol.%, 10 Vol.% and 15 Vol.% reinforcements, as well as pure magnesium, are studied by using the Design of Experiment (DOE) method. Cutting forces, surface morphology and surface roughness are characterized to understand the machinability of the four materials. Based on response surface methodology (RSM) design, experimental models and related contour plots have been developed to build a connection between different materials properties and cutting parameters. Those models can be used to predict the cutting force, the surface roughness, and then optimize the machining process.

An analytical cutting force model has been developed to predict cutting forces of Mg-MMCs reinforced with nano-sized SiC particles in the micro-milling process. This model is

different from previous ones by encompassing the behaviors of reinforcement nanoparticles in three cutting scenarios, i.e., shearing, ploughing and elastic recovery. By using the enhanced yield strength in the cutting force model, three major strengthening factors are incorporated, including load-bearing effect, enhanced dislocation density strengthening effect and Orowan strengthening effect. In this way, the particle size and volume fraction, as significant factors affecting the cutting forces, are explicitly considered. In order to validate the model, various cutting conditions using different size end mills (100 μm and 1 mm dia.) have been conducted on Mg-MMCs with volume fraction from 0 (pure magnesium) to 15 Vol.%. The simulated cutting forces show a good agreement with the experimental data. The proposed model can predict the major force amplitude variations and force profile changes as functions of the nanoparticles' volume fraction.

Next, a systematic evaluation of six ductile fracture models has been conducted to identify the most suitable fracture criterion for micro-scale cutting simulations. The evaluated fracture models include constant fracture strain, Johnson-Cook, Johnson-Cook coupling criterion, Wilkins, modified Cockcroft-Latham, and Bao-Wierzbicki fracture criterion. By means of a user material subroutine (VUMAT), these fracture models are implemented into a Finite Element (FE) orthogonal cutting model in ABAQUS/Explicit platform. The local parameters (stress, strain, fracture factor, velocity fields) and global variables (chip morphology, cutting forces, temperature, shear angle, and machined surface integrity) are evaluated. Results indicate that by coupling with the damage evolution, the capability of Johnson-Cook and Bao-Wierzbicki can be further extended to predict accurate chip morphology. Bao-Wierzbiki-based coupling model provides the best simulation results in this study.

The micro-cutting performance of MMCs materials has also been studied by using FE modeling method. A 2-D FE micro-cutting model has been constructed. Firstly, homogenized material properties are employed to evaluate the effect of particles' volume fraction. Secondly, micro-structures of the two-phase material are modeled in FE cutting models. The effects of the existing micro-sized and nano-sized ceramic particles on micro-cutting performance are carefully evaluated in two case studies. Results show that by using the homogenized material properties based on Johnson-Cook plasticity and fracture model with damage evolution, the micro-cutting performance of nano-reinforced Mg-MMCs can be predicted. Crack generation for SiC particle reinforced MMCs is different from their homogeneous counterparts; the effect of micro-sized particles is different from the one of nano-sized particles.

In summary, through this research, a better understanding of the unique cutting mechanism for particle reinforced heterogeneous materials has been obtained. The effect of reinforcements on micro-cutting performance is obtained, which will help material engineers tailor suitable material properties for special mechanical design, associated manufacturing method and application needs. Moreover, the proposed analytical and numerical models provide a guideline to optimize process parameters for preparing and micro-machining of heterogeneous MMCs materials. This will eventually facilitate the automation of MMCs' machining process and realize high-efficiency, high-quality, and low-cost manufacturing of composite materials.

To: my parents Liu Hongchao and Cai Guilan

and my wife Li Juan

ACKNOWLEDGMENTS

First and foremost, I would like to acknowledge and extend my sincere appreciation to my advisor Dr. Chengying Xu. Her guidance, patience, continuous encouragement and steady support have led me go through the most difficult stages during completing this dissertation research. I am deeply influenced and motivated by her passion, dedication, commitment and endurance. My appreciation also goes to Dr. Qiang Liu at the Beihang University for bringing me into the machining research area.

Besides my advisors, I would like to thank Dr. Linan An, Dr. Yuanli Bai, Dr. Ali P. Gordon and Dr. Xun Gong for serving on my examination and advisory committee and for providing me with ample guidance. I must thank them for answering any questions I had and spending time reviewing the manuscript. Their valuable insights have helped me think through research problems from different perspectives.

I am cordially grateful to Professor Tony Atkins for helpful discussions on the modeling of cutting processes. Moreover, help from Dr. Xiaoqing Teng in developing VUMAT material subroutines is greatly appreciated. My gratitude also goes to Dr. David Nicholson, Dr. Alain Kassab, Dr. Quanfang Chen, Dr. Olusegun Ilegbusi, Dr. Vaidyanathan Raj, Dr. Weiwei Deng, Dr. Wenwu Zhang and Dr. Xinyu Liu, for their helpful discussions and suggestions.

My appreciation also goes to all MMAE staff for their assistance throughout my study at UCF. I gratefully acknowledge the technical support from the Institute of Simulation & Training and the Materials Characterization Facility at UCF. My thanks also go to the Dassault Systèmes for providing Abaqus software, and the Altair Company for the continuous support with HyperMesh. Moreover, I would like to acknowledge the financial support from the Department

I have been fortunate to work with all my colleagues and friends in Reconfigurable Intelligent Systems Engineering Lab, especially Dr. Yan Tang, Dr. Randal Allen, Andrew Joslin, and Kevin Knipe, who helped me immensely in many ways. Additionally, I would like to thank all my friends, without whom my time over the years would not have been as interesting, educational and meaningful.

Last, but by no means least, my heartful gratitude goes to my parents and my wife. Their unconditional love and tremendous support have continuously encouraged me to achieve better and live a full life.

TABLE OF CONTENTS

LIST OF FIGURES

LIST OF TABLES

LIST OF NOMENCLATURE

f_t feed per tooth (µm/tooth)

d_a depth of cut (µm)

λ inter-particle spacing (µm)

d average particle size (µm)

V_f volume fraction (Vol.%)

G_m shear modulus of the matrix (GPa)

t_c uncut chip thickness (µm)

κ overall elastic recovery rate (%)

R micro end mill radius (µm)

t_{min} minimum chip thickness (mN)

t_{er} minimum elastic recovery thickness (mN)

A_p ploughing area (µm^2)

σ_{ys} reinforced yield strength of MMCs composites (MPa)

σ_{ym} yield strength of matrix material (MPa)

f_l improving factor due to load-bearing effect

f_d improving factor due to enhanced dislocation density effect

f_O improving factor due to Orowan effect

b magnitude of the Burgers vector of dislocation in the matrix

α_m coefficient of thermal expansion of matrix (µm.m/K)

α_p coefficient of thermal expansion of reinforcement (µm.m/K)

θ_s start immersion angle (rad)

θ_e exit immersion angle (rad)

L_c length of ploughed area (µm^2)

N number of teeth of end mill

r_e cutting tool edge radius (μm)

ψ_e cutting tool clearance angle (rad)

α_p cutting tool rake angle (rad)

ψ_t cutting tool geometric angle (rad)

ψ_s cutting tool geometric angle (rad)

β helical angle of end mill ($^\circ$)

F_t tangential force in local coordinates (mN)

F_r radial force in local coordinates (mN)

F_a axial force in local coordinates (mN)

F_{rRVE} radial force due to strengthening effects (mN)

F_{tRVE} tangential force due to strengthening effects (mN)

F_x cutting force in X direction in global coordinates (mN)

F_y cutting force in Y direction in global coordinates (mN)

F_z cutting force in Z direction in global coordinates (mN)

K_{te} tangential force coefficient in the elastic recovery zone (MPa)

K_{re} radial force coefficient in the elastic recovery zone (MPa)

K_{ae} axial force coefficient in the elastic recovery zone (MPa)

K_{tp} tangential force coefficient in the ploughing zone (MPa)

K_{rp} radial force coefficient in the ploughing zone (MPa)

K_{ap} axial force coefficient in the ploughing zone (MPa)

K_{ts} tangential force coefficient in the shearing zone (MPa)

K_{rs} radial force coefficient in the shearing zone (MPa)

K_{as} axial force coefficient in the shearing zone (MPa)

T_{room} room temperature (˚C)

T_{melt} melting temperature (˚C)

ρ density (kg/m^3)

E elastic modulus (GPa)

v Poisson's ratio

C_p specific heat (J/kg ˚C)

λ thermal conductivity (W/m˚C)

α_d coefficient of thermal expansion (μm.m/˚C)

μ friction coefficient

τ_{crit} critical shear stress (MPa)

$\bar{\varepsilon}_f^{pl}$ plastic strain to failure

$\bar{\varepsilon}^{pl}$ equivalent plastic strain

D damage parameter

D_{cr} critical damage parameter

η triaxiality (a dimensionless pressure deviatoric stress ratio)

p pressure stress (MPa)

q Von Mises stress (MPa)

G_f Hillerborg's fracture energy

L characteristic length of the element

$\bar{u}_f$ equivalent plastic displacement after the onset of damage initiation

K_{IC} mode I fracture toughness (MPa $\sqrt{mm}$)

K_{IIC} mode II fracture toughness (MPa $\sqrt{mm}$)

K_{IIIC} mode III fracture toughness (MPa $\sqrt{mm}$)

σ_1 normalized maximum principal stress (MPa)

CHAPTER 1   INTRODUCTION

1.1 Background and Motivation

In numerous fields that include aerospace, energy, automobile, medical and optics, requirements of tough mechanical properties and miniaturized sizes become more and more demanding. Specific applications include avionics packaging, micro-fluidic channels for lab-on-chips and fuel cells, micro-scale holes for fiber optics, micro-nozzle array for multiplexed electrospray systems, micro-molds, micro sensors and actuators [1-6].

Metal Matrix Composite materials (MMCs) have been applied in numerous fields that include energy, defense, aerospace, bio-technology, optics and automobile, because of their reinforced high performance mechanical properties and reduced weight. In recent decades, substantial progress has been achieved in the development of MMCs. This enables the advanced heterogeneous materials to be considered in more applications. Some large scale application examples of MMCs are shown in Figure 1.1. These applications require outstanding mechanical properties, including light weight, high strength, high creep resistance, long fatigue life, high corrosion/oxidation resistance, low thermal expansion and good wear resistance. The energy efficiency will be dramatically improved as the MMCs are widely applied in these fields.

(a)	(b)	(c)
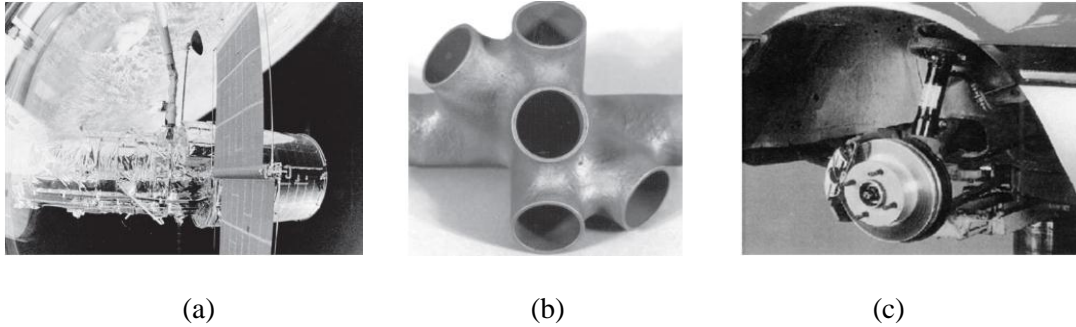
Figure 1.1: Macro-scale applications of advanced MMCs: (a) The P100/6061 Al high-gain antenna wave guides/boom deployed in the Hubble Space Telescope (HST) [4]; (b) Cast SiCp/Al multi-inlet fitting for a truss node [4]; (c) Vented passenger car brake disk [1];

On the other side, emerging miniaturization technologies are perceived as key technologies of the future in a broad spectrum of applications [2, 3]. Due to the high surface-to-volume ratio, miniature components can provide lower power consumption, higher heat transfer, and are more flexible and efficient. Using miniature components under appropriate circumstances can further improve energy efficiency. Figure 1.2 shows some micro/meso-scale applications which demand the miniaturized mechanical features in the range of a few hundred micros to several millimeters. Both the small size and excellent mechanical properties are required in these applications.

(a)	(b)	(c)
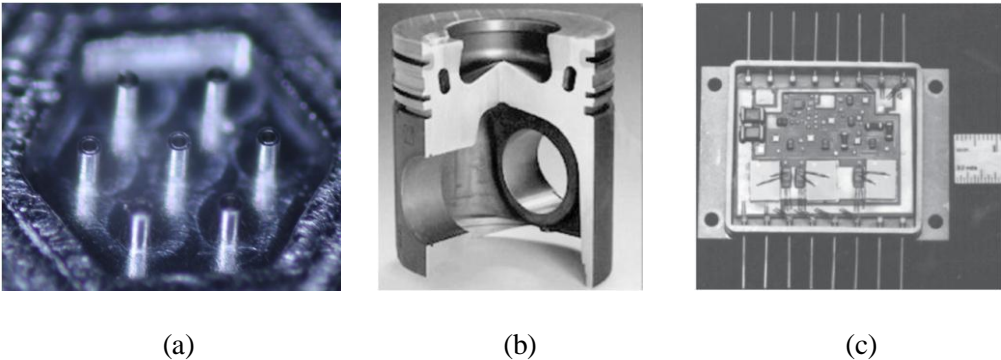
Figure 1.2: Micro-scale applications of advanced MMCs for: (a) micro machined electrospray atomizers (hole inner diameter 50 μm fabricated in RISE lab); (b) Partial short fiber reinforced light metal diesel pistons [1]; (c) SiCp/Al electronic package for a remote power controller applied in communication satellites [4];

In aforementioned applications, both the small size and outstanding mechanical properties are required. Ceramic particle-reinforced Metal Matrix Composites, such as Aluminum-based MMCs (Al-MMCs) or Magnesium-based MMCs (Mg-MMCs), with light weight and high toughness, are excellent candidates for making components for such applications. Thanks to the hard ceramic particles reinforcement, the mechanical properties are improved significantly. It was found that these composites exhibit much better mechanical properties such as higher strength and superior wear resistance than pure Mg/Al and their alloys [7-9].

There exist a number of different fabrication methods to make miniaturized components, made of ceramic-reinforced MMCs. Since components made of advanced MMC materials usually contain complex 3-Dimensional (3-D) features, the traditional silicone based fabrication methods for micro-electro-mechanical systems (MEMS) are not adequate. Several micro-machining methods have been reported in literature for SiC reinforced MMCs. Müller *et al.* [10] studied the capability of manufacturing SiC particle-reinforced aluminum matrix composites using electrical discharge machining (EDM) method. The results showed that the removal rate was low due to the poor electrical conductivity of SiC particles. In addition, electrode wear was severe and thus inevitably increased the manufacturing cost. Laser machining is another alternative method and is capable of making small diameter holes and cutting metal matrix composites. However, the surface quality was relatively poor and the microstructure of materials was changed under the effect of laser heating [11].

Compared to the above methods, the mechanical micro-machining process is promising to mass produce MMCs parts. This approach is cost-effective, flexible, and controllable, precise

(relative accuracy as $10^{-3} \sim 10^{-5}$), and capable to make arbitrary 3-D pattern [2, 10, 11]. Using micro-machining technique, small components can be manufactured more efficiently with lower cost and higher quality.

However, the remarkably enhanced mechanical properties of MMCs, in terms of yield strength, fracture strength, wear resistance and shear modulus bring great challenges for mechanical micro-machining. Comparing with micro-machining homogeneous metals, cutting forces when machining MMCs are much larger due to the existence of the ceramic particle reinforcement. Tool wear is more severe and tool life is shortened. Due to the elevated cutting force amplitude, tool vibration and tool deflection are more significant. As a result, both dimensional accuracy and surface quality are adversely affected. In order to achieve good machining efficiency and quality, it's important to fully understand the strengthening mechanism and the influence of reinforcement particles on the entire micro-cutting process, especially the chip formation process.

1.2 Objectives of This Research

The objective of this research is to establish explicit process models connecting the controllable input cutting conditions with output variables (e.g., cutting forces, tool deflections and machined surface roughness) for advanced heterogeneous Mg-MMCs materials during micro-endmilling process. Using these models, based on input cutting conditions for specific Mg-MMCs materials, the machining performance can be predicted in terms of cutting forces, tool deflections, machined surface integrity and cycle time. To this end, comprehensive process

models of micro milling the heterogeneous materials will be constructed. Since the cutting performance is strongly affected by unique cutting mechanisms in both the macro-scale and micro-scale levels, a thorough understanding of the cutting mechanisms in different scales is highly required.

Figure 1.3 illustrates the relationships among material properties, strengthening mechanisms and cutting mechanisms in different scales during mechanical micro-machining.

In the micro-scale level, the fundamental microstructure and strengthening mechanisms of the MMCs establish the foundation for cutting mechanics and dynamics. Core research topics involve mechanical properties and fracture mechanisms of the material.

In the meso-scale level, fundamental chip formation mechanism is different from traditional machining and micro-machining of homogeneous materials due to the effect of heterogeneity, size effect and the minimum chip thickness effect etc. The influence of material's microstructure and strengthening mechanism on chip formation is the key. The fundament of heterogeneous material removal mechanism further establishes the foundation for differentiating cutting regimes in macro-scale level. The chip formation modeling involves material micro-structural effect, strengthening effect, tool edge radius effect, size effect, and minimum chip thickness effect; it is built to further predict dynamic cutting force during machining.

In the macro-scale level, the research should focus on modeling the process states including cutting forces and tool vibration, as well as the final machined surface integrity in terms of dimensional accuracy and surface roughness.
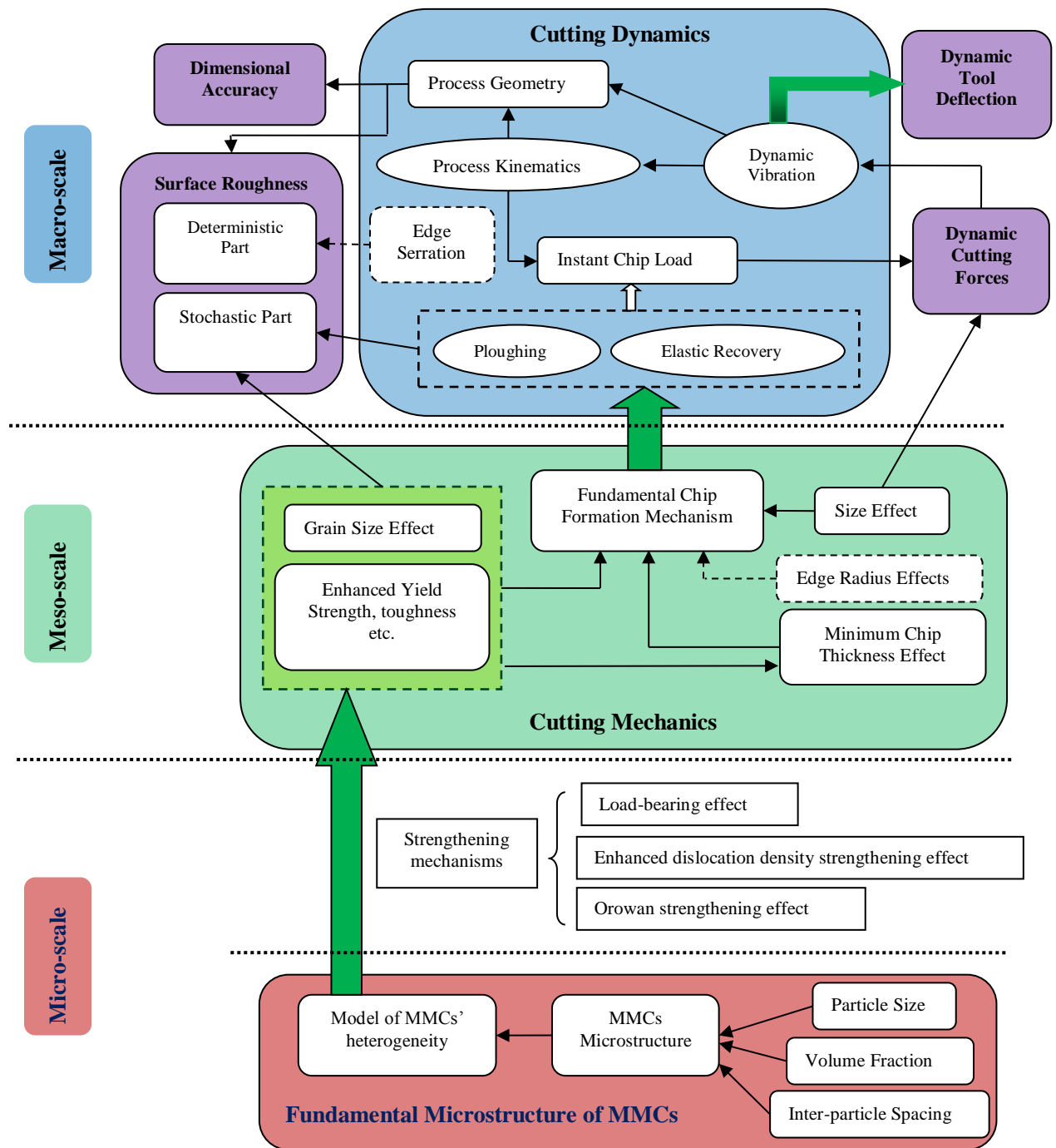
Figure 1.3: Schematic of the interrelationship among the cutting mechanisms in different scales

The research specially focuses on modeling material removal process and related process states, including cutting forces and machined surface integrity in terms of dimensional accuracy and surface roughness. The micro end mill's diameter ranges from 100 μm to 1000 μm. Due to the innovativeness of the Mg-MMCs materials, experimental machinability study is conducted in the first step. Based on the experimental study, the phenomena that are fundamentally different from micro milling homogeneous materials are revealed.

The objective of this dissertation research is realized through the following specific studies:

a) Micro-Machinability Study on Mg-MMCs: The objective is to investigate the machinability of Mg-MMCs with micro-endmilling method. A better understanding of machining characteristics for Mg-MMCs has been obtained. Using Design of Experiment (DOE) method, the effects of the reinforcements' volume fraction and particle size on cutting forces as well as machined surface roughness are systematically studied. Experiments are conducted on samples of Mg-MMCs with 5 Vol.%, 10 Vol.% and 15 Vol.% reinforcements of SiC nano-particles and pure Magnesium. Different feedrates and spindle speeds are chosen as varied cutting parameters. Cutting forces, surface morphology and roughness are measured and evaluated to understand the machinability of the four different materials during the micro-milling process.

b) Modeling of Dynamic Cutting forces: The analytical dynamic cutting force model consists three parts:

☐ Instantaneous chip load model – The tool tip trajectory in micro-endmilling is not an ideal trochoidal path due to the material heterogeneity, tool vibration and

deflection. The influences of above factors on the instantaneous chip thickness are even greater than the nominal uncut chip thickness under certain circumstances. Therefore, an instantaneous chip thickness model should be constructed by considering the tool runout, tool deflection and the unique cutting regime switching mechanism for Mg-MMCs.

☐ Cutting force model – The cutting force model of Mg-MMCs is developed from using differential forms of tangential, radial and axial force. Based on the chip formation study, behaviors of the reinforcement particles can be reflected in the three cutting regimes, i.e., shearing, ploughing and elastic recovery. The validated model can be used to study the effects of the materials' properties on the cutting forces.

☐ Calibration algorithm – Cutting force tests using different nominal chip load have been conducted in order to calibrate the proposed cutting force model. Root Mean Square (RMS) average cutting forces is used to calculate the specific cutting energies and the cutting force constants for a specific nominal chip load.

c) Effects of Fracture Models: A systematic evaluation of six ductile fracture models is conducted to identify the most suitable fracture criterion for micro-scale machining problems based on Finite Element (FE) modeling method. The objective is to establish the most suitable ductile fracture models for micro-cutting simulations. The evaluated fracture models include the constant fracture strain, the Johnson-Cook, the Johnson-Cook coupling criterion, the Wilkins, the modified Cockcroft-Latham, and the Bao-Wierzbicki fracture models. By means of a user material subroutine (VUMAT) in ABAQUS/Explicit platform, these fracture models are

implemented into a Finite Element (FE) model of orthogonal cutting process. The local parameters (stress, strain, temperature, velocity fields) and global variables (chip morphology, cutting forces, shear angle, machined surface integrity) are evaluated. The numerical simulation results have been examined by comparing with experimental results published in open literatures.

d) Chip Formation Mechanism Study on Mg-MMCs: The fundamental material removal mechanism and micro-cutting performance of Mg-MMCs materials are studied by using FE modeling method. A 2-D FE micro-cutting model has to be constructed and a simulation study is achieved in this research. Firstly, homogenized material properties are employed to evaluate the effect of volume fraction. Secondly, micro-structures of the two-phase material are modeled in FE cutting models. The effects of the existing micro-sized and nano-sized ceramic particles on micro-cutting performance are carefully evaluated in two simulation case studies. The fundamental chip formation model is the foundation to study the effects of material properties on cutting process. Moreover, it can bridge the micro-level behaviors of the material with the meso and macro level cutting performance.

Based on the process models, the productivity, machined surface integrity, and tool life can be improved through optimizing the cutting conditions for a specific Mg-MMCs composite materials.

1.3 Dissertation Outline

The reminder of this dissertation is organized as follows.

Chapter 2 contains a review and analysis of the literature related to metal matrix composite machining and micro milling process. In Chapter 3, a systematic micro-machinability study on Mg-MMCs materials is conducted and analyzed based on Design of Experiment (DOE) method. Chapter 4 includes the cutting force model which accounts for the effect of materials' volume fraction and particle size. The behaviors of nanoparticles have been defined in this model and the proposed cutting force model is validated by comparing the simulation cutting forces and experimental measurements using a 100 μm diameter end mill and a 1 mm diameter end mill. Chapter 5 focuses on the effects of different fracture models on cutting matrix materials. This study will facilitate the utilization of proper fracture models in MMC's numerical cutting simulation. Chapter 6 exhibits numerical cutting simulation study for Mg-MMCs with SiC reinforcements. Homogenized materials property and heterogeneous materials' properties are considered as case studies, and the unique cutting mechanisms for Mg-MMCs are analyzed through the simulation studies. Chapter 7 concludes this research and points out the recommended future research directions.

CHAPTER 2   LITERATURE REVIEW

This chapter surveys the state of the art of micro-machining technology and its application for heterogeneous materials' fabrication. In general, the principles of micro-machining are similar to those of macro-scale machining; however micro-machining exhibits different characteristics due to the significantly reduced size. Thorough understanding the tool-workpiece interaction mechanism and the chip formation physics will facilitate the modeling work of the entire micro-cutting process. With this purpose, this chapter specifically focuses on the interaction of the cutting tools and the ceramic-reinforced MMCs. Various effects in micro-scale perspective should be considered when modeling the micro-machining process, including material's heterogeneity, size effect, minimum chip thickness effect, tool edge roundness and tool runout.

2.1 Ceramic-reinforced Metal Matrix Composites

2.1.1 Mechanical Properties

Ceramic-reinforced Metal Matrix Composites (MMCs) have potential to replace conventional light-weight metallic materials such as magnesium, aluminum, titanium and their alloys due to the reinforced high mechanical performance including higher yield strength, fracture strength, toughness, lower thermal expansion, higher creep resistance and wear

resistance. In comparison to pure metal materials, the engineered composites display higher stiffness, strain hardening, and strength, with lower strain to fracture [1].

Previous studies primarily focused on the use of micro-sized reinforcements or low volume fractions (< 2 Vol.%) of nano-sized reinforcements, mostly in aluminum matrix [1]. It is revealed that the composites reinforced with nano-sized particles exhibit better properties than those reinforced with micro-sized reinforcements. Nano-reinforcements can remarkably increase the mechanical strength by effectively promoting particle hardening mechanisms. A fine and uniform dispersion of nano-particles provides a good balance between the ceramic strengthener (non-deforming particles) and inter-particle spacing effects to maximize the yield strength and creep resistance while retaining good matrix ductility [12-14]. Recent experiments demonstrated that MMCs with a high volume fraction of nano-particles exhibit better mechanical behaviors than those reinforced with micro-sized particles, and those with low volume fractions of nano-sized reinforcements. Through our previous research, we found that aluminum matrix nanocomposites containing 15 Vol.% alumina nano-particles of 50 nm exhibit better wear resistance than stainless steel [15]. The impact strength of this composite is greater than 1 GPa, which is sufficient for lightweight armor applications [16].

Researchers have investigated the effect of micro-sized reinforcement particles on the mechanical properties of the MMCs [1, 9, 17]. Lim *et al.* [9] studied the wear behavior of the Mg-MMCs reinforced by SiC particles with a nominal size of 14 μm. Charles *et al.* [17] investigated the mechanical behavior of Al-MMCs at cryogenic temperatures.

As novel nanoparticle-reinforced MMCs show improved mechanical performances, such as higher yield strength and creep resistance, comparing to their micro-composite counterparts,

researchers began to move their interests further to nano-particulate MMCs. Different matrix materials were studied including Magnesium [18-21], Aluminum [22] and Copper [23]. The investigated reinforcement nanoparticles include SiC [18], Alumina [20], MgO/MgO$_2$ [8] and even Ti$_2$AlC [21]. Tjong summarized and reviewed the processing methods, micro-structures and mechanical properties of MMCs reinforced with nano-sized ceramic particles [24].

As the lightest construction/structural metal materials at present, Magnesium and its alloys have gained adequate attention in research. Reddy *et al.* [18] first reported Mg-MMCs using SiC particulates in sub-micron length scale. In this study, the micro-structural, physical and mechanical properties of pure magnesium reinforced with different volume fractions of 0.6 μm SiC particles were studied. The Mg-MMCs were synthesized using disintegrated melt technique. The characterization results are shown in Table 2.1. The microscopic views showing the distribution of the particles in matrix materials are displayed in Figure 2.1.

Table 2.1: Results of acid dissolution, density, porosity and grain size measurements [18]

Material	Reinforcement		Density (g/cm3)	Porosity (Vol. %)	Characteristics of grains		Characteristics of SiC particulates	
	Wt. %	Vol. %			Size (μm)	Aspect ratio	Size (μm)	Aspect ratio
Mg	---	---	1.7380±0.0020	0.12	21±6	1.8±0.41	---	---
Mg/SiC	4.8	2.7	1.7698±0.0236	0.53	18±6	1.9±0.40	0.57±0.04	1.2±0.1
Mg/SiC	10.2	5.8	1.7931±0.0019	1.75	17±7	1.8±0.21	0.58±0.02	1.1±0.1
Mg/SiC	15.4	9.0	1.8349±0.0163	1.98	12±4	1.4±0.11	0.58±0.02	1.1±0.1
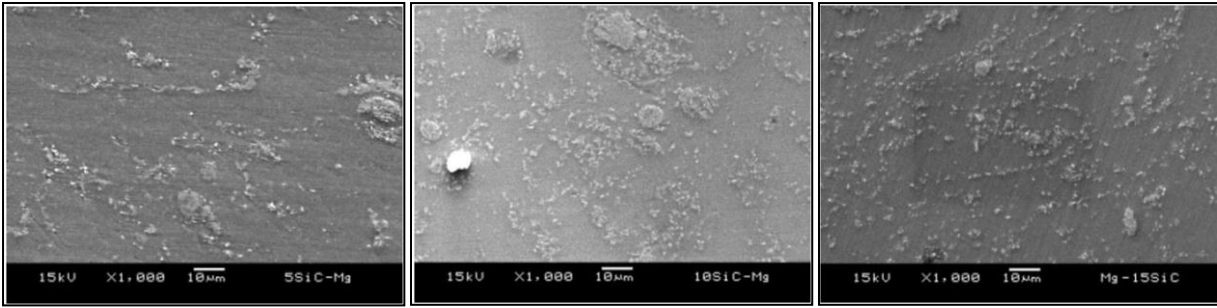
<div align="center">(a)   (b)   (c)</div>

Figure 2.1: SEM micrographs showing the distribution of reinforcement in: (a) Mg/4.8 wt% SiC; (b) Mg/10.2 wt% SiC; (c) Mg/15.4 wt% SiC [18]

Cao *et al.* [19] investigated the mechanical properties and microstructure of Mg-SiC nanocomposites fabricated by ultrasonic cavitation to disperse SiC nanoparticles in Mg melts. The average size of SiC particles used in this study is 50 nm. The mechanical properties are shown in Table 2.2. The microstructures of the fabricated Mg-MMCs are shown in Figure 2.2. It indicates that most of the SiC nanoparticles were dispersed well locally, with extinct SiC micro-clusters. Table 2.3 shows result for Mg-MMCs with higher content of SiC nanoparticles [18], where the percentage value in the first column represents the weight ratio of SiC nanoparticles in the matrix of Mg-MMCs nanocomposites.

<div align="center">Table 2.2: Average mechanical properties [19]</div>

Materials	Yield strength (MPa)	Ultimate tensile strength (MPa)	Ductility/Elong. (%)
Pure Mg	20.0	89.6	14.0
Mg/0.5% SiC	28.3	120.7	15.5
Mg/1.0% SiC	30.3	124.1	14.2
Mg/2.0% SiC	35.9	131.0	12.6
Mg/4.0% SiC	47.6	106.9	5.5

Table 2.3: Mechanical properties measured at ambient room temperature [18]

Material	Young's Modulus E (GPa)	0.2% Yield Stress (MPa)	UTS (MPa)	Ductility (%)
Mg	39.82	153 ±8	207 ±4	9.2 ±1.4
Mg/4.8SiC	45.60	182 ±2	219 ±2	2.1 ±0.9
Mg/10.2SiC	47.22	171 ±3	221 ±14	1.5 ±0.2
Mg/15.4SiC	48.24	155 ±1	207 ±9	1.4 ±0.1
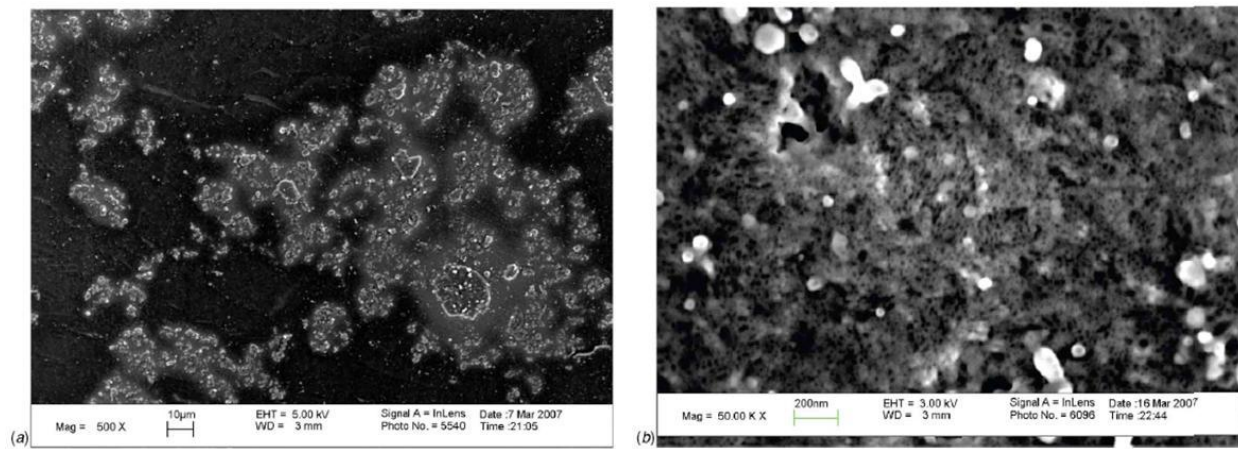
Figure 2.2: SEM images of Mg/2 wt% SiC nanocomposite: (a) lower magnification and (b) higher magnification [19]

According to the literature, the volume fraction of the Mg-MMCs using SiC as reinforcement is limited approximately around 10 Vol.%. There is very little literature regarding higher volume fraction MMCs with nano-reinforcements, especially for Mg-based nanocomposites [16]. The main reason is because it is very difficult to mix more SiC nano-particles into the matrix metal uniformly. Different mechanical property aspects, such as elasticity, plasticity and fracture strength, exhibit different trends as volume fraction varies. Also, MMCs reinforced with various sizes of nano particles behave differently in mechanical

properties. Therefore, the study on the effect of particle size and volume fraction on the material properties is important and explicit models are needed.

2.1.2 Fracture Mechanism of MMCs

In order to understand the cutting mechanism of ceramic-reinforced MMCs, it's critical to understand the materials' fracture mechanism. From the perspectives of fracture mechanics and computational mechanics, researchers have dedicated effort in modeling the fracture behavior, crack damage evaluation and interface damage for MMCs.

For particle-reinforced MMCs, classical plasticity theory cannot be directly applied, because the composites exhibit a tension-compression yield asymmetry due to the variation of damage evolution with loading modes [25]. Zhang *et al.* [25] proposed a viscoplastic multi-axial constitutive model for plastic deformation of MMCs using the Mises-Schleicher yield criterion, which is capable of describing the multi-axial yield and flow behavior of MMCs by using asymmetric tensile and compressive stress-strain responses as input. Biner and Hu [26] proposed a phase-field model to describe the damage evaluation, due to particle cracking in particle reinforced MMCs. In this model, the metal matrix deformation is described by using elastic-plastic constitutive law including linear hardening behavior. Comparing to conventional models, such as constitutive models of void growth and cohesive zone models, the experimentally validated phase-field model that they proposed has the advantage to describe the microstructure and topological changes related to damage evaluation.

Aiming at assessing microscale stress sates of MMCs under high plastic strain conditions, which are typical for high-temperature forming process, Ilie *et al.* [27] introduced a multi-scale

16

Finite Element (FE) modeling approach and two model types to analyze the extrusion of Al-SiC MMCs. The microscale model explicitly embraced the heterogeneous micro-structures of the material, while the macroscale model was used to simulate the extrusion process of the MMCs, which was modeled as homogeneous continuum at this level. Using the proposed multi-scale model, the predicted macroscale plastic strain distributions and pressures can be used to evaluate the risk of damage in the materials during forming process. Aghdam *et al.* [28] developed a three-dimensional micromechanical Finite Element Analysis (FEA) model to study the interface damage of unidirectional SiC/Ti MMCs under hybrid thermal and axial shear loading. By introducing a suitable failure criterion for interface damage, the predicted stress-strain curve demonstrated better agreement with experimental data than predictions based on perfectly bonded and fully de-bonded interface. The interface damage study was also conducted for off-axis loading in their later work [29].

Experimentally, Xia *et al.* [30] studied the fracture behavior of MMCs reinforced with micro-sized (15~30 μm) ceramic particles. Different volume fractions (5%~20%), reinforcements (alumina and SiC) and matrix materials (2618, 6061 and 7075 Al) were examined under three point bending tests. Results revealed that the energy absorption level during the crack propagation depended on both matrix strength and ductility. The latter property related to the volume fraction, composition and heat treatment conditions. Similar experimental study was also performed by Rabiei *et al.* [31], who evaluated the fracture toughness of Al-MMCs with various particle reinforcements. Hahn Rosenfield model was used to estimate theoretical fracture toughness. Since the Hahn Rosenfield model is only valid for predicting the fracture toughness of MMCs with 5 ~ 10 μm particle reinforcements, a modification to this model was developed

for estimating the fracture toughness of the MMCs with larger sizes of particle reinforcements (up to 20 μm).

According to the above modeling and experimental studies, the stress-strain behavior, interface damage or fracture responses can be predicted; however the investigated loading conditions in these literatures were far from reality of true material removal for machining processes.

2.1.3 Machinability Study of MMCs

The aim of manufacturing is to achieve near net shape components with required strength and functions. Even though MMCs are generally processed near net shape, further machining operations are usually inevitable to ensure the correct function for application. In this section, a number of experimental studies on MMCs' machinability are reviewed. The influences of machining conditions, e.g., cutting speed, feed speed and depth of cut, on various aspects of the machinability are evaluated. Important factors of machinability include cutting forces, chip formation, built-up edges (BUEs), surface integrity, shear/friction angles and residual stress.

Different cutting tools, including tungsten carbide (WC) inserts [32] and PCD inserts [33] re used to conduct experimental investigations on the machinability of SiC particulate Al-MMCs in turning operations. Another experimental study for Al-MMCs [34] focused on evaluating the chip compression ratio, chip formation, friction angle, shear angle, normal and shear stress under different cutting conditions.

Kannan *et al.* [35] carried out research to understand the role of ductile matrix on the machining performance by estimating line defects (Figure 2.3), resulting from turning operation for alumina reinforced Al-MMCs. The ceramic particle size was in micro-level.
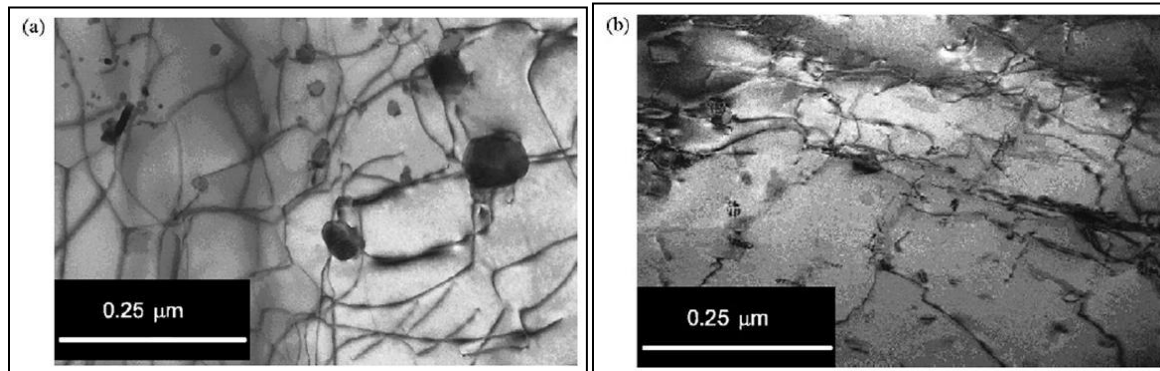
Figure 2.3: Nature of line defects in the two different matrix materials: (a) Al-7075/10% alumina MMC and (b) Al-6061/10% alumina MMC [35]

Pramanik *et al.* [36] experimentally studied the effects of reinforcement particles on the machining performance of Al-MMCs. The SiC particles' average size is 6~18 μm. The experiments were carried out using a bar turning process under dry conditions. The effect of ceramic particles on cutting forces, surface roughness, residual stress, chip shape, shear angles and friction angles were examined. From the results, complex variation of force profiles for the Al-MMCs was observed and possible reasons were summarized to be: (a) different work hardening properties, (b) fracture at the shear plane and tool chip interface for MMC, (c) different thermal softening behaviors, (d) tool-particle interaction for MMCs, and (e) different effects of strain and strain rate on forces of these materials. Pramanik *et al.* [37] also proposed a mechanistic model for predicting the average cutting forces in turning MMCs reinforced with

SiC or Al_2O_3 particles. The forces were categorized into three aspects, including the chip formation force, the ploughing force and the particle fracture force.

Since the cutting mechanisms are not well understood yet for MMCs, the experimental study to reveal the nature of MMCs' cutting behavior demands a large number of cutting tests. In order to improve the efficiency of the experimental study and extract more information from the experimental results analysis, Design of Experiments (DOE) methods have been widely applied to study the machinability of MMCs. Taguchi method-based experimentation studies were carried out to analyze the machinability of Al-MMCs [38, 39]. A Taguchi method was also applied to study the drilling of hybrid MMCs [40]. Besides, Response Surface Methodology (RSM) was effective to study the effects of cutting conditions on cutting forces [41] and surface roughness [42].

Machinability studies on micro-reinforced MMCs have been experimentally developed to a mature stage, especially on conventional turning operation for Al-MMCs. Currently, there are a number of companies who are commercializing the Al-MMCs. However, there is little literature on the machinability of nano-reinforced MMCs. Therefore, the micro-machinability study on the Mg-MMCs reinforced with nano-sized ceramic particles is greatly needed in this field.

2.2 Cutting Process Mechanism

2.2.1 Material's Micro-structural Effect

During micro-milling, the micro-structural nature of the workpiece materials must be considered in order to achieve high surface quality. The crystalline grain size of the most

commonly used engineering materials suitable for micro-machining is between 100 nm and 100 μm [43]. These crystalized materials such as aluminum, copper, steel and titanium etc. have broad engineering applications. The order of magnitude overlaps with the feature size in micro-machining. Moreover, the tool edge radius (roundness) and preferred feed per tooth value are often designed from several hundreds of nanometers to several micro meters, which is also comparable to the crystalline grain size. Therefore, the effect of the crystallographic properties on overall cutting performances plays an important role in micro-machining.

Vogler *et al.* [44] proposed a micro-structural mapping based on finite element (FE) simulation (Figure 2.4) and studied the effect of metallurgical phases on cutting forces. Comprehensive literature studies regarding the grain size effect of traditional polycrystalline materials, such as steel, aluminum, etc., were conducted in [3, 43]. Chuzhoy *et al.* [45-47] proposed a FE model for the orthogonal cutting of ductile iron. In this study, the different phases of the iron, including ferrite and pearlite, were explicitly modeled with different constitutive models. The proposed model was capable to compute stress, strain, temperature and damage distributions as well as the size of fracture and decohesion zones. Figure 2.5 shows the accumulated damage during the FE simulation. The grain size in this study is around tens of micrometers.
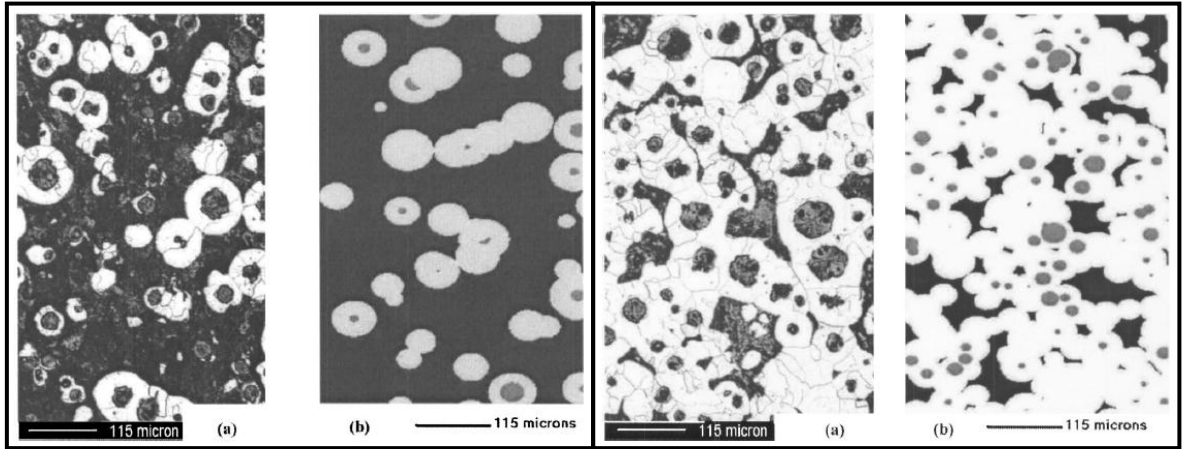
Figure 2.4: (a) Actual and (b) simulated microstructures of pearlitic (left) and ferritic ductile iron (right) [44]
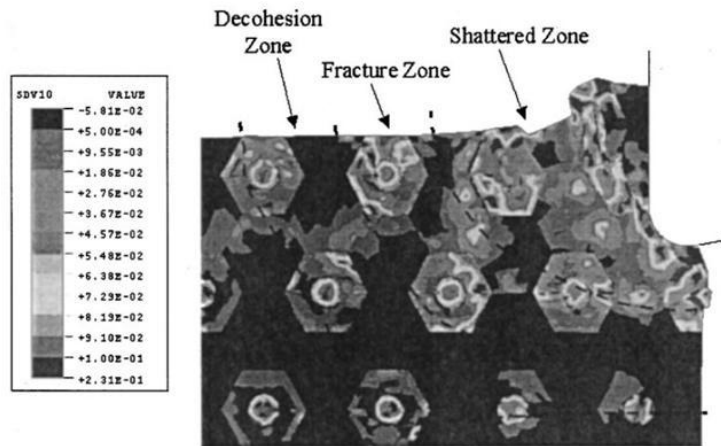
Figure 2.5: Machining damage accumulated during machining ductile iron [46]

During micro-machining processes, reinforcements in MMCs play a significant role in machining performance. Due to the micro-structural influence of particles or fibers in the matrix material, material removal and chip formation mechanism are different from when machining homogeneous material, where only grain size effect is considered.
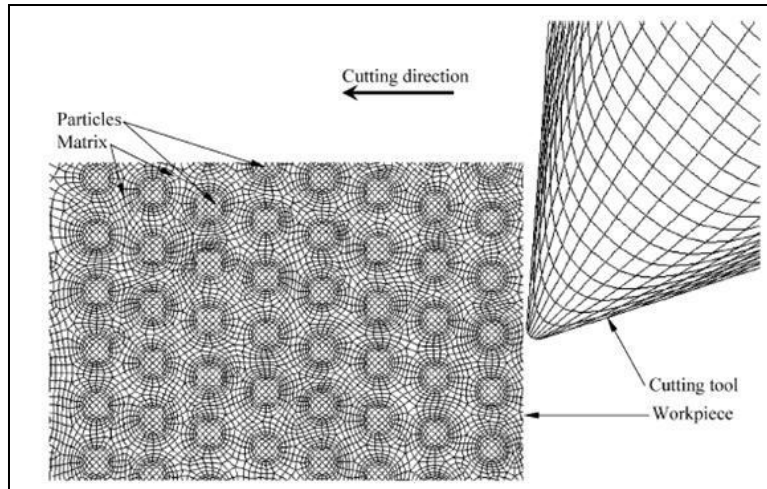
Figure 2.6: Workpiece and tool for MMC machining simulation [48]

As it can be seen in Figure 2.6, the matrix deformation and tool-particle interactions during orthogonal cutting operation were investigated using FE method in [48]. Three scenarios were defined to explain the interactions between the tool and micro-sized reinforcement particles: particle along the cutting path, particle above the cutting path, and particle below the cutting path. The evolution of stress and strain fields as well as some typical physical phenomena, including tool wear, particle debonding and heterogeneous deformation of matrix, were investigated.

Similar FE-based techniques can also be applied to machining of carbon nanotube (CNT) reinforced polymer composite materials. Dikshit *et al.* proposed a continuum-based microstructural material model [49] to simulate machining of CNT reinforced composites using a micro-level FE model [50]. In this model, the Gearing and Anand failure model calibrated at different temperatures were implemented. On average, the model can predict cutting forces with an error of 8% and thrust forces with an error of 13.4%. The chip formation mechanism (Figure 2.7) was studied using this model and a detailed failure mechanism study was further conducted in Reference [51].
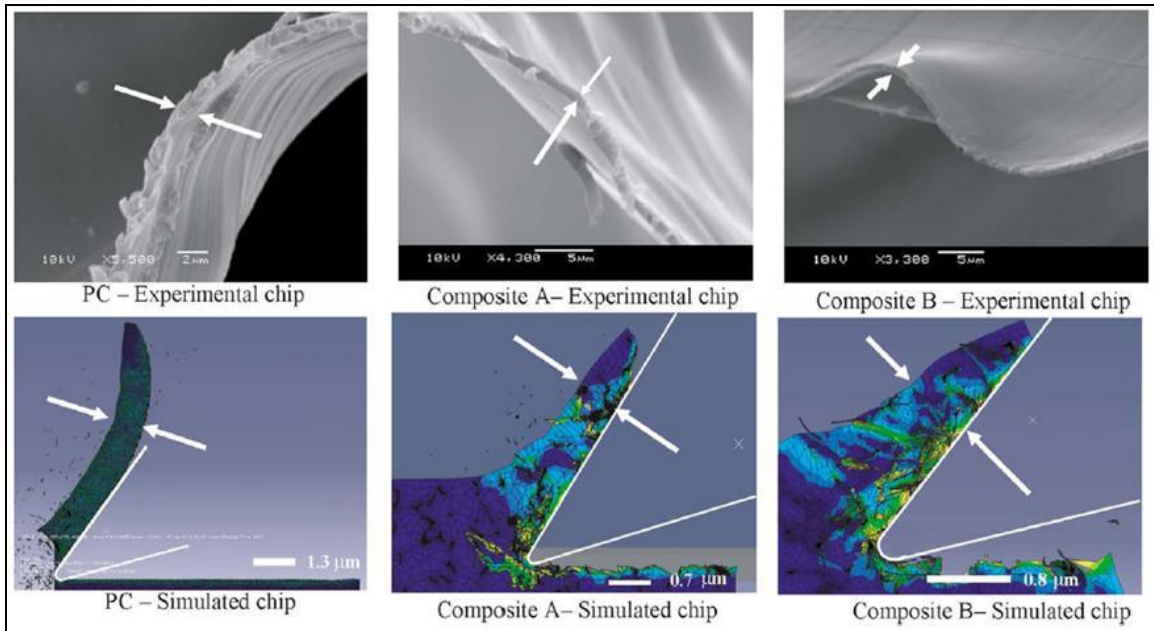
Figure 2.7: Comparison of experimental and simulated chip formation [50]

According to above literature, the cutting mechanism for ceramic-particle reinforced MMCs is still unknown, especially for nano-reinforced MMCs. Further investigations are required to reveal the fundamentals of micro-cutting such materials, in terms of stress-strain distribution, failure mode, chip formation, tool wear, and particle behaviors, etc. Theoretical and experimental studies should be conducted in order to better understand the micro-machinability of nano- and micro-sized reinforced MMCs.

2.2.2 Strengthening Effect

Material removal process in cutting operations is essentially a process where materials are continuously/intermittently fractured and then removed under comprehensive fracture criteria. The enhanced mechanical properties of MMCs, including the yield strength and toughness,

influence the materials' fracture behaviors significantly. Researchers tried to predict the reinforced yield strength by considering different strengthening mechanisms [52-54]. The three main strengthening mechanisms include Orowan strengthening mechanism, enhanced dislocation density strengthening mechanism and the strengthening mechanism of load-bearing effect.

As widely acknowledged, Orowan strengthening is caused by the resistance of hard reinforcement particles to the passing of dislocations. This effect is not a major factor in micro-size particulate-reinforced MMCs, especially for melt-processed MMCs with particles size as 5 μm or larger [55]. However, for nano-sized particles, typically in sub-micron level, Orowan strengthening effect becomes more prominent [52]. Zhang and Chen proposed a model to predict the yield strength of nano-reinforced MMCs and showed that the strengthened yield strength is governed by the size and the volume fraction of nanoparticles, the difference in the coefficients of thermal expansion between the two phases, and the temperature change after processing [52] Also, it indicates that for MMCs with particle size smaller than 50 nm, the yield strength increases dramatically as the particle size decreases (Figure 2.8).

The following equation was proposed to predict the enhanced yield strength:

$$\sigma_{yc} = \sigma_{ym}(1 + f_{load-bearing})(1 + f_{Orowan})(1 + f_{dislocation}) \tag{1}$$

where σ_{ym} is the yield strength of the matrix material; $f_{load-bearing}$ and f_{Orowan} and $f_{dislocation}$ represent the three aforementioned strengthening mechanisms. The prediction showed good agreement with experimental data. However, in reality, material removal process is more complicated due to the complex micro-structural effects, and thus cannot be described by yield strength alone. In this case, the fracture mechanism studies [28, 31, 56] of MMCs become highly important and will benefit the fundamentals of chip formation studies for cutting processes [48,

57]. It was pointed out that the relative contribution of load-bearing effect is very small in nano-reinforced MMCs [53].
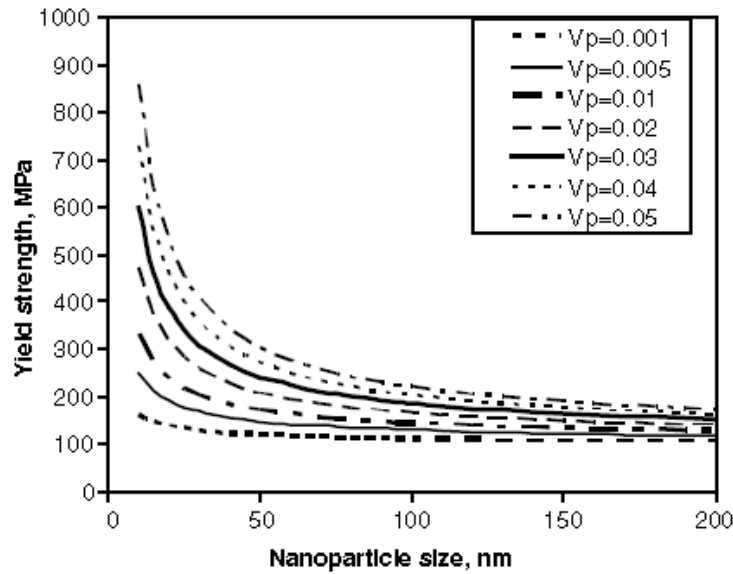
Figure 2.8: Yield strength as a function of nanoparticle size for different volume fractions in nano-Al_2O_3 particulate-reinforced Mg-MMCs [52]

2.2.3 Size Effect

In micro-machining process, the ratio of the uncut chip thickness to the effective tool edge radius becomes a significant factor influencing the cutting performance. As this ratio decreases, the specific cutting energy in machining increases nonlinearly [58-61]. This phenomenon occurs due to several factors, including material strengthening effect, finite tool edge radius, and material separation effects [58]. We observed similar phenomena when micro-milling nano-ceramic particle-reinforced Mg-MMCs, where the size effect plays an important role [62].

In our study, the ratio of particle size to uncut chip thickness, and the volume fraction, significantly affects the micro-milling performance of MMCs. Therefore, heterogeneous materials express different performances from homogeneous materials. Figure 2.9 and Figure 2.10 compare the specific cutting energy trends from experiments for pure Mg and 10 Vol.% Mg-MMCs (with nano-reinforcements), respectively. The horizontal axis represents the nominal feed per tooth (uncut chip thickness). The vertical axis represents the specific cutting energy. The Root Mean Square (RMS) values of in-plane cutting force ($F_{inplane} = \sqrt{F_x^2 + F_y^2}$) were calculated for 18 different cutting conditions. For both cases, three cutting regions were defined to illustrate different dominant cutting mechanisms. Region I is the elastic recovery zone and Region III denotes the traditional shearing zone. The specific cutting energy shows almost linear relationship with the uncut chip thickness in both regions. In Region II, ploughing plays the most important role in cutting mechanism and partial elastic recovery accompanies. It can be seen that the existence of nano particles does change the size effect in micro-machining. Much more energy is needed when cutting Mg-MMCs due to the strengthened mechanical property in all three regions. Besides, when machining Mg-MMCs, the shear zone is shorter than pure Mg, while the ploughing zone is wider. Especially, the amplitude in elastic recovery zone is considerably higher when machining Mg-MMCs than machining pure Mg.
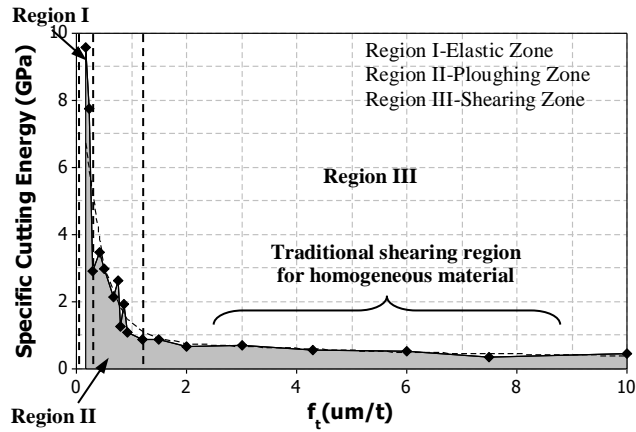
Figure 2.9: Specific cutting energy vs. nominal feed per tooth for Pure Mg [62]
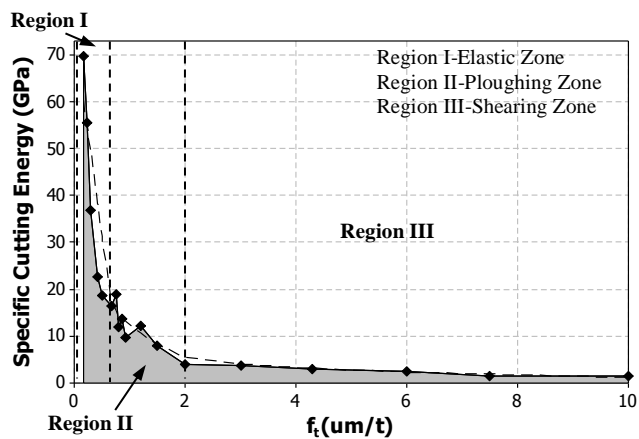
Figure 2.10: Specific cutting energy vs. nominal feed per tooth for 10 Vol.% Mg-MMCs [62]

2.2.4 Minimum Chip Thickness Effect

The role of the minimum chip thickness has been studied by many researchers in the past twenty years both theoretically and experimentally [44, 63, 64]. I In micro-milling conditions, Weule *et al.* firstly proposed the existence of minimum chip thickness and its significant influence on machined surface quality [65]. The authors pointed out that the minimum chip thickness was strongly dependent on material properties. In another theoretical study, Liu *et al.*

28

proposed an analytical model for the prediction of minimum chip thickness [66]. The model considers comprehensive aspects of materials properties as well as cutting conditions. It accounts for the effects of thermal softening, strain hardening, cutting velocity and tool edge radius. The minimum chip thickness value can be predicted from the workpiece's and tool's thermal-mechanical properties.

In our previous study, a comprehensive instantaneous chip thickness model is developed for micro-machining MMCs [62]. The heterogeneity of material's properties is taken into consideration.

- When the uncut chip thickness is smaller than elastic recovery threshold, only elastic deformation occurs and the deformed material will fully recover to its original position. The SiC nanoparticles comply with the same elastic deformation as the Mg matrix and will fully recover to the original positions after cutting.

- As the uncut chip thickness increases beyond the elastic recovery threshold, the elastic-plastic deformation becomes dominant. In this region, it is assumed that a constant percentage of the workpiece material undergoes elastic deformation. The remaining material undergoes plastic deformation. In this case, the SiC particles cannot recover to their original positions. Since the plastic deformation occurs in this region, the matrix-particle interface will be damaged, and then leads to either particle fracture or particle displacements.

- When the uncut chip thickness increases to the minimum chip thickness, the shearing mechanism plays a major role and continuous chips form. In this situation, the elastic recovery rate drops to zero. The reinforcement particles in the chips and the uncut

material can mostly retain their original relative positions locally. Although the particles in the separation zones still have fractures and displacements, this effect is negligible comparing to shearing effect.

2.3 Cutting Process Modeling

2.3.1 Chip Formation Modeling

In macro-scale, the chip formation process can be understood by applying the theory of minimum chip thickness to the instantaneous chip thickness model. This belongs to the mechanistic process modeling technique, which relates the process inputs and outputs by combining a comprehensive characterization of the cutting geometries. However, due to the complex physics, which governs the tool-workpiece interactions, in microscale, chip formation can not be predicted by using only a threshold value. Except for the mechanistic process modeling method, there are other approaches, including molecular dynamics (MD) simulation [67-69], the Finite Element (FE) analysis simulation, and multiscale simulation [70, 71]. MD simulation performs analysis in nano-size with resolution to the atomic level, thus is best suitable for nanometric cutting analysis. FE method is capable of predicting cutting forces, temperatures, stresses, strains and machined surface integrity, since the underlying theory in FE is macro/meso/micro scale continuum mechanics. Therefore, by using FE technique, the chip formation can be modeled and predicted with reasonable accuracy.

In the early stage of computational study of metal cutting, the FE method was used only to obtain intermediate values for semi-mechanistic or empirical models. Ueda *et al.* [72]

presented such a method to analyze the material removal mechanism in micro-machining ceramics. This method largely depended on fracture mechanism for cutting process. FE was used only to calculate the J-integral around a crack in front of the cutting edge, in order to differentiate various cutting modes. Later on, rigid-plastic FE began to prevail in modeling chip formation [73, 74], which is used to further understand the localized adiabatic deformation for homogeneous metals, such as copper.

With the development of modern computer technology, FE simulation can be carried out on more advanced solvers. Some commercially available FE solvers are suitable for cutting simulation and have become popular in academia, such as Abaqus and LS-Dyna. Complex cutting geometries and material models can be embedded into the cutting process model conveniently by using such FE platforms.

In recent decades, tool edge radius effect has gained adequate attention from cutting mechanism researchers [75-78]. In these studies, a 2-Dimentional (2D) orthogonal cutting model was constructed to represent the tool-workpiece interaction, where materials were treated as homogeneous (Table 2.4). Nasr *et al.* [76] presented an Arbitrary-Lagrangian-Eulerian (A.L.E.) FE model to simulate the effects of tool edge radius on residual stresses when dry turning AISI 316L stainless steel. The Johnson-Cook (J-C) plasticity was used for material modeling. The analysis was achieved in two steps. The first step simulated the cutting process, and the second one did the stress-relaxation process. Coupled thermal-mechanical analysis was carried out in both steps. The usage of Eulerian formulation avoids the necessity to define the failure criterion for chip formation. Ozel *et al.* [77] applied the similar modeling technique to simulate high speed machining of AISI 4340 steel, in order to extract the stress and temperature distributions. In the

study conducted by Liu and Melkote [78], the influence of tool edge radius on size effect was investigated by using a strain gradient plasticity-based FE model. Orthogonal micro-cutting simulation was achieved for Al5083-H116. Chip separation criterion was also ignored via an adaptive remeshing technique. Except for the tool edge radius effect, other researchers put emphasis on either advanced hard-to-machine materials [79, 80] or material strengthening mechanisms [58].

Based on the FE modeling approach, the mechanistic models of micro-cutting can be further improved by using the parameters calibrated by FE models. The FE based chip formation studies for homogeneous materials are summarized in Table 2.4. Tool edge radius has been considered as a dominant factor in micro-cutting. For different materials, different constitutive modeling approaches were applied. Even though good results can be achieved and match the experimental data, the use of the Arbitrary Lagrangian Eulerian (A.L.E.) or adaptive remeshing technique makes it possible to ignore the actual chip separation criterion. According to Atkins [81], this is implausible and implies that plastic flow cannot be the phenomenon explaining the separation of chips from the machined surface.

Table 2.4: Comparison of FEA modeling studies on micro-cutting homogeneous metals

No.	Research Purpose	Constitutive Model	Meshing Technique	Fracture Model	Tool edge radius	Materials	Ref. #
1	σ, T	J-C model	A.L.E.	NO	YES	AISI steel	[76, 77]
2	Size effect	Taylor-based non-local plasticity	Adaptive remeshing	NO	YES	Al5083-H116	[78]
3	σ, ε, T, force	Internal state variable plasticity	Adaptive remeshing	NO	Sharp	Mg-Ca alloy	[79]
4	Size effect	Taylor-based non-local plasticity	Adaptive remeshing	NO	Sharp	Al5083-H116	[58]
5	Grain refinement	Dislocation density-based model	A.L.E.	NO	YES	CP Ti	[80]

In the chip formation modeling for heterogeneous materials, such as ductile iron (crystallographic heterogeneous), polymer-based CNT composites and particulate-reinforced MMCs, the fracture mechanisms of the materials have been considered (listed in Table 2.5). Dikshit *et al.* [50, 51] implemented the Gearing and Anand failure model in order to capture the difference between ductile and brittle failure modes in the polymer matrix. For the CNT reinforcement phase, a simple strain-to-failure criterion was used. Chuzhoy *et al.* [45, 47] also considered the material damage model by continuously removing the "damaged" element during simulation. The experimental results of the chip formation are shown in Figure 2.11.

Table 2.5: Comparison of FEA modeling studies on micro-cutting heterogeneous metals

No.	Constitutive Model	Meshing Technique	2D/3D	Matrix	Reinforcement	Particle size	Ref. #
1	Internal state variable model [82]	Adaptive remeshing	2D	Ferritic and pearlitic grains	Graphite (10 %)	µm-sized	[45-47]
2	Mulliken and Boyce model [83]	Adaptive remeshing	2D	Polymer	CNT	nm-sized	[49-51]
3	Johnson-Cook model	NO adaptivity	2D	Al6061	Alumina particles (15 µm)	µm-sized	[84, 85]
4	Equivalent Homogeneous Material (EHM) model [86, 87]	Adaptive remeshing	3D	A359	SiC particles (20%)	µm-sized	[88]
5	Cowper-Symonds model	NO adaptivity	2D	Aluminum	SiC particles (30%)	µm-sized	[48]
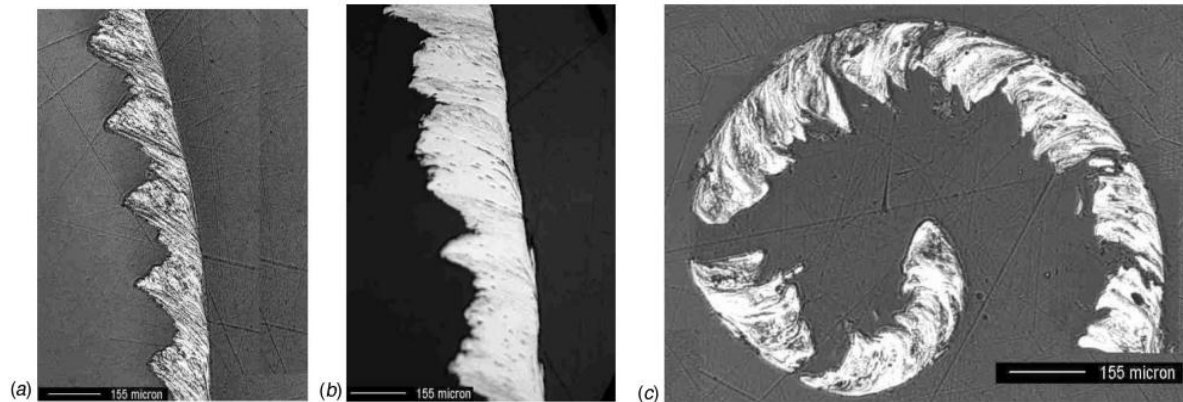
Figure 2.11: Photomicrographs of machined chips of (a) pearlite, (b) ferrite, and (c) ductile iron [45]

Zhu and Kishawy [85] utilized a shear failure model by comparing effective plastic strain

with the damage plastic strain value for each element. Similar approach was also applied in the

work conducted by Pramanik *et al.* [48]. However, the failure modes during micro-cutting particulate reinforced MMCs are far more complex than the existing models proposed by previous researchers. More research effort toward the fracture behavior of the particulate MMCs is needed both theoretically and experimentally. The understanding of failure modes potentially requires the application of cohesive zone models so that it is possible to capture the details of particles' effect on micro-cutting. Material's constitutive modeling is another aspect requiring more research. Currently, most of the material models take account of the mechanical behaviors in a uniaxial manner. Due to the nature of cutting, the loads applying on the material should be multi-axial. Therefore, materials' constitutive model should be reformulated in order to accommodate this micro-cutting fact.

As it can be seen in Table 2.5, most of research on micro-cutting MMCs focuses on micro-sized particulate MMCs. There are very few publications on the machining of nano-sized particulate MMCs. The research on particle size effect and the micro-cutting of nano-reinforced MMCs will lead to a new area for metal cutting theory. Molecular dynamics simulation and multi-scale modeling techniques will be necessary in the analysis.

2.3.2 Cutting Force Modeling

Cutting MMCs is considerably difficult due to the extremely abrasive nature of the reinforcements that causes rapid tool wear and high machining cost [35]. Thus, it is crucial to fully understand the effect of ceramic particles on the machining process. Based on the process model, machining quality and cost can be improved through optimizing the cutting conditions for specific composite materials. As a step towards this goal, cutting force modeling is very critical.

During the last decade, process models have been developed to predict cutting force at the micro-milling scale [44, 89-91]. Jun *et al.* [89, 92] studied the geometric chip formation mechanism in micro-milling and proposed a new algorithm to compute the instantaneous chip thickness by incorporating the minimum chip thickness effect. In their later work [90], the mechanistic model of micro-milling forces was proposed. This model considered the effects of ploughing, elastic recovery, tool run-out and dynamics; and it focused on homogeneous materials. Vogler *et al.* [44, 91] proposed a mechanistic model that explicitly accounts for different phases when machining heterogeneous materials. The model predicted the higher frequency components of cutting forces by considering the multiple phases (in micro-scale grain size) in the material model. However, as the size of the reinforcement particles decreases to nano-scale, this model is not suitable to predict cutting forces since SiC nanoparticles will not be directly cut by tool edge. Kishawy *et al.* [93] proposed an energy-based analytical force model for orthogonal cutting Al-MMCs. In this model, the total specific energy for deformation had been estimated for the debonding of ceramic particles from the aluminum matrix as a function of volume fraction and material properties. The model was validated and applicable for micro-sized ceramic reinforced MMCs in turning configuration. For nano-sized reinforcements, they are more prone to escape the cutting than the micro-scale particles during machining. Therefore, it is more challenging to model the cutting force for nano-reinforced heterogeneous materials.

As for calibration of cutting force coefficients, some previous researchers expressed the simultaneous force coefficients as a nonlinear exponential function [94-96]. Wan *et al.* [96] proposed a genetic procedure to calibrate the force coefficients using instantaneous cutting force. An exponent-like function was proposed to describe the relationship between force coefficients

and uncut chip thickness. The force was predicted using calibrated instantaneous force coefficients [96-100]. This method was experimentally validated under conventional milling conditions. Additionally, the method uses the instantaneous cutting force signals [97, 98]. The accuracy of the force coefficients heavily depends on where the data is truncated and the length of the data. Other models were developed based on constant cutting force coefficients [44, 90, 101-103]. The coefficients in mechanical micro-machining were calibrated according to different cutting mechanisms, such as shearing and ploughing [90, 102]. The minimum chip thickness plays an important role in differentiating the cutting mechanisms. Liu *et al.* [66] developed an analytical model to predict the minimum chip thickness by considering various material properties and cutting conditions.

Finite element models can also be used to calibrate cutting force coefficients. 2-D FE models built for orthogonal cutting can be efficiently used to acquire cutting coefficients which are essential for cutting force modeling. Accurate material models are required and computational load can be high for high quality meshing [59]. Afazov *et al.* [104] proposed a new approach for predicting micro-milling cutting forces using the FE methods. A set of FE analyses were performed firstly at different chip loads and cutting speeds, and then the relationship between cutting forces, chip load and cutting velocities could be nonlinearly fitted and used in micro-milling force calculation. The full relation between these variables is expressed in equation (2), where h is uncut chip thickness, v is the tangential cutting velocity and $p_1 \sim p_6$ are the constants. The predicted and experimental cutting force results are shown in Figure 2.12.

$$F_{c,t} = (p_1 v^{p_2})[1 - \exp(p_3 h)] + (p_4 v + p_5)[1 - \exp(p_6 h)]$$

(2)
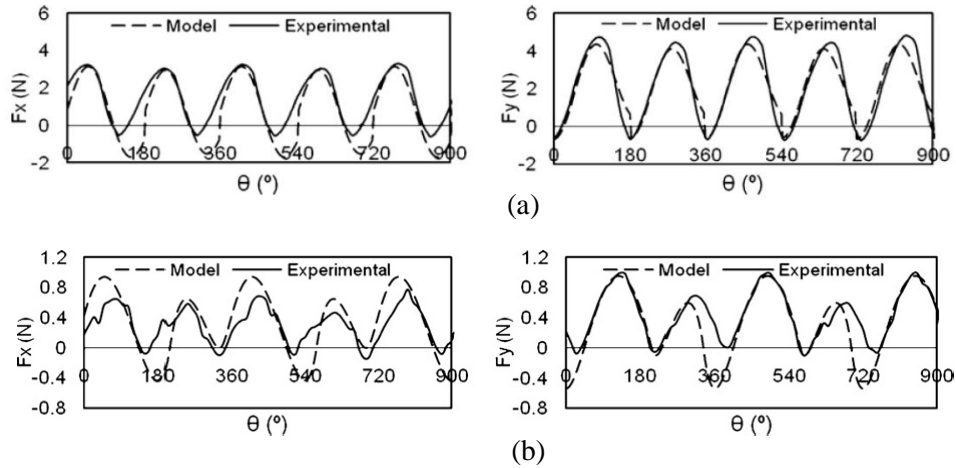
Figure 2.12: Cutting forces at different cutting conditions on AISI 4340: (a). spindle speed 5000 RPM, feed speed 2 mm/s; (b). spindle speed 50000 RPM, feed speed 0.5 mm/s [104]

Altintas and Jin [105] further improved the mechanics understanding of micro milling by incorporating the effect of tool edge radius. The authors proposed a micro-milling force analytical model from material's constitutive model and friction coefficient. The chip formation process is predicted with a slip-line field model [75]. The predicted cutting forces are displayed in Figure 2.13.

As for heterogeneous materials, Park *et al.* [106] introduced a method for mechanistic cutting force model calibration using microstructural FE model for ferrous materials. This method requires detailed modeling for the materials' microstructures in order to achieve accurate calibration. Liu *et al.* [62] proposed another cutting force structures and corresponding calibration technique by considering the behaviors of reinforcement ceramic particles for Mg-MMCs. The simulated cutting forces are shown in Figure 2.14.
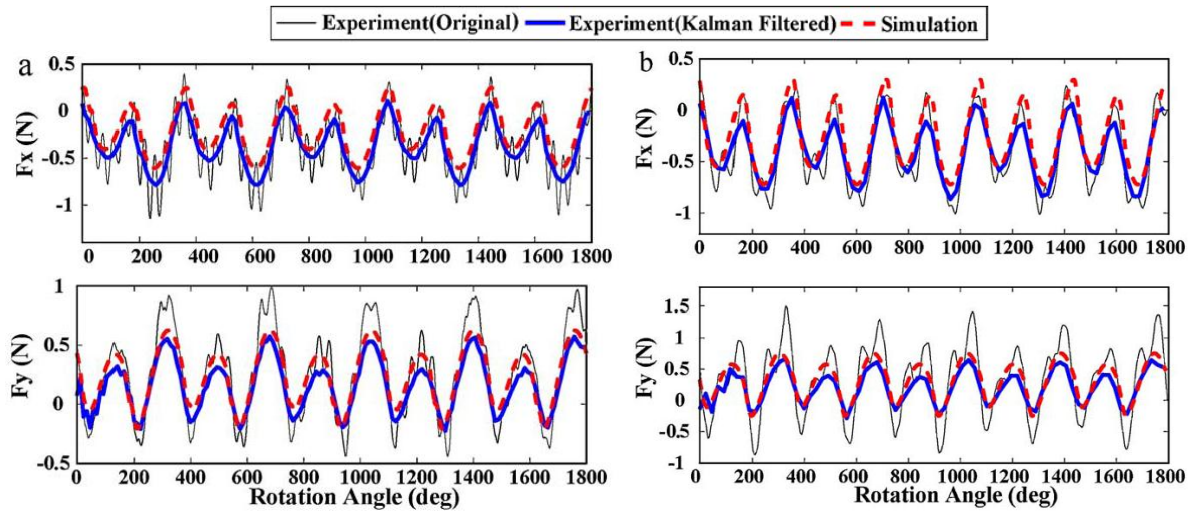
Figure 2.13: Slot micro-milling with 50 μm axial depth of cut on Brass 260 using 200 μm dia. cutting tool (with two 30˚ helical flutes) at cutting conditions: (a). spindle speed: 20000 RPM, feed rate: 3 μm/tooth. (b). spindle speed: 40000 RPM, feed rate: 5 μm/tooth [105]
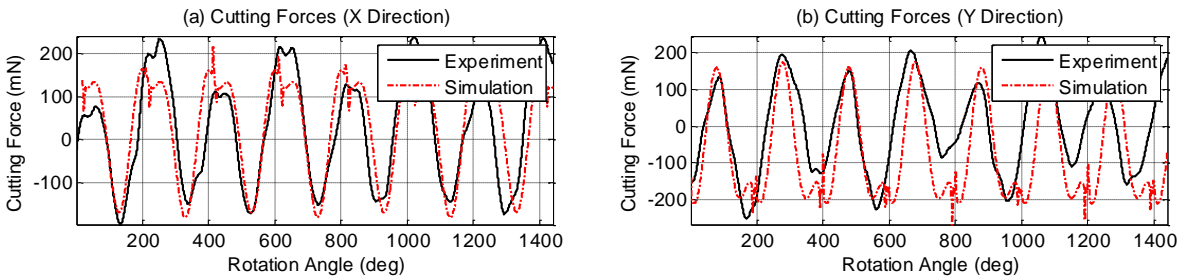
Figure 2.14: Cutting forces on 10 Vol.% SiC nanoparticle reinforced Mg-MMCs at cutting condition: spindle speed is 4,000 RPM, feed speed is 0.4 mm/s (f_t = 3.0 μm/t) and depth of cut is 20 μm using 1 mm diameter end mill [62]

2.3.3 Other Aspects

The dynamics modeling of micro-cutting requires fully understanding the behaviors of material-tool-holder system and the machine tool structures. Prior to these aspects, the fundamental cutting mechanisms are the foundation of dynamic analysis of micro-cutting MMCs, because the existence of reinforcements in the matrix affects the overall dynamic behaviors [36, 44], especially for micro-milling processes.

Filiz and Ozdoganlar [107] presented an analytical model of the transverse vibration of rotating micro end mills in the presence of tool alignment errors and tool manufacturing errors. The model can be used for micro tools design and stability analysis of micro-milling processes. A more sophisticated dynamics model for micro-milling was constructed by Jun *et al.* [89, 92], considering the complex chip formation nature. The stability characteristics due to the regenerative effect were also studied. It was found that there was significant increase in vibration due to the unbalance arising from process faults. Thus, the estimation of effective process errors/faults [108] and its analysis are essential to mitigate un-balance induced vibration. It was noted that the minimum chip thickness effect causes instability when feed rate is around the minimum chip thickness.

Based on our extensive literature survey, there is little relevant research on how the material's microstructures affect system dynamics, which is crucial for particulate MMCs machining. For example, in micro-milling process, measurements of tool vibration and tool deflection is a challenging task, because the vibration measurement at the shank of the cutting tool can be misleading [92]. During micro-milling, the tool tip is buried into the workpiece material. Current measurement techniques are able to detect the displacement at the cutting tool shank which is different than the actual tool tip deflection and vibration. Therefore, the effect of reinforcement particles on the micro-cutting dynamics, tool vibration, tool deflection [109], chatter prediction and suppression [110-112] will need to be studied for MMC micro-machining.

Surface measurement and modeling is also difficult since the nature of machined surface generation is complicated and determined by numerous factors [113]. Vogler *et al.* [114] built the surface generation models for surface roughness in micro- end milling of single phase and

multiple phase materials based on minimum chip thickness theory. The model was able to accurately predict the surface roughness for single phase materials. For multi-phase materials, the authors pointed out that surface roughness is affected by three independent effects, including: geometric effect, minimum chip thickness effect and the effect of burr formation at the grain boundaries. The effect of reinforcement particles in particulate MMCs still remains unstudied by previous researchers.

Cutting temperature distribution for micro-cutting is usually captured and analyzed by infrared (IR) camera [115, 116]. Along with the cutting temperature, machined surface residual stress, tool wear, and tool life prediction under the effect of reinforcement particles are still unclear for particulate MMCs during micro-cutting operations.

2.4 Summary and Analysis

This chapter provides a literature review on micro-cutting ceramic-reinforced Metal Matrix Composites (MMCs). Some observations regarding past work and future directions are summarized:

1. The cutting mechanism of the nano-/micro-sized ceramic particle reinforced MMCs is not fully understood for micro-machining operations, in terms of stress-strain distribution, failure mode, chip formation, tool wear, and particle fracture/debonding/dislocation.

2. Although there exist a number of studies and theories on machining micro-reinforced particulate MMCs over the last 25 years, further machinability study is still needed.

Because the existing literatures mostly focus on conventional-scale turning, the theoretical and experimental study in micro-scale machining is needed.

3. Multiphase materials' performance in micro-cutting has been studied by using ductile iron as samples. However, the eutectic heterogeneous materials are different from engineering-designed MMCs. The cutting mechanisms for MMCs should be redefined beyond the understanding of multiphase materials, such as ductile irons and CNT reinforce polymers.

4. Since cutting performance is strongly affected by the cutting mechanisms in three scales: macro, meso and micro, a thorough understanding of the cutting mechanisms in different scales is required.

5. In particulate MMCs, the effects of particle shapes (aspect ratio), particle size and volume fraction have great influences on the micro-cutting performance. The effects of these factors on cutting mechanisms should bring more attention in order to better understand MMCs' micro-machining process.

6. As the particle size decreases to nanometer level, the continuum mechanics laws can be fundamentally different. FE approach based on continuum assumption will remain as one of the suitable candidates to conduct chip formation simulation. How to simulate nano-particle reinforced MMCs is challenging until some explicit modeling technique is established.

7. The fracture mechanics and criteria for MMCs should be carefully considered to achieve accurate simulation of chip separation. The currently popular technique using A.L.E. or adaptive remeshing skills in FE is not suitable for heterogeneous material cutting

simulation. Homogenized material properties, including elasticity, plasticity and failure modes, are good enough to initiate research work on cutting mechanisms.

8. Process models, including chip formation model, cutting force model, tool deflection model and surface generation model, should be constructed to better understand the micro-machinability of nano- and micro-size reinforced Mg-MMCs.

9. The explicit process models connecting the controllable input cutting conditions with output variables (e.g., cutting forces, tool deflections and generated surface roughness) for advanced heterogeneous MMCs during machining process will benefit the industrial needs for MMCs processing.

CHAPTER 3   MACHINABILITY STUDY ON MAGNESIUM BASED METAL MATRIX COMPOSITE

3.1 Design of Experiments (DOE) Method

This section experimentally investigates the machinability of Magnesium Metal Matrix Composites (Mg-MMCs) with high volume fractions of SiC nano-particles using micro-milling process. The nanocomposites containing 5 Vol.%, 10 Vol.% and 15 Vol.% reinforcements of SiC nano-particles were studied and compared with pure Magnesium. The milling was carried out at different feedrates and spindle speeds chosen according to Design of Experiment (DOE) method. Cutting forces, surface morphology and surface roughness were measured to understand the machinability of the four different materials. Based on Response Surface Methodology (RSM) design, experimental models and related contour plots were developed to build a connection between material properties and cutting parameters. Those models can be used to predict the cutting force, the surface roughness, and then optimize the machining conditions with the required cutting forces and surface roughness.

3.2 Experimentation and Process Monitoring

3.2.1 Experimental Setup

The experiments were carried out on a micro-milling platform under dry machining condition. The micro-milling machine was set up on a tetrahedral space frame, as shown in Figure 3.1. The feed system of the machine was composed of three precision linear stages along X, Y and Z axes. An Aerotech Ensemble multi-axis motion controller was utilized to maintain the accurate machining position in nanometer scale (motion resolution can reach as high as 4 nm). The air-bearing spindle was fixed at the center of the tetrahedral frame. The highest speed of the spindle is 80,000 rpm. A Kistler 9256C2 triaxial piezoelectric dynamometer was used to measure instant cutting forces along X, Y and Z directions. The vibration of the machining tetrahedral platform was measured by a PCB triaxial piezoelectric ICP accelerometer, which was mounted at the spindle holder. A National Instrument (NI) PXI-based Data Acquisition (DAQ) system was used to conduct real time measurement of cutting forces. The machined surface morphology was assessed by using Scanning Electron Microscope (SEM) to observe the bottom surface of slots. Surface roughness tester SRG-4000 (profilometer) and Keyence LT-9010M confocol displacement meter were used to measure the surface roughness of machined surface, which is at the bottom of the machined slots.
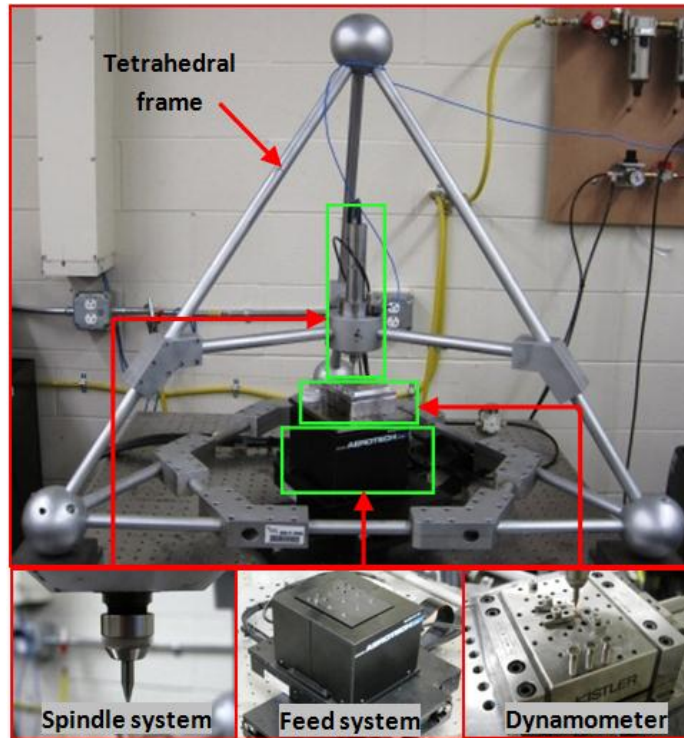
Figure 3.1: Micro-milling machine platform

3.2.2 Material Preparation

To fabricate the SiC reinforced Mg-MMCs, Magnesium powder of 98% purity with a mean diameter of 30 μm was used as the matrix material, and nano-size SiC particles with a mean diameter of 20 nm as shown in Figure 3.2 was used as the reinforcement. The two materials with desired volume fractions were mixed using high energy ball milling for 20 hours to ensure the uniform distribution of SiC nano-particles within Mg matrix. The obtained powder mixtures were sintered by Spark Plasma Sintering (SPS) technique at 600°C for 5 minutes. The densities of the resultant composites were measured using Archimedes' method and were found to reach their respective theoretical density. For comparison, pure Mg was also prepared using the same procedure. For simplicity, the four different sample materials made from pure Mg, Mg-

MMCs with 5, 10 and 15 Vol.% SiC nano-particles are named sequentially as Pure Mg, Composite A, Composite B and Composite C in this chapter.
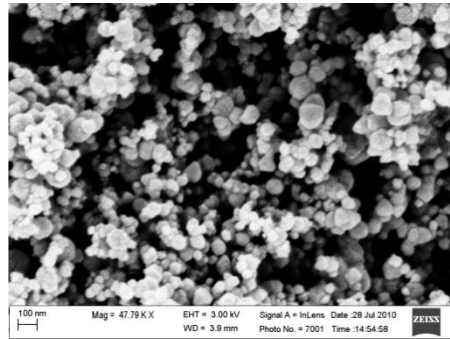
Figure 3.2: 20 nm SiC particles

3.2.3 System Dynamics

In order to acquire accurate cutting force measurements, the piezoelectric dynamometer (Kistler 9256C2) was tested and calibrated. The machining coordinate is defined as follows: X is the direction norm to feed direction, Y is the feed direction, and Z is along the tool axial direction. The calibration of the dynamometer was performed by using the instrumented impact hammer (PCB-086C03) to verify the force measurements. The sensitivity of the hammer and the dynamometer are 2.25 mV/N and 26 pC/N, respectively. The noise level was approximately 5 mN which is insignificant compared with cutting forces.
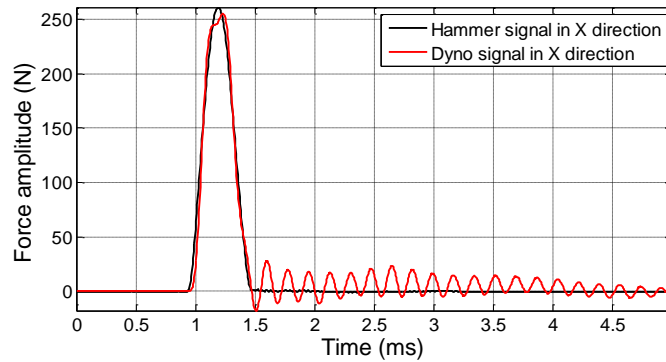
Figure 3.3: Time domain impact and response results for F_x
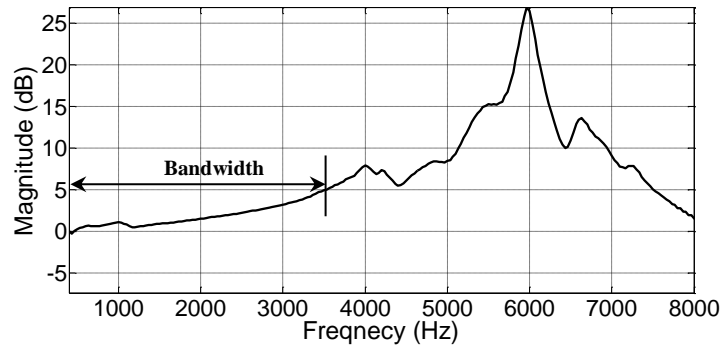
Figure 3.4: Dynamic frequency response for F_x

By using the hammer to trigger the dynamometer without load along X-Y-Z direction in sequence, the force signals from hammer and dynamometer were measured and the results in X direction are shown in Figure 3.3 as an example. The dynamometer was calibrated by force signals from hammer. Meanwhile, frequency response plot of dynamometer's measurements shows its measuring bandwidth. From Figure 3.4, it can be seen that the X axis of the dynamometer's bandwidth is approximately 3500 Hz, and it is similar for Y and Z axes. Therefore, the maximum measurable spindle speed can be 105,000 rpm by this dynamometer with a two-flute tool. Consequently, since only the effects of the spindle frequency and the tool path frequency are considered in the analysis, the dynamometer's bandwidth is adequate to

accurately measure the cutting forces. Additionally, according to the spindle's property, in the experimental design, the spindle speed range was selected to be from 20,000 rpm to 60,000 rpm.

3.3 Experiments Design

The Design of Experiments (DOE) method based on three-factor Response Surface Methodology (RSM) was used to design the experimental conditions [117, 118]. Specifically, Central Composite Design (CCD) was employed. All the cutting conditions are summarized in Table 3.1. Based on this design, the effects of spindle speed, feedrate and volume fraction on average cutting forces (F_x, F_y, and F_z) and surface roughness (R_a and R_q) can be systematically studied. Further, the experimental models can be produced to predict the cutting force, the surface roughness, and then optimize the cutting conditions.

In the experiments, the uncoated solid WC micro end mills (TR-2-0400-S) with two flutes and the diameter of 1.016 mm were chosen. The straight grooves with the length of 5 mm and 10 μm depth of cut were slotted under different cutting conditions. For each sample, a new tool was used in order to remove the effect of tool wear between different samples.

Table 3.1: Cutting conditions

Trail #	Feedrate (mm/s)	Spindle speed (kRPM)	Volume fraction (%)	Sample
1	0.5	20	5	Composite A
2	1.5	20	5	Composite A
3	1.0	40	5	Composite A
4	0.5	60	5	Composite A
5	1.5	60	5	Composite A
6	1.0	20	10	Composite B
7	0.5	40	10	Composite B
8	1.0	40	10	Composite B
9	1.5	40	10	Composite B
10	1.0	60	10	Composite B
11	0.5	20	15	Composite C
12	1.5	20	15	Composite C
13	1.0	40	15	Composite C
14	0.5	60	15	Composite C
15	1.5	60	15	Composite C
16	1.0	20	5	Composite A
17	0.5	40	5	Composite A
18	1.5	40	5	Composite A
19	1.0	60	5	Composite A
20	1.0	20	10	Composite B
21	0.5	40	10	Composite B
22	1.5	40	10	Composite B
23	1.0	60	10	Composite B
24	1.0	20	15	Composite C
25	0.5	40	15	Composite C
26	1.5	40	15	Composite C
27	1.0	60	15	Composite C
28	0.5	20	0	Pure Mg
29	1.0	20	0	Pure Mg
30	1.5	20	0	Pure Mg
31	0.5	40	0	Pure Mg
32	1.0	40	0	Pure Mg
33	1.5	40	0	Pure Mg
34	0.5	60	0	Pure Mg
35	1.0	60	0	Pure Mg
36	1.5	60	0	Pure Mg

3.4 Cutting Force Analysis

Before analyzing the experimental data, the validity of the experimental design was examined based on the measurements. Figure 3.5 shows that the responses of F_x are not skewed and no outliers are found in the data. The normal probability p-value corresponding to F_x is 0.448. All of these indicate that the data is normally distributed and the three factors chosen here are the only significant factors influencing the responses. Figure 3.6 illustrates there is no systematic effects in the data due to time or experimental order. Similar results are also attained for F_y, F_z and the surface roughness. Consequently, the data acquired from the experiments based on this design are valid for analysis.
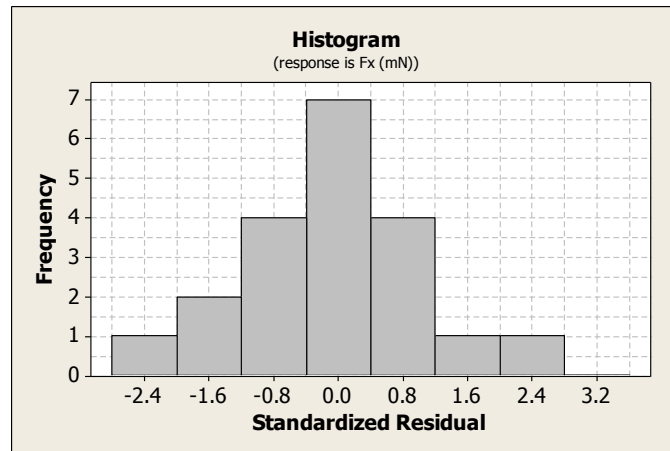
Figure 3.5: Residual histogram for the cutting force F_x
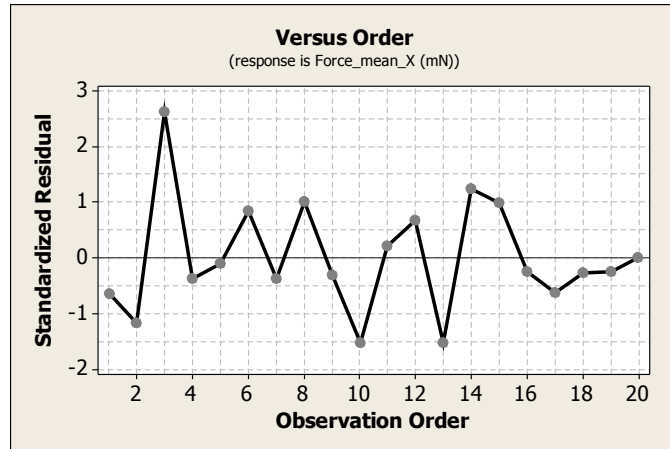
Figure 3.6: Residuals vs. order for the cutting force F_x

3.4.1 Effect of Feedrate and Spindle Speed

Figure 3.7 shows the Root Mean Square (RMS) average cutting forces, F_x, F_y and F_z, during the entire slotting for Composite A, under spindle speed 60,000 rpm with three different feedrates (0.5, 1.0 and 1.5 μm/tooth). It indicates the influence of feedrate on the normal force F_x, the feed force F_y, and the axial force F_z. As the feedrate increases, the magnitudes of the average forces along X, Y and Z directions all increase. It can also be observed that the axial force F_z has a similar increasing rate as the normal force F_x, while the increasing rate of the feed force F_y is smaller. The similar trend also appears under low spindle speed (20,000 rpm) and medium spindle speed (40,000 rpm).
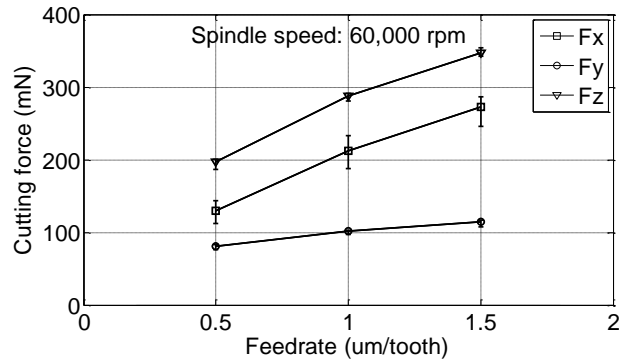
Figure 3.7: Influence of the feedrate on the cutting force for Composite A

The influence of the spindle speed on the average cutting forces for Composite A is shown in Figure 3.8. The average magnitudes of the normal force F_x, feed force F_y and axial force F_z during the entire slot milling all rise up with the increasing of the spindle speed. Especially at the highest spindle speed 60,000 rpm, the cutting forces along X and Z directions have the largest increasing. A similar trend is also obtained at feedrate 1.0 μm/tooth and 1.5 μm/tooth. This is different from previous literature results. As for aluminum-based alumina reinforced MMCs machining, it was reported in [33, 35] that the cutting forces decrease as the spindle speed increased. Also, when machining Al-based SiC reinforced MMCs, the specific power was observed to be minimum when the cutting speed was set to maximum level. The reason is most likely due to higher wear resistance of Mg-MMCs compared to Al-MMCs . As the spindle speed increases, the material's wear resistance is more phenomenal and therefore increases the cutting forces significantly.
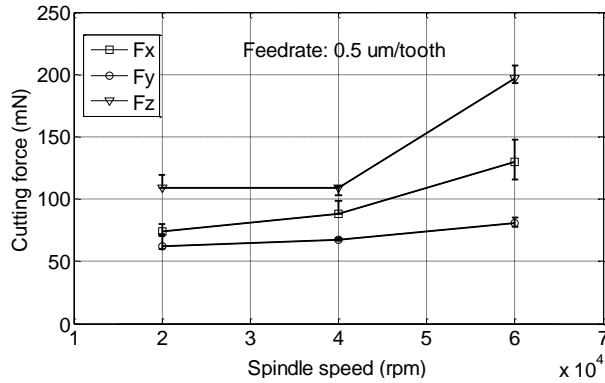
Figure 3.8: Influence of the spindle speed on the cutting force for Composite A

3.4.2 Effects of Volume Fraction

The hardness of Mg-MMCs is closely related to the volume fraction of SiC particles [8]. Therefore, the volume fraction plays an important role in determining material mechanical properties and its machinability. Pure Mg is considered as a sample with 0 Vol.% reinforcement particles. Figure 3.9 summaries the norm force, which is the square root of the quadratic summation of all three force components along X, Y and Z directions ($\|F\| = \sqrt{F_x^2 + F_y^2 + F_z^2}$), f for the four different material samples. Region I, II and III correspond to the spindle speed of 20,000, 40,000 and 60,000 rpm. In each region, the feedrate is increased from 0.5 μm/tooth to 1.0 μm/tooth, then to 1.5 μm/tooth.
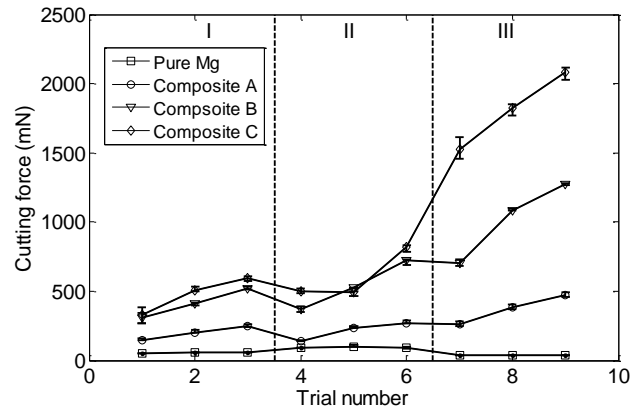
Figure 3.9: Effect of the volume fraction in different cutting conditions

Figure 3.9 illustrates that the cutting force is very small when the volume fraction is low, and comparatively the cutting force increases as the volume fraction increases. The influence of volume fraction on the cutting force is most remarkable at the highest spindle speed (Region III). Interestingly, under the highest spindle speed, the cutting force of Pure Mg decreases slightly, while the cutting forces for Composite A, B and C all increase significantly. It indicates the machining characteristics of Mg-MMCs can be completely different from machining of homogeneous materials (such as pure Mg).

These results presented in Figure 3.9 are different from those reported previously [32, 35, 36, 119, 120]. According to [36], for both non-reinforced metal materials and reinforced metal composites, cutting forces increase with the increase of spindle speed within a certain range. Beyond that region, the cutting forces start to decrease due to thermal softening. The reason is that at low spindle speeds, heat generation is relatively low, thus the increase of cutting forces is likely attributed to the increased strain rate [120]. However, when spindle speed exceeds a certain value, heat generated by machining can lead to the thermal softening of workpiece

55

materials, which reduces the cutting forces correspondingly. Conversely, the cutting force for the Mg-MMCs studied here continually increases with spindle speed. This is likely due to that the SiC nanoparticles can improve the thermal stability of Mg-MMCs. A better thermal stability restricts the dislocation motion of materials and limits the thermal softening [8].
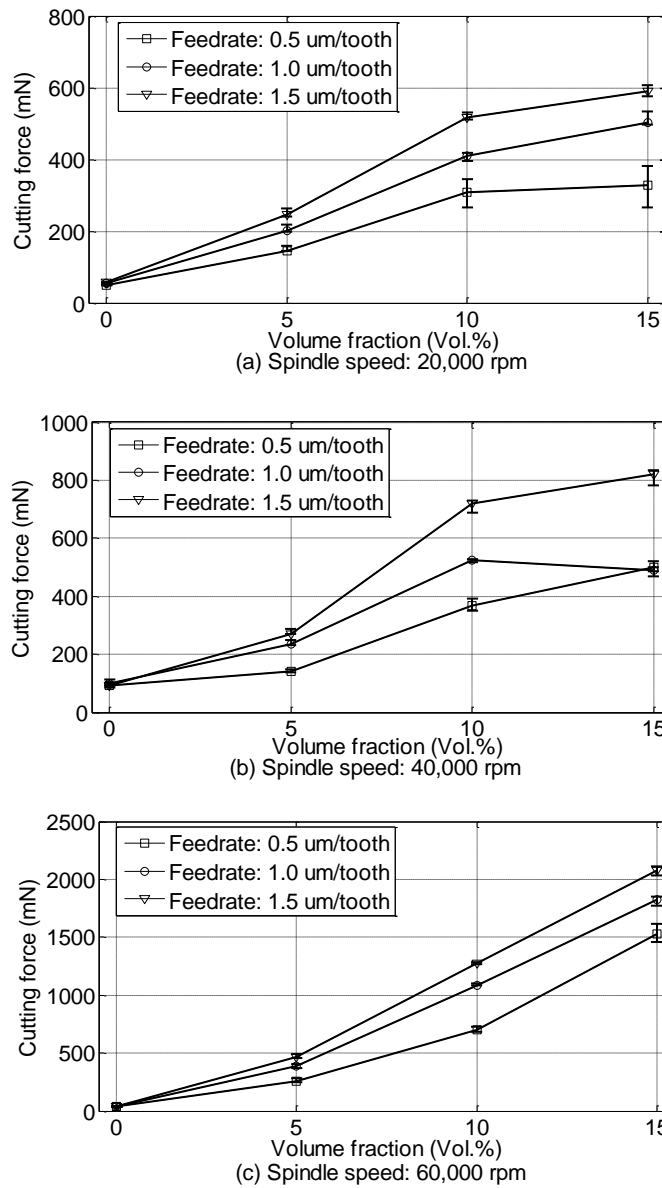
Figure 3.10: Combined effect of the volume fraction and the feedrate on the norm force

Figure 3.10 reveals the combined effect of the volume fraction and the feedrate on the norm force at different fixed spindle speeds. It is seen that for all spindle speeds, the cutting force increase with increasing the SiC concentration. In Figure 3.10(a), the spindle speed is fixed at 20,000 rpm, the cutting force not only increases with the increase of the feedrate, it also increases with the increase of the volume fraction of Mg-MMCs. Similar trend is observed as well when spindle speed is set at 40,000 and 60,000 rpm in Figure 3.10(b) and Figure 3.10(c), respectively. This is agreeable with the knowledge that the mechanical properties of composite materials are strengthened with the increased volume fraction of nano-particles [16, 35]. Additionally, it is also observed that the cutting force increase faster for higher feedrates at the same spindle speed.

Furthermore, it can be seen from Figure 3.10(a) and Figure 3.10(b), the slopes of the cutting force between 5 to 10 Vol.% are generally larger than that for the other two regions (from 0 to 5 Vol.%, and from 10 to 15 Vol.%), which may represent a drastic mechanical strength property change when the volume fraction is around 10 Vol.%, where the inter-particle spacing is approaching the particle size [16]. However, as shown in Figure 3.10(c), as the spindle speed is set at 60,000 rpm, with a higher feedrate value (1.0 or 1.5 μm/tooth), the increasing slopes of the cutting force are maintained roughly the same at both regions of from 5 to 10 Vol.% and from 10 to 15 Vol.%. This is an interesting phenomenon and will be explored further.

3.5 Surface Morphology Analysis

Comparing to traditional homogeneous metal materials Due to the high reinforced strength and extraordinary wear resistance of Mg-MMCs, decent surface quality is relatively difficult to achieve for Mg-MMCs due to their high strength and high wear resistance. As one of the most important parameters in evaluating the machined surface integrity, the surface roughness was measured along the bottom of the slots using profilometer. The corresponding roughness values are obtained by the average of five repeated measurements at the same location along the feed direction.

Table 3.2 summarizes the measured surface roughness. In general, no obvious effect of a single experimental variable (feedrate, spindle speed or volume fraction) on the machined surface roughness can be concluded for the experimental tests conducted. Figure 3.11 shows SEM images of the tool wear after cutting (a) pure magnesium and (b) 15% MMC for 9 slots. The images show no difference in tool wear pattern. Therefore, tool wear does not contribute to variation in surface roughness summarized in Table 3.2. This phenomenon differs from previous research results [121] of Aluminum MMCs where the tool wear is severe. This is likely due to that the nano-sized SiC particle exhibited reduced abrading effect on the tool.

Table 3.2: Surface roughness on machined surface

Spindle speed (rpm)	Feedrate (μm/tooth)	Ra (μm)			
		Pure Mg	A	B	C
20,000	0.5	0.434	0.438	0.246	0.563
20,000	1	0.413	0.513	0.395	0.523
20,000	1.5	0.437	0.529	0.574	0.419
40,000	0.5	0.743	0.543	0.555	0.748
40,000	1	0.486	0.504	0.525	0.658
40,000	1.5	0.380	0.546	0.548	0.807
60,000	0.5	0.234	0.558	0.534	0.815
60,000	1	0.562	0.58	0.486	0.828
60,000	1.5	0.386	0.714	0.657	0.664
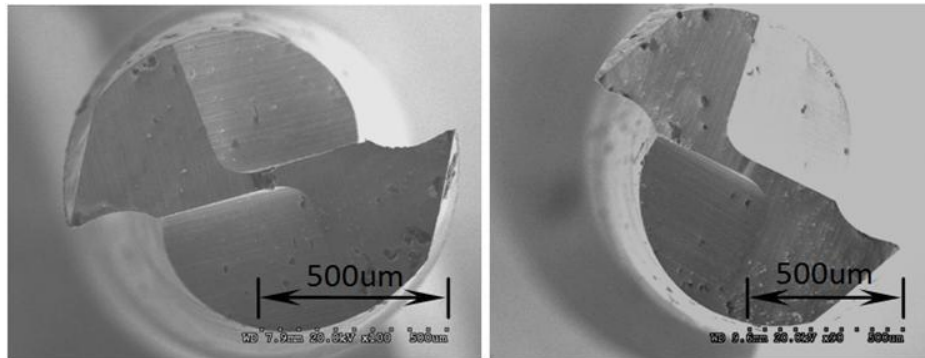
(a). For Pure Mg   (b). For 15% MMC

Figure 3.11: Tool wear after cutting

Figure 3.12 shows the surface morphology of a machined slot for Composite C with the spindle speed at 40,000 rpm and the feedrate at 0.5 μm/tooth. It is seen that on the left, the slot has a clear edge along the entire slotting path. The figure on the right is a magnified SEM picture at an arbitrary location on the bottom of the machined slot. The curves are the tool tip paths and the voids may be caused by the scratches of the attached chips on the tool tip sliding on the top

of workpiece surface. Further research will be conducted to fully understand the tool-workpiece interaction.
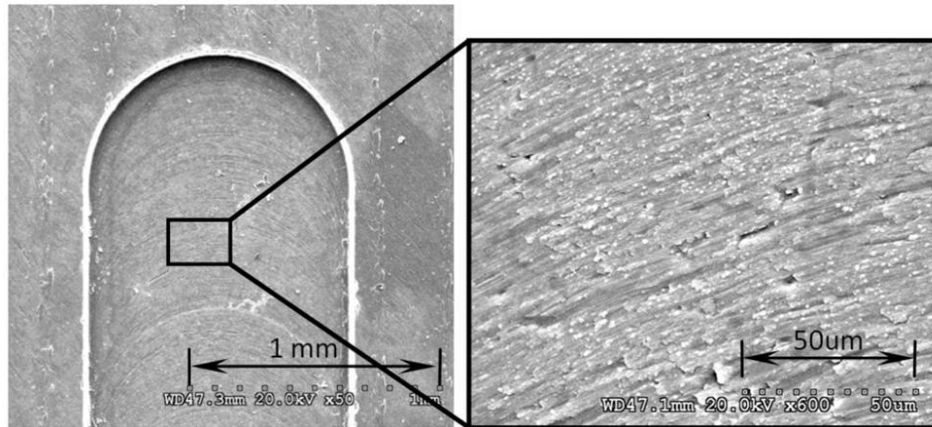
Figure 3.12: Slot surface morphology

3.6 Cutting Condition Optimization

3.6.1 Model Validation

The relationship between each factor (feed rate, spindle speed and volume fraction) with the cutting force and the surface roughness is studied here by main effects plots. Since a more important factor causes a steeper slope, by comparing the main effect factor for cutting force Figure 3.13, it can conclude that spindle speed and volume fraction are more important factors for the cutting force.
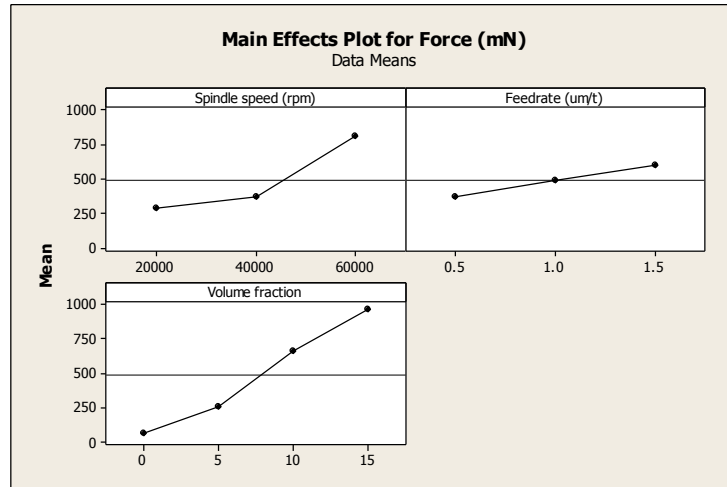
Figure 3.13: Main effects plot for cutting force

Meanwhile, from the main effects plot for the surface roughness (Ra) in Figure 3.14, spindle speed and volume fraction cause larger slopes, even though not monotonically. It illustrates that the spindle speed and volume fraction are the dominant factors affecting the surface roughness but the relationship is not monotonic. This is mainly because the surface generation during micro-machining is complex and related to several aspects, such as cutting conditions, tool material, tool deflection, tool wear and workpiece material, etc. Therefore, it is difficult to conclude that machined surface roughness has a clear trend with one single experimental parameter.
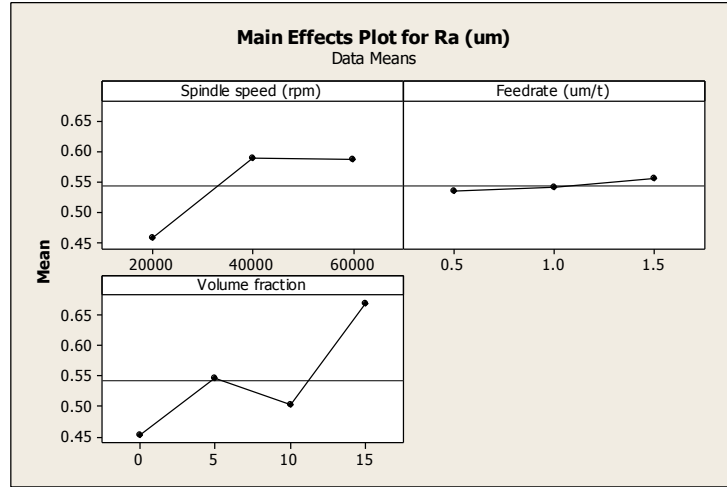
Figure 3.14: Main effect plot for the surface roughness (Ra)

While suitable cutting conditions are critical to ensure the desired quality of machined workpiece, productivity and cost, the optimal process parameters should be judiciously selected based on the material's unique properties. Based on Response Surface Methodology Design of Experiment (RSM DOE) and previous experimental results, experimental models can be produced to predict the optimal cutting conditions satisfying the demand. The general second order polynomial model used for analyzing the parametric influences of cutting conditions on the cutting forces and the surface roughness is described as follows:

$$y = \alpha_0 + \sum_{i=1}^{k} \alpha_i x_i + \sum_{i=1}^{k} \alpha_{ii} x_i^2 + \sum_{i=1, i<j}^{k-1} \sum_{j=2}^{k} \alpha_{ij} x_i x_j + \varepsilon$$

(3)

where the variable y represents the cutting forces or the surface roughness; number k is given as 3; the symbol x_1, x_2 and x_3 represent the feedrate (mm/s), spindle speed (krpm) and volume fraction (%), respectively; the variable ε is the residual which represents the difference between the observed values (actual) and the predicted (fitted) values; α is constant coefficient.

The experimental results from Trail 1 to 15 in Table 3.1 were used to identify the related coefficients in equation (3). The identified coefficients are shown in Table 3.3. Another eight totally different trials as shown in Table 3.4 were conducted to validate models. The comparison error results in Table 3.5 show that the models are accurate enough to predict the trend of the machining responses corresponding to the input cutting conditions. Therefore, these models can be used to optimize machining operation in industry.

Table 3.3: Coefficients of the experimental models

	Cutting Force			Surface Roughness	
	F_x	F_y	F_z	R_a	R_q
α	710.350	-115.41	591.514	0.324907	0.532877
α_1	126.060	64.940	-41.600	0.260477	-0.531251
α_2	-46.659	-0.817	-55.576	0.004463	0.004154
α_3	-25.119	32.785	47.094	-0.032727	0.017798
α_{11}	0.000	0.000	0.000	0.000000	0.352320
a_{22}	0.493	0.000	0.593	0.000000	0.000000
a_{33}	0.000	-1.568	-5.766	0.003369	0.000000
α_{12}	0.000	0.000	0.000	0.000000	0.000000
α_{13}	0.000	0.000	30.500	-0.027135	0.000000
α_{23}	1.692	0.265	2.395	0.000000	-0.019198

Table 3.4: Cutting conditions for validation

Trial #	Feedrate (µm/t)	Spindle speed (rpm)	Volume fraction (%)
1	1	20	5
2	1	60	5
3	1	20	10
4	0.5	40	10
5	1.5	40	10
6	1.5	40	15
7	1	60	15
8	0.9	50	10

Table 3.5: Relative error ratio between the results of models and experiments

Trial #	Cutting Force (%)			Surface Roughness (%)	
	F_x	F_y	F_z	R_a	R_q
1	12.527	5.3870	19.484	10.417	19.470
2	16.877	1.6844	7.3793	10.013	4.610
3	11.490	6.958	15.287	4.273	14.641
4	9.380	18.698	4.647	8.536	12.380
5	6.253	4.800	11.068	9.352	1.897
6	11.182	8.409	20.548	11.756	15.888
7	11.325	2.802	4.707	13.857	14.684
8	16.286	13.041	19.105	11.342	10.945

3.6.2 Contour Plot Analysis

Contour plots derived from the models shown in equation (3) can clearly demonstrate the relationships between the parameters and guide the selection of suitable cutting conditions for specific requirements. Based on the models, contour plots of the cutting forces and the surface roughness were obtained using *Minitab 16*. Parameter relations are shown with colorful region in contour plot. For example, Figure 3.15 shows the contour plot of the cutting forces F_x regarding to spindle speed and feedrate for Composite B. It indicates that the minimal F_x exists at the region around 28,000 rpm and 0.60 μm/s with the darkest green color. Larger cutting force will be generated in the following regions, especially when spindle speed and feedrate are increasing towards upper-right corner. For different demands on the cutting force, this chart can be helpful to find the appropriate cutting conditions.
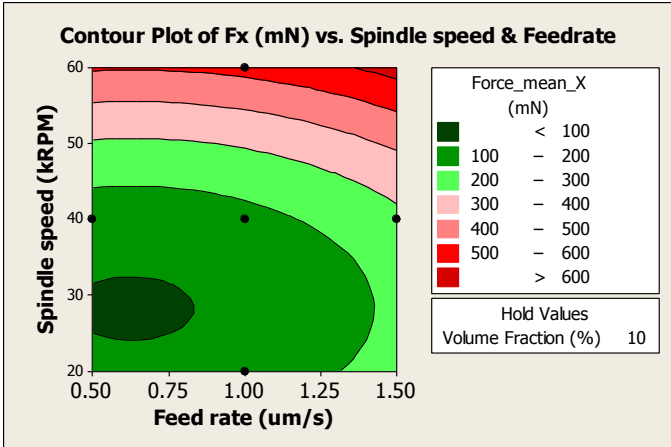
Figure 3.15: Contour plot of F_x

A contour plot of the cutting force F_y with respect to volume fraction and feedrate with fixed spindle speed (40,000 rpm) is presented in Figure 3.16. The maximum cutting force of F_y exists around the upper-right corner obviously. This implies that larger cutting force (F_y) appears when machining larger volume fraction Mg-MMCs with the same feedrate. It can be concluded that for high volume fraction application, the feedrate should be low in order to reduce the cutting force to avoid severe tool wear or even tool breakage.
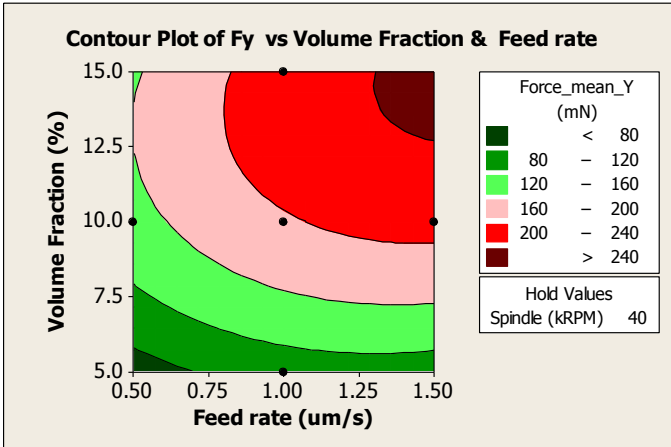
Figure 3.16: Contour plot of F_y
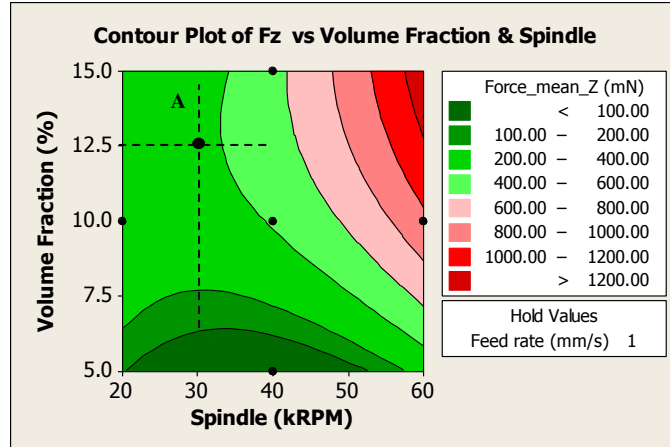
Figure 3.17: Contour plot of F_z

The contour plot for the cutting force F_z exhibits hyperbolical surface and it has a saddle point A as shown in Figure 3.17. The existence of the saddle point is likely due to the unique microstructural feature of the materials, which can be described as:

$$\lambda = d(\frac{1}{f_v^{1/3}} - 1)$$

(4)

where the inter-particle spacing (λ) is related to the particle size (d) and volume fraction (f_v). When volume fraction will be approximately 12.5%, the inter-particle spacing is approaching the average particle size. When the volume fraction is beyond 12.5%, the material will have significant changes in its mechanical behavior [15]. This saddle point coincides with this statement. It also explains the phenomenon of the steeper change of the cutting force around 10 Vol.% volume fraction shown in Figure 3.10.
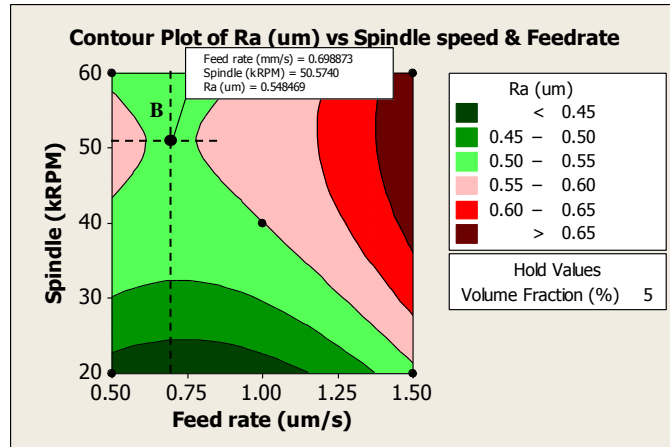
Figure 3.18: Contour plot of Ra for Composite A (5% Mg-MMC)
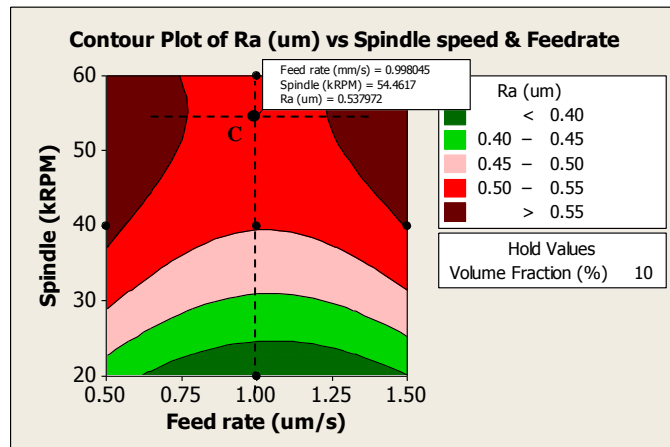
Figure 3.19: Contour plot of Ra for Composite B (10% Mg-MMC)
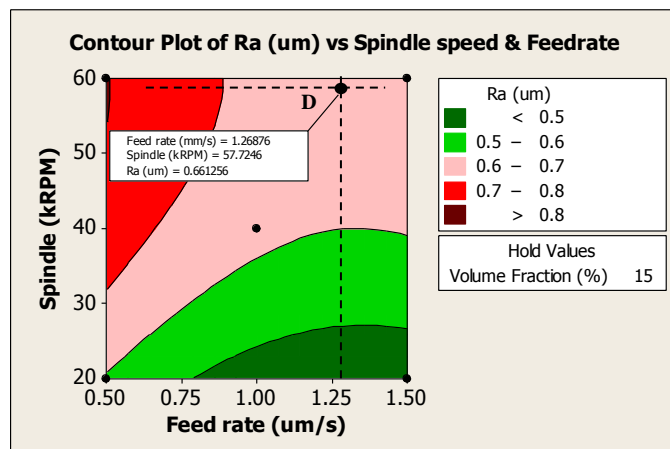
Figure 3.20: Contour plot of Ra for Composite C (15% Mg-MMC)

67

The contour plots for the surface roughness are more complicated than those for the cutting force, and every plot has a saddle point. The contour plots of bottom surface roughness for Composite A, B, C are shown in Figure 3.18, Figure 3.19 and Figure 3.20 separately. Their saddle points are Point B, C, D in sequence. Since the saddle point is the optimal cutting condition for each sample, by comparing the saddle points' position (Point B, C, D) for different Mg-MMCs samples, it is obvious that the spindle speed and feedrate of the saddle point increase with the increasing of volume fraction.

In addition, the surface roughness of Point C is the lowest compared to those of Point B and D, which verify the statement of distinct change of material properties around 10 Vol.% volume fraction again.

Consequently, all the contour plots can be combined together to determine the most applicable cutting conditions for the required cutting force and surface roughness. This method successfully builds the connection between material properties and machining performance. It will be helpful to improve productivity and the economics of the cutting process.

3.7 Summary

Experiments were conducted to investigate the machining behavior of Mg-MMC composites using micro-milling. The varied parameters in the experiments included spindle speed, feedrate and volume fraction of the reinforcing particles. Based on the measured cutting force signals and the surface roughness, the following conclusions can be reached:

1. The normal force F_x, the feed force F_y and the axial force F_z all increase with the increasing of either the spindle speed or the feedrate. The increasing rate of the axial force F_z and the normal force F_x is larger, while that of the feed force F_y is moderate for most cases.

2. The nano-particles' volume fraction has a considerable effect on the cutting force. The cutting force increases with increasing volume fraction. The largest increasing slope occurs at transition from 5 to 10 Vol.% rather than from Pure Mg to 5 Vol.% and from 10 to 15 Vol.%, which is agreeable with the sharp change of material mechanical properties around 10 Vol.%. However, when the spindle speed is increased to 60,000 rpm, the increasing rate of the cutting forces is much larger comparing with the ones when the spindle speeds are at 20,000 rpm and 40,000 rpm. The increasing slopes of the cutting forces are maintained the same at both regions of from 5 to 10 Vol.% and from 10 to 15 Vol.%.

3. The influence of a single experimental variable (feedrate, spindle speed or volume fraction) on the machined surface roughness is not obvious. The results from SEM show a decent machined surface can be achieved by micro-milling Mg-MMCs.

4. The experimental models derived by Response Surface Methodology Design of Experiment (RSM DOE) can be used to predict the cutting force and the surface roughness with different machining parameters. The related contour plots can be combined together to determine the most suitable cutting conditions for the required cutting force and surface roughness. This method builds the connection between material properties and machining performance successfully.

Further research on the effects of depth of cut, tool size and especially the microstructures of materials will improve the experimental models and make the cutting performance prediction more accurate.

CHAPTER 4   DYNAMIC CUTTING FORCE MODELING

Due to its light weight, high creep and wear resistance, Magnesium Metal Matrix Composites (Mg-MMCs) with nano-sized reinforcements are promising for various industrial applications, especially those with high volume fractions of reinforcements. The machinability of Mg-MMCs and related cutting process modeling are important to study. In this chapter, an analytical cutting force model is developed to predict cutting forces of Mg-MMC reinforced with SiC nanoparticles in micro-milling process. This model is different from previous ones by encompassing the behaviors of nanoparticle reinforcements in three cutting scenarios, i.e., shearing, ploughing and elastic recovery. By using the enhanced yield strength in the cutting force model, three major strengthening factors are incorporated, including load-bearing effect, enhanced dislocation density strengthening effect and Orowan strengthening effect. In this way, material properties, such as the particle size and volume fraction as significant factors affecting the cutting forces, are explicitly considered. To validate the model, various cutting conditions using two types of end mills (diameters as 100 μm and 1 mm) were conducted on pure Mg, Mg-MMCs with volume fractions of 5 Vol.%, 10 Vol.% and 15 Vol.%. The experimental results show a good agreement with the predicted cutting force value.

4.1 Background Introduction

Magnesium Metal Matrix Composites (Mg-MMCs), with light weight, high creep/wear resistance and bio-compatibility, are outstanding candidate materials for making miniature structural/functional components in various applications. It exhibits improved mechanical properties compared to traditional Mg-based materials, such as pure Mg and its alloys [7-9]. To shape Mg-MMCs material into required part components, mechanical machining is one of the most suitable techniques due to its high precision, 3-D flexibility, efficiency and low cost, compared to other existing manufacturing methods [10, 11].

Recently, it has been demonstrated that MMCs with high volume fractions ($\geq 10\%$) of nanoparticles exhibit even better mechanical behaviors than those reinforced with micro-sized particles, and those with low volume fractions of nano-sized reinforcements [12-14, 16, 19]. They provide better yield strength, wear resistance and shear modulus; while at the same time, also bring great challenges for machining. The machinability of Mg-MMCs reinforced with high volume fractions of nanoparticles is an important topic to study.

During the last decade, process models have been developed to predict cutting force during micro-milling [44, 89-91]. Jun *et al.* [89, 92] studied the chip formation mechanism in micro-milling and proposed a new algorithm to compute the instantaneous chip thickness by incorporating the minimum chip thickness effect. In Malekian *et al.*'s work [90], a mechanistic model of micro-milling forces was proposed. This model considered the effects of ploughing, elastic recovery, tool run-out, and focused on homogeneous materials. Vogler *et al.* [44, 91] proposed a mechanistic model that explicitly accounts for different phases during heterogeneous materials machining. The model predicted the cutting forces' higher frequencies by considering

72

the multiple phases (in micro-scale grain size) in the material model. There is however a lack in studying the machining phenomenon for nano-reinforced heterogeneous materials and modeling the resultant cutting forces.

In this chapter, an analytical cutting force model is proposed to predict cutting forces of Mg-MMC reinforced with SiC nanoparticles during micro-milling. The behaviors of those nanoparticle reinforcements are modeled and analyzed in three cutting regimes: elastic recovery zone, ploughing zone and shearing zone. Material properties, including volume fraction and particle size, are explicitly taken into account in this model by considering the various strengthening effects of the nanoparticles.

The remainder of the chapter is organized as follows. Section 4.2 presents the details of experimental setup. Section 4.3 summarizes the cutting force model formulation. Section 4.4 discusses the calibration of force coefficients and model validation. Section 4.5 summarizes the result analysis and delivers the conclusion.

4.2 Experimental Preparation

In order to prepare the magnesium metal matrix composite material (Mg-MMCs) reinforced with SiC nanoparticles, Magnesium powder of 98% purity with a mean diameter of 30 µm (from Alfa Aesar Corporation) was used as the matrix material. Nano-sized SiC particles with a mean diameter of 20 nm (from MTI Corporation) were employed as the reinforcements. Both powders with desired volume fractions were mixed using high energy ball milling (SPEX

8000M miller) for 20 hours to ensure the uniform distribution of SiC nanoparticles within the Mg matrix. The obtained powder mixtures were sintered by Spark Plasma Sintering (SPS) technique at 600 ^{o}C for 5 minutes. The SPS system used in this study is DR. SINTER (Model SPS-1030, SPS Syntex Inc., Kanagawa, Japan). The densities of the resultant composites all reached their theoretical values, which are 1.8, 2.0 and 2.0 g/cm^{3}, for the composites with 5 Vol.%, 10 Vol.% and 15 Vol.% SiC nanoparticles, respectively.

The micro-milling machine is set up on a tetrahedral frame, as shown in Figure 4.1. The feed system of the machine is composed of three precision linear stages along X, Y and Z axes (Aerotech ALS130H-150 for X-Y axes and AVL125 for Z axis). A multi-axis motion controller (Aerotech Ensemble Epaq) is utilized to control the accurate machining position. The motion resolution of the X-Y axes is 4 nm and the corresponding motion accuracy is ± 0.25 μm. A 300W air-bearing electric motor spindle (NSK E800Z) is fixed at the center of the tetrahedral frame. Its highest rotational speed is 80,000 rpm with the static runout error less than 1 μm. A Kistler 9256C2 triaxial piezoelectric dynamometer is used to measure instant cutting forces along X, Y and Z directions. The vibration of the machining tetrahedral platform is measured by a PCB triaxial piezoelectric ICP accelerometer, which is mounted at the spindle holder. A National Instrument (NI) PXI-based Data Acquisition (DAQ) system (including NI PXI-8106 and PXI-4496) is used to take measurements and online control.
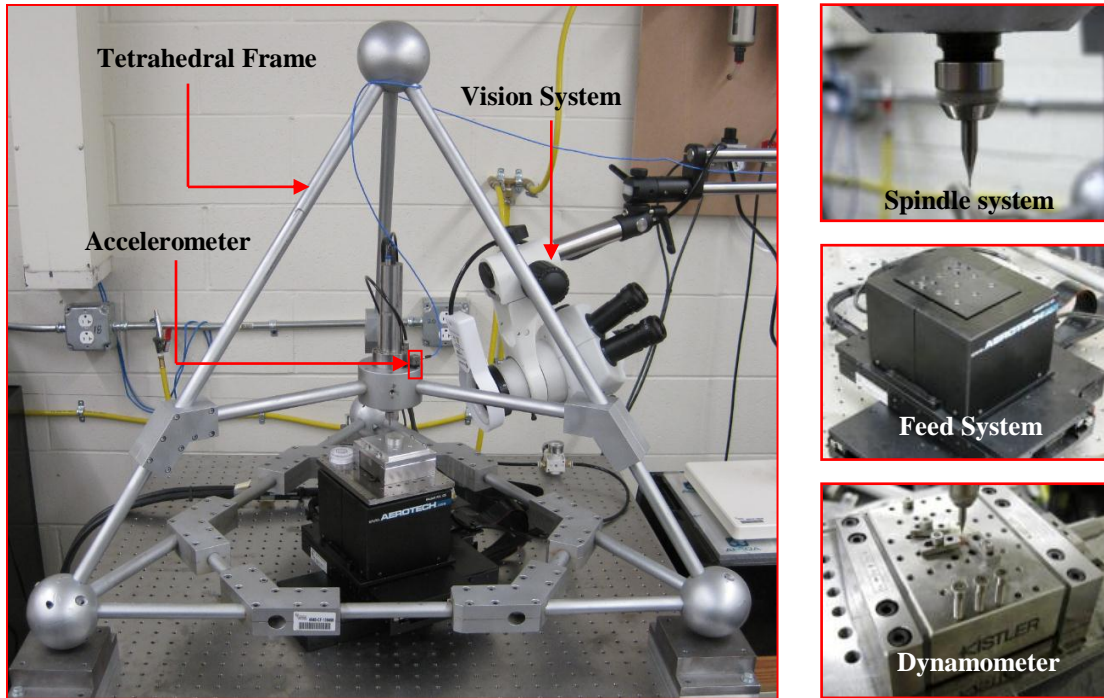
Figure 4.1: Micro-milling machine platform

Two-flute uncoated solid carbide end mills with diameter of 1 mm were used to conduct the experiments listed in Figure 4.1. A new cutting tool was used each time when changing materials. The 18 full immersion cutting conditions were conducted on all materials (pure Mg, Mg-MMCs with volume fractions of 5 Vol.%, 10 Vol.% and 15 Vol.%) and each experiment was repeated three times. The purpose of these 18 cutting conditions is to achieve the nominal feed per tooth in a large range of 0.15-10 μm/t. In our experimental platform, feed speed was constrained within the range of 0.2-1.0 mm/s. Spindle speed was adjusted in the range of 1500-70000 RPM. Both feedrate and spindle speed were varied randomly in order to avoid systematic errors. The axial depth of cut was fixed at 20 μm. During experiments, the 18 cutting conditions were executed randomly by Design of Experiments method in the software Minitab 16. Feed direction is the X direction.

Table 4.1: Experimental cutting conditions

Trial No.	Feed speed (mm/s)	Spindle Speed (RPM)	Nominal f_t (μm/t)
1	0.4	70,000	0.1714
2	0.5	65,000	0.2308
3	0.5	50,000	0.3000
4	0.5	35,000	0.4286
5	0.5	30,000	0.5000
6	0.2	9,000	0.6667
7	1.0	40,000	0.7500
8	0.2	7,500	0.8000
9	1.0	35,000	0.8571
10	0.2	6,500	0.9231
11	1.0	25,000	1.2000
12	1.0	20,000	1.5000
13	0.4	6,000	2.0000
14	0.4	4,000	3.0000
15	0.5	3,500	4.2857
16	0.5	2,500	6.0000
17	0.5	2,000	7.5000
18	0.5	1,500	10.0000

4.3 Analytical Model Development

4.3.1 Size Effect and Minimum Chip Thickness of Mg-MMCs

Size effect and minimum chip thickness significantly affect the micro-milling performance in terms of cutting forces, tool wear, and machined surface integrity [59, 66, 100]. In micro-scale milling, both shearing and ploughing mechanisms play significant roles during machining [90, 94]. However, heterogeneous materials exhibit different phenomenon during micro-milling from homogeneous materials regarding the size effect and minimum chip thickness effect.

Figure 4.2 and Figure 4.3 show the specific cutting energy trends for pure Mg and Mg-MMCs with volume fraction of 10 Vol.%, respectively. The horizontal axis represents the nominal feed per tooth (uncut chip thickness). The vertical axis represents the specific cutting

76

energy. The Root Mean Square (RMS) values of in-plane cutting force ($F_{inplane} = \sqrt{F_x^2 + F_y^2}$) were calculated for the 18 different cutting conditions (Table 4.1). The specific cutting energy is calculated via dividing the RMS cutting force by the feed per tooth f_t and depth of cut d_a. Three cutting regions were formed with different dominant cutting mechanisms [89, 90]. The cutting energy in Region I and III changes linearly with the nominal feed per tooth. Region I is the elastic recovery zone and Region III denotes the traditional shearing zone. In Region II, ploughing plays the most important role, with a small portion of elastic recovery phenomenon.
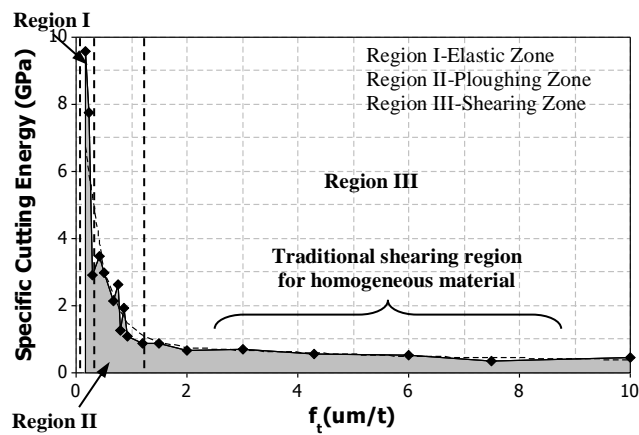
Figure 4.2: Specific cutting energy vs. nominal feed per tooth for Pure Mg
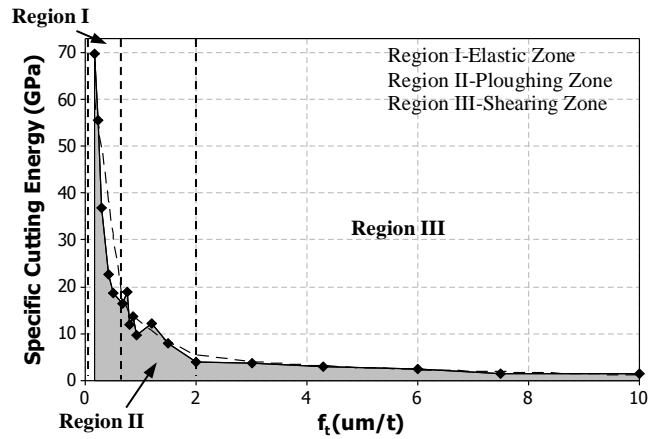
Figure 4.3: Specific cutting energy vs. nominal feed per tooth for 10Vol.% Mg-MMCs

By comparing Figure 4.2 and Figure 4.3, it can be seen that:

- Due to particle strengthening effect, much more energy is needed to cut the Mg-MMCs with volume fraction of 10 Vol.% than cut pure Mg. The peak value when cutting the 10 Vol.% Mg-MMCs in the elastic zone is around 70 GPa; while it is around 10 GPa when cutting pure Mg.

- Both the elastic zone and the ploughing zone are wider when cutting the 10 Vol.% Mg-MMCs than cutting pure Mg.

In summary, micro-milling Mg-MMCs, especially with high volume fractions of nanoparticle reinforcements, is significantly different from micro-milling pure magnesium material, and the cutting force model need to be systematically studied and formulated.

4.3.2 Instantaneous Chip Formation

In order to accurately compute the chip thickness, a comprehensive model including the effect of minimum chip thickness [89, 91, 94] is utilized in this work. Three cutting mechanisms

78

influence the overall material removal process and the behavior of the SiC nanoparticles during the machining process:

- When the instantaneous uncut chip thickness t_c is smaller than the elastic recovery threshold t_{er}, only elastic deformation occurs and the deformed material will fully recover to its original position. The SiC nanoparticles comply with the same elastic deformation as the Mg matrix and will fully recover to the original positions after cutting.

- As t_c increases to be larger than t_{er}, the elastic-plastic deformation becomes dominant. In this region, it is assumed that a constant percentage p_e of the workpiece material undergoes elastic deformation. The remaining material experiences plastic deformation. In this case, the SiC particles cannot recover to their original positions. Since plastic deformation occurs in this region, the matrix-particle interface will be damaged and leads to particle displacements [37].

- When t_c increases to be larger than the minimum chip thickness t_{min}, the shearing mechanism plays a major role and continuous chips will form. In this situation, the elastic recovery rate p_e drops to 0. The SiC particles in the chips and the uncut material will retain their original relative positions locally. Although the particles in the cohesive zones still have fractures and displacements, this effect is neglectable compared to the shearing effect.
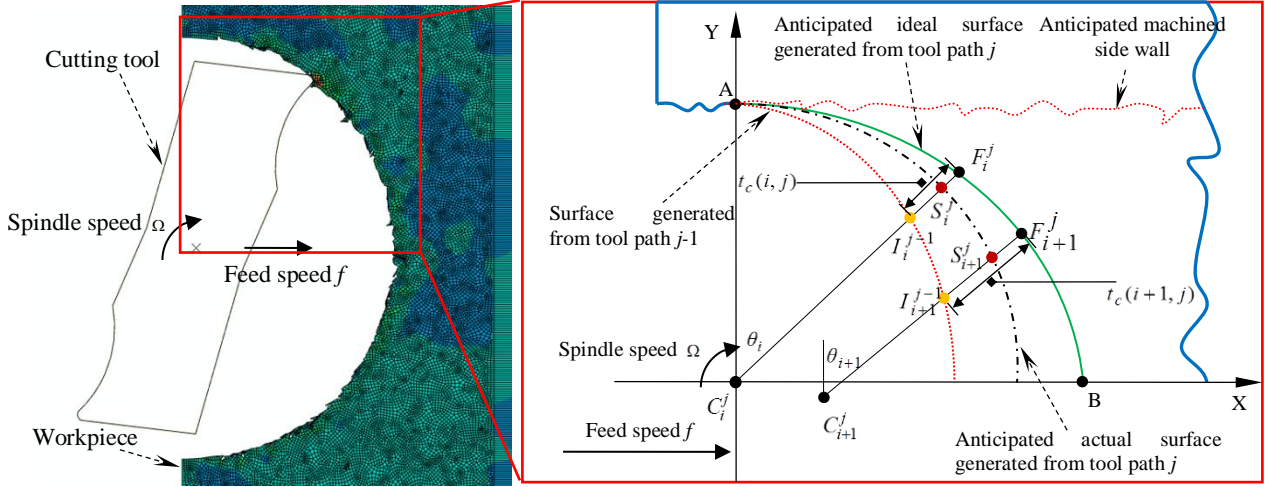
Figure 4.4: Diagram of instantaneous chip thickness calculation

Figure 4.4 is a diagram showing the continuous cutting process, where the instantaneous chip thickness at the rotational angle θ_i and the tool path j is determined as [89]:

$$t_c(i,j) = \max(0, \left\| C_i^j F_i^j \right\| - \left\| C_i^j I_i^{j-1} \right\|)$$

(5)

where C_i^j and F_i^j are the tool center and cutting edge coordinates; I_i^{j-1} is the intersection between the line $C_i^j F_i^j$ and the surface generated at the previous tool path $j-1$. The locations of the machined surface point S_i^j can be expressed as [89]

$$x_{S_i^j} = x_{F_i^j} - \frac{t_c(i,j) \cdot \kappa}{R}(x_{F_i^j} - x_{C_i^j})$$

(6)

$$y_{S_i^j} = y_{F_i^j} - \frac{t_c(i,j) \cdot \kappa}{R}(y_{F_i^j} - y_{C_i^j})$$

(7)

where R is the cutting tool radius, x_C and y_C are coordinates of the cutting tool center, x_F and y_F are the coordinates of the cutting tool edge, x_S and y_S are coordinates of the generated surface point, κ is the overall elastic recovery rate as [89]

80

$$\kappa = \begin{cases} 1.0 & \text{when} & t_c < t_{ce} \\ p_e & \text{when} & t_{ce} \leq t_c < t_{\min} \\ 0 & \text{when} & t_c \geq t_{\min} \end{cases} \tag{8}$$

In our study, the elastic recovery rate of the material p_e is assumed to be 15%. A simulated chip thickness plot is shown in Figure 4.5, where the nominal feed per tooth is 4 μm/t and the spindle speed is 50,000 rpm. The tool runout amplitude is set as 2 μm.
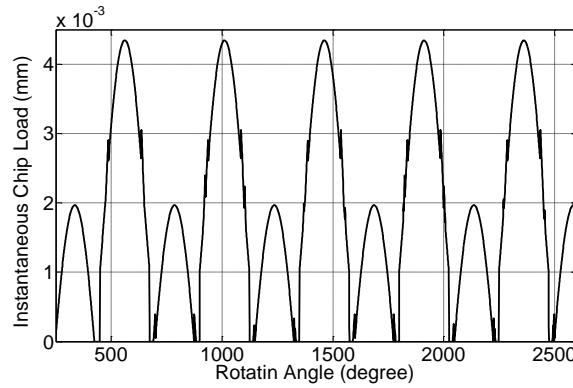
Figure 4.5. Simulated instantaneous chip load using 2-flute end mill

4.3.3 Cutting Force Model

In our study, cutting force models are developed for the three cutting regimes for Mg-MMCs. The tangential force F_t, radial force F_r and axial force F_a are modeled using differential forms. The tool deflection is assumed to be very small and neglectable for larger diameter cutting tools (> 500 μm). For smaller tools, constant tool deflection parameters are applied. Tool wear is not considered in the model. The cut length is 3 mm for each test. The tool edge radii are considered to be the same for different cutting tests.

Elastic Recovery Zone

In the elastic recovery dominant regions, particle displacement can be neglected, since the majority of the reinforcement particles in the uncut workpiece materials retain their original relative positions (Figure 4.6).

In Figure 4.6, the cutting tool moves from right to left. The hollow circles represent SiC particles in the Mg matrix. The solid-colored circles represent those particles under elastic deformation. The oblique-line filled circles represent those reinforcement particles just recovered to their original position.
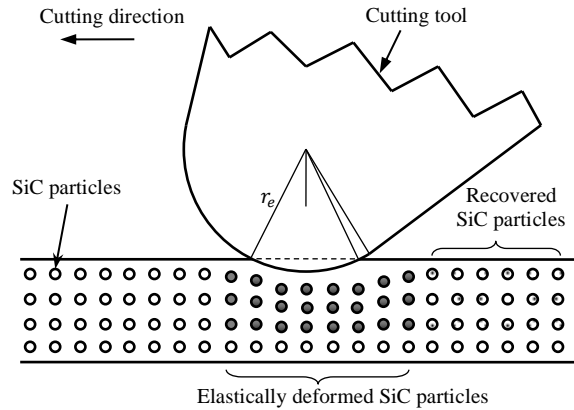
Figure 4.6: Particle displacement in the elastic recovery zone

The differential cutting forces are formulated in Equation (9) for this zone, where the end mill is discretized into axial slices and uncut chip thickness is computed for the teeth of each slice.

$$
\begin{aligned}
dF_t &= K_{te} \cdot t_c \cdot dz \\
dF_r &= K_{re} \cdot t_c \cdot dz \\
dF_a &= K_{ae} \cdot t_c \cdot dz
\end{aligned}
\tag{9}
$$

where K_{te}, K_{re} and K_{ae} are tangential, radial and axial force coefficients in the elastic recovery zone. The term dz is the thickness of the axial slices. In this study, the cutting force coefficients are assumed to be equivalent to the specific cutting energy since they have the same dimension. As can be seen in Figure 4.3, in Region I, the specific cutting energy exhibits a linear relation with the nominal uncut chip thickness, therefore these coefficients are linear to uncut chip thickness t_c:

$$
\begin{aligned}
K_{te} &= K_{te1} \cdot t_c + K_{te2} \\
K_{re} &= K_{re1} \cdot t_c + K_{re2} \\
K_{ae} &= K_{ae1} \cdot t_c + K_{ae2}
\end{aligned}
\tag{10}
$$

where K_{te1}, K_{te2}, K_{re1}, K_{re2}, K_{ae1}, K_{ae2} are constants and can be obtained by optimizing the measured cutting force data using the least-square method.

Ploughing Zone

When the uncut chip thickness t_c increases beyond t_{er} but less than the minimum chip thickness, the workpiece deforms both elastically and plastically at the same time. No material is sheared off from the workpiece. From Figure 4.3, the specific cutting energy exhibits an exponential relation with the nominal uncut chip thickness t_c. Therefore, the force coefficients are assumed to be exponential functions to the ploughing area A_p as:

$$
\begin{aligned}
K_{tp} &= K_{tp1} \cdot (A_p)^{K_{tp2}} \\
K_{rp} &= K_{rp1} \cdot (A_p)^{K_{rp2}} \\
K_{ap} &= K_{ap1} \cdot (A_p)^{K_{ap2}}
\end{aligned}
\tag{11}
$$

where K_{tp}, K_{rp} and K_{ap} are the force coefficients of tangential, radial and axial directions in the ploughing zone. K_{tp1}, K_{tp2}, K_{rp1}, K_{rp2}, K_{ap1}, K_{ap2} are constants and can be calculated by nonlinearly optimizing the averaged cutting force data.

83

Ploughing force is more dependent on the ploughing area A_p, which is a function of uncut chip thickness t_c.

In the ploughing dominant region in Figure 4.7, particle displacement can not be ignored. A comprehensive model for ploughing area was developed in [90]. The ploughed area A_p is expressed by area S_{ACE}. The symbol t_{er} is the elastic recovery thickness. The symbol ψ_e denotes the clearance angle of the tool. Geometric angles α_p and ψ_e can also be expressed by $\angle CBE$ and $\angle DBE$, respectively. Angle ψ_t is $\angle ABD$ in Figure 4.7(a) and angle ψ_s is $\angle ABE$ in Figure 4.7(b).
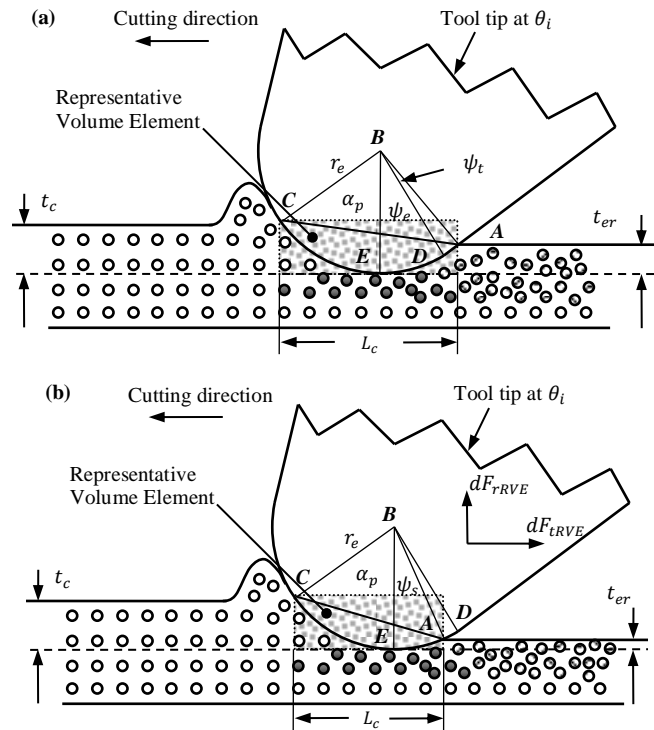
Figure 4.7: Particle displacement in the ploughing zone (a) deeper immersion and (b) shallower immersion

When $t_{er} \geq r_e(1 - \cos\psi_e)$ (Figure 4.7(a)), the ploughed area A_p is expressed as [90]:

84

$$A_p = \frac{1}{2}[r_e^2(\alpha_p + \psi_e) + r_e l_{AD} - r_e l_{AB} \sin(\alpha_p + \psi_e + \psi_t)] \tag{12}$$

where,

$$l_{AD} = \frac{t_{er} - r_e(1 - \cos\psi_e)}{\sin\psi_e}$$

$$l_{AB} = \sqrt{r_e^2 + l_{AD}^2}$$

$$\alpha_p = \cos^{-1}(1 - \frac{t_c}{r_e}) \tag{13}$$

$$\psi_t = \tan^{-1}(\frac{l_{AD}}{r_e})$$

When $t_{er} < r_e(1 - \cos\psi_e)$ (Figure 4.7(b)), the ploughed area A_p is expressed as [90]:

$$A_p = \frac{1}{2}r_e^2(\alpha_p + \psi_s - \sin(\alpha_p + \psi_s)) \tag{14}$$

where,

$$\psi_s = \cos^{-1}(1 - \frac{t_{er}}{r_e}) \tag{15}$$

As seen from Figure 4.7, the reinforcement particles inside the Mg-MMCs are assumed to undergo elastic-plastic deformations due to ploughing and SiC particles cannot return to their original local positions after being ploughed. This implies that the particles experienced certain displacement. A rectangular Representative Volume Element (RVE), which is shaded in Figure 4.7, is proposed to reflect this local mechanistic effect. It is certain that in the ploughing region, the local materials are experiencing deformations from an elastic manner to a plastic manner. Therefore, the overall yield stress value of the RVE is used to calculate the force components (dF_{rRVE} and dF_{tRVE}) due to the strengthening effect. Assuming that the SiC particles are uniformly distributed and the grain size effect is neglectable, the cutting force acting on the RVE can be expressed as

$$\begin{cases} dF_{rRVE} = \sigma_{ys} \cdot L_c \cdot dz \\ dF_{tRVE} = \sigma_{ys} \cdot t_c \cdot dz \end{cases} \tag{16}$$

where L_c is the length of ploughed area, and is expressed as:

$$L_c(t) = \begin{cases} (r_e - t_c)\tan\alpha_p + (r_e - t_{er})\tan(\psi_t + \psi_e) & Fig.4.7(a) \\ (r_e - t_c)\tan\alpha_p + (r_e - t_{er})\tan\psi_s & Fig.4.7(b) \end{cases} \tag{17}$$

There are three major strengthening factors in particle-reinforced metal matrix nanocomposites: load-bearing effect, enhanced dislocation density strengthening effect, and Orowan strengthening effect [52]. An analytical model for predicting the yield strength of the metal matrix nanocomposites has been developed based on these three strengthening effects, which is expressed as [52]:

$$\sigma_{ys} = \sigma_{ym}(1 + f_l)(1 + f_d)(1 + f_{Orowan}) \tag{18}$$

where,

$$f_l = \frac{1}{2}V_f$$

$$f_d = \frac{1.25G_m b}{\sigma_{ym}} \sqrt{\frac{12(T_{process} - T_{test})(\alpha_m - \alpha_p)V_f}{bd_p(1 - V_f)}} \tag{19}$$

$$f_{Orowan} = \frac{0.13G_m b}{\sigma_{ym}d_p[(0.5V_f)^{1/3} - 1]}\ln\frac{d_p}{2b}$$

where σ_{ys} is the improved yield strength of Mg-MMCs, σ_{ym} is the yield strength of the Magnesium matrix. The symbols f_l, f_d and f_{Orowan} are the improvement factors due to the load-bearing effect, enhanced dislocation density effect and Orowan effect, respectively. The symbol V_f denotes the volume fraction of the reinforcement particles and d_p is the average particle size. G_m is the shear modulus of the matrix, b is the magnitude of the Burgers vector of dislocation in the matrix, $T_{process}$ is the processing temperature when fabricating the material, and T_{test} is the test

temperature when testing the material. The symbols α_m and α_p represent the coefficients of thermal expansion of the matrix and reinforcement phase, respectively. Including this reinforced yield strength of Mg-MMCs σ_{ys} into the cutting force model to compensate for the local heterogeneity of material, and the modified cutting force model in the ploughing zone is derived as:

$$
\begin{aligned}
dF_t &= (K_{tp} \cdot t_c + \sigma_{ys} \cdot t_c) \cdot dz \\
dF_r &= (K_{rp} \cdot t_c + \sigma_{ys} \cdot L_c) \cdot dz \\
dF_a &= K_{ap} \cdot t_c \cdot dz
\end{aligned}
\tag{20}
$$

Shearing Zone

In the shearing region, the particle displacement can be neglected, since the majority of the reinforcement particles in the formed chips retain their original relative positions.

In Figure 4.8, the majority of particles retain their original local positions during cutting, no matter whether they are in the formed chips (above tool) or in the uncut material (under tool), marked as gray-shaded particles. The hollow circles represent those reinforcement particles which facilitate the generation of new surfaces and undergo displacement. However, compared to the volume of gray-shaded particles in the formed chips and uncut material surface, the displaced particles are minimum and affect cutting force insignificantly. Therefore, particle displacement effect is ignored in this region.
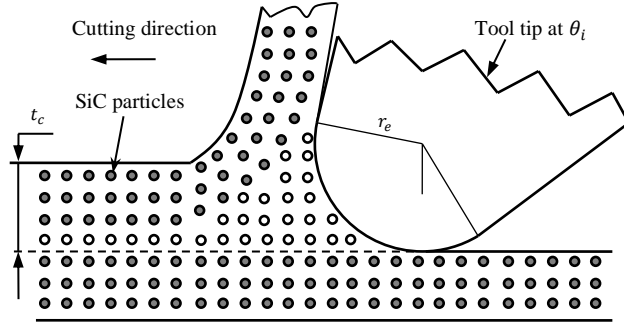
Figure 4.8: Particle displacement in the shearing zone

According to Figure 4.3, the specific cutting energy is linear to the nominal uncut chip thickness. The three force components are described as:

$$
\begin{aligned}
dF_t &= K_{ts} \cdot t_c \cdot dz \\
dF_r &= K_{rs} \cdot t_c \cdot dz \\
dF_a &= K_{as} \cdot t_c \cdot dz
\end{aligned}
\tag{21}
$$

where K_{ts}, K_{rs} and K_{as} are tangential, radial and axial force coefficients in the shearing zone. These coefficients are linear to uncut chip thickness t_c and can be calculated by optimizing the measured cutting force data.

$$
\begin{aligned}
K_{ts} &= K_{ts1} \cdot t_c + K_{ts2} \\
K_{rs} &= K_{rs1} \cdot t_c + K_{rs2} \\
K_{as} &= K_{as1} \cdot t_c + K_{as2}
\end{aligned}
\tag{22}
$$

where K_{ts1}, K_{ts2}, K_{rs1}, K_{rs2}, K_{as1}, K_{as2} are constants defined for K_{ts}, K_{rs} and K_{as} of the linear relationship.

4.4 Experimental Validation

4.4.1 Model Calibration

In order to model cutting forces for Mg-MMCs, cutting force coefficients should be first calibrated. The piezoelectric dynamometer (Kistler 9256C2) was calibrated and its frequency response was determined using impact hammer test. The dynamics of the sensing system was measured using the instrumented impact hammer (PCB-086C03) and the dynamometer. The sensitivity of the hammer and dynamometer (X/Y direction) are 2.25 mV/N and 26 pC/N, respectively.

In this study, the spindle frequency and tooth-passing frequency are the two most concerned components of the cutting forces in frequency domain. The tooth-passing frequency of a two-flute cutting tool at maximum spindle speed of 70,000 rpm is around 2,333 Hz, which is within the bandwidth range. Figure 4.9 shows the dynamic response of the dynamometer along X direction from the impact hammer test, where the bandwidth of the dynamometer is approximately 3,300 Hz. So the dynamometer is adequate to accurately measure the cutting force.
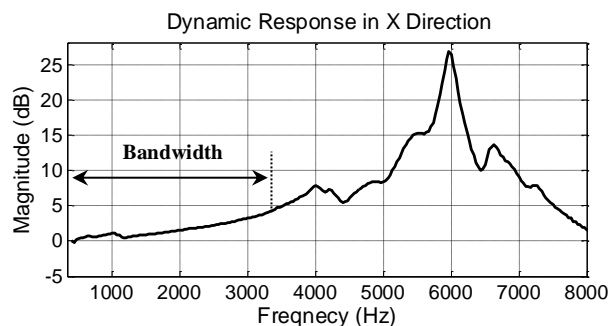
Figure 4.9: Dynamic response in the X direction of the dynamometer from the impact hammer test

Experimental cutting force is measured in order to calibrate cutting force coefficients. Based on the local coordinate transformation:

$$\begin{bmatrix} dF_x(i) \\ dF_y(i) \\ dF_z(i) \end{bmatrix} = \begin{bmatrix} -\cos\theta & -\sin\theta & 0 \\ \sin\theta & -\cos\theta & 0 \\ 0 & 0 & 1 \end{bmatrix} \begin{bmatrix} K_t(\overline{t_c}) \\ K_r(\overline{t_c}) \\ K_a(\overline{t_c}) \end{bmatrix} \overline{t_c} dz \tag{23}$$

and considering the geometric conditions,

$$dz = \frac{r}{\tan\beta} d\theta \tag{24}$$

where β is the helical angle. The Root Mean Square (RMS) averaged cutting force for the nominal feed per tooth $\overline{t_c}$ can be expressed as [96]

$$\begin{bmatrix} \overline{F_x(\overline{t_c})} \\ \overline{F_y(\overline{t_c})} \\ \overline{F_z(\overline{t_c})} \end{bmatrix} \cong \frac{R \cdot \overline{f_t}}{\tan\beta} \cdot \begin{bmatrix} A & -B & 0 \\ B & A & 0 \\ 0 & 0 & -C \end{bmatrix} \begin{bmatrix} K_t(\overline{t_c}) \\ K_r(\overline{t_c}) \\ K_a(\overline{t_c}) \end{bmatrix} \tag{25}$$

where A, B, and C denoting the integral results are given as:

$$A = \frac{1}{4} \sum_{i=1}^{N} \cos(2\theta)\Big|_{\theta_s}^{\theta_e}$$

$$B = \frac{1}{4} \sum_{i=1}^{N} [2\theta - \sin(2\theta)]\Big|_{\theta_s}^{\theta_e} \tag{26}$$

$$C = \sum_{i=1}^{N} \cos(\theta)\Big|_{\theta_s}^{\theta_e}$$

where θ_s and θ_e denote the start angle and exit angle of each immersion. Symbol N denotes the number of teeth. When dividing the RMS averaged cutting force components by the product of $\overline{f_t}$ and depth of cut d_a, the specific cutting energy $K_{x,y,z}(\overline{f_t})$ can be directly calculated from the measured cutting force.

$$\begin{bmatrix} K_x(\overline{f}_t) \\ K_y(\overline{f}_t) \\ K_z(\overline{f}_t) \end{bmatrix} = \frac{R}{d_a \cdot \tan\beta} \cdot \begin{bmatrix} A & -B & 0 \\ B & A & 0 \\ 0 & 0 & -C \end{bmatrix} \begin{bmatrix} K_t(\overline{t}_c) \\ K_r(\overline{t}_c) \\ K_a(\overline{t}_c) \end{bmatrix} \qquad (27)$$

Figure 4.10 shows the experimental result of the relationship between the specific cutting energy and the nominal feed per tooth for 10 Vol.% Mg-MMCs. During experiments, the average of all three replicates for a single f_t value was used to characterize the specific cutting energy.
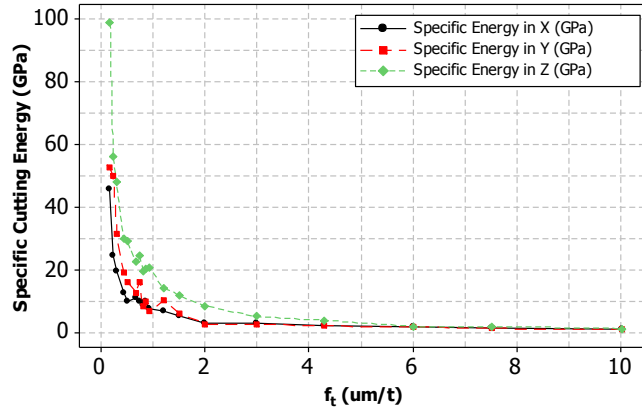
Figure 4.10: Specific cutting energy for 10 Vol.% Mg-MMCs

Two critical values t_{er} and t_{min} can be determined by measuring the slope of the curve in the plot for X-Y plane norm specific cutting energy in Figure 4.3. The determined values for the four different materials are summarized in Table 4.2.

Table 4.2: Minimum chip thickness t_{min} and t_{er} values

Material	Pure Mg	Composite A	Composite B	Composite C
t_{er} (μm)	0.43	0.51	0.85	0.49
t_{min} (μm)	1.2	2.01	2.02	2.00

The nominal values of K_r, K_t and K_a can be obtained from Equation (27) by the inverse of the coefficient matrix. The cutting force coefficients calibrated for the composites are listed in Table 4.3.

Table 4.3: Identified cutting force coefficients

	Composite A		Composite B		Composite C	
	$K_{i,1}$	$K_{i,2}$	$K_{i,1}$	$K_{i,2}$	$K_{i,1}$	$K_{i,2}$
K_{er}	-330.75	172.38	-687.96	388.61	-786.99	783.15
K_{et}	-336.20	194.60	-886.72	537.94	-880.76	662.53
K_{ea}	-60.55	42.22	-291.36	177.19	-237.59	239.91
K_{pr}	33.14	-0.74	51.52	-0.83	176.61	-0.87
K_{pt}	35.58	-1.08	56.07	-1.24	89.30	-1.18
K_{pa}	12.19	-0.72	25.80	-0.85	62.68	-0.80
K_{sr}	-0.43	7.08	-1.97	25.12	-3.79	43.34
K_{st}	-0.22	4.47	-1.68	22.70	-2.65	37.01
K_{sa}	-0.12	2.08	-1.26	12.60	-3.73	32.92

As for the parameters in Equation (18), the following parameter values from references [62, 122] are used in this study: $\sigma_{ym} = 97\text{MPa}$, $G_m = 165\text{GPa}$, $b = 0.32\text{nm}$, $\alpha_m = 28.4 \times 10^{-6} (°C)^{-1}$, $\alpha_p = 4.3 \times 10^{-6} (°C)^{-1}$, $d_p = 20\text{nm}$, $V_f = 0 \sim 15$ Vol.%, $T_{process} = 600°C$ and $T_{test} = 40°C$.

For the cutting tool geometry, helical angle β and clearance angle ψ_e are $30°$ and $15°$ obtained from the manufacturer. Tool edge radius r_e was measured using Scanning Electronic Microscope (SEM) before each cutting test (as shown in Figure 4.11). An average value of 1.0 μm was used in the simulation.
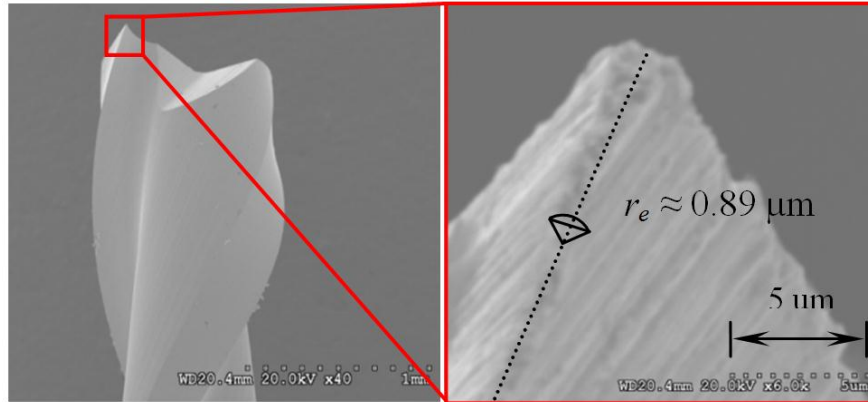
Figure 4.11: Measured tool edge radius

4.4.2 Model Validation and Results Analysis

In order to validate the proposed cutting force models, three representative cutting conditions were set up to machine the pure Mg and 10 Vol.% Mg-MMCs. One is chosen to be mainly in the shearing region and the other is chosen to be mainly in the ploughing region.

The instantaneous cutting force simulated in time domain was compared with experimental data. The results imply that the proposed model can predict the cutting forces with satisfactory accuracy and thus clearly reflect the effect of reinforcement nanoparticles on instantaneous cutting forces.

Case I: spindle speed is 4,000 RPM, feed speed is 0.4 mm/s (f_t = 3.0 μm/t) and depth of cut is 20 μm using 1 mm diameter end mill.

Figure 4.12 shows the experimental and simulated forces for pure Mg along X, Y and Z directions. The yield strength of pure Mg was directly applied to Equation (18) in the model. It can be seen that the model can fairly accurately predict the forces. The agreement between the data of F_z is not as good as F_x and F_y. This is mainly because the magnitude of F_z is close to that

93

of the noise signal. In this case, the noise has significant influences on the profile of cutting force F_z.
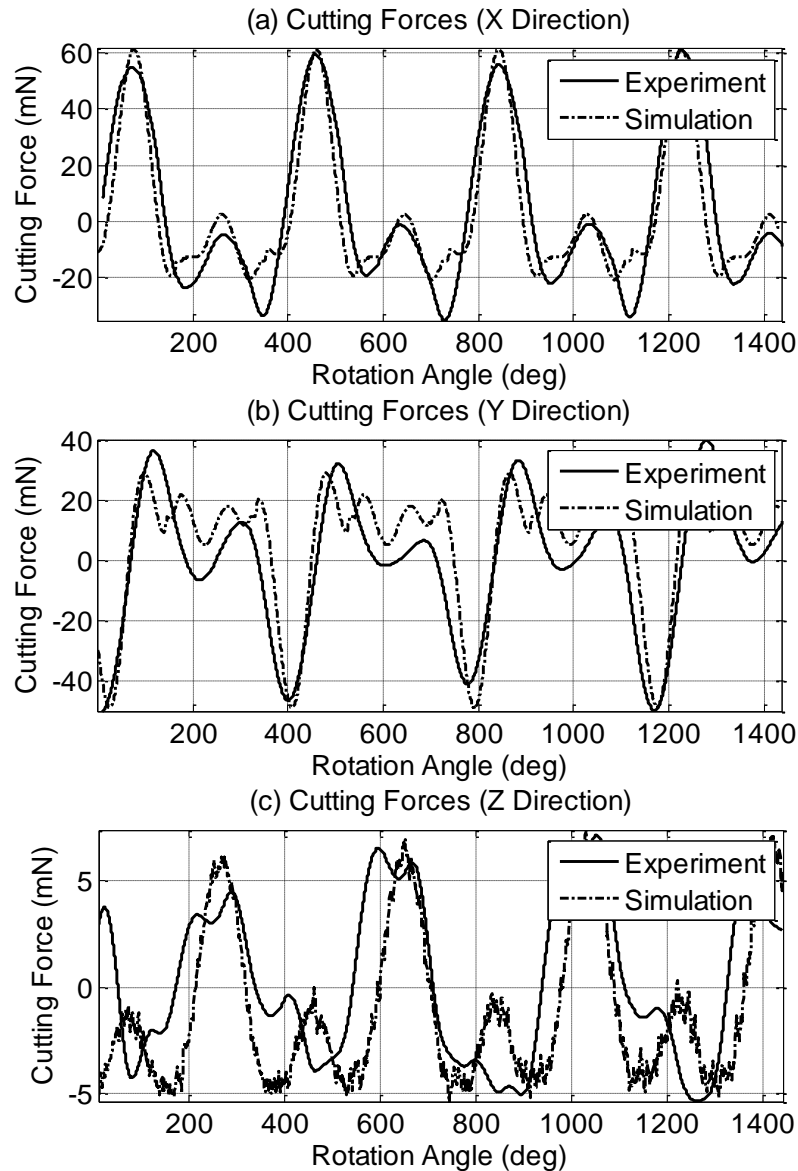
Figure 4.12: Comparison of experimental and simulated cutting forces (on pure Mg)

Figure 4.13 illustrates the experimental and simulated cutting forces for 10 Vol.% Mg-MMCs. Due to the nanoparticles reinforcement effect, the force magnitudes greatly increase as

the volume fraction is varied from 0 Vol.% to 10 Vol.%. This is attributed to the improved yield

strength and fracture strength by adding the nanoparticles.
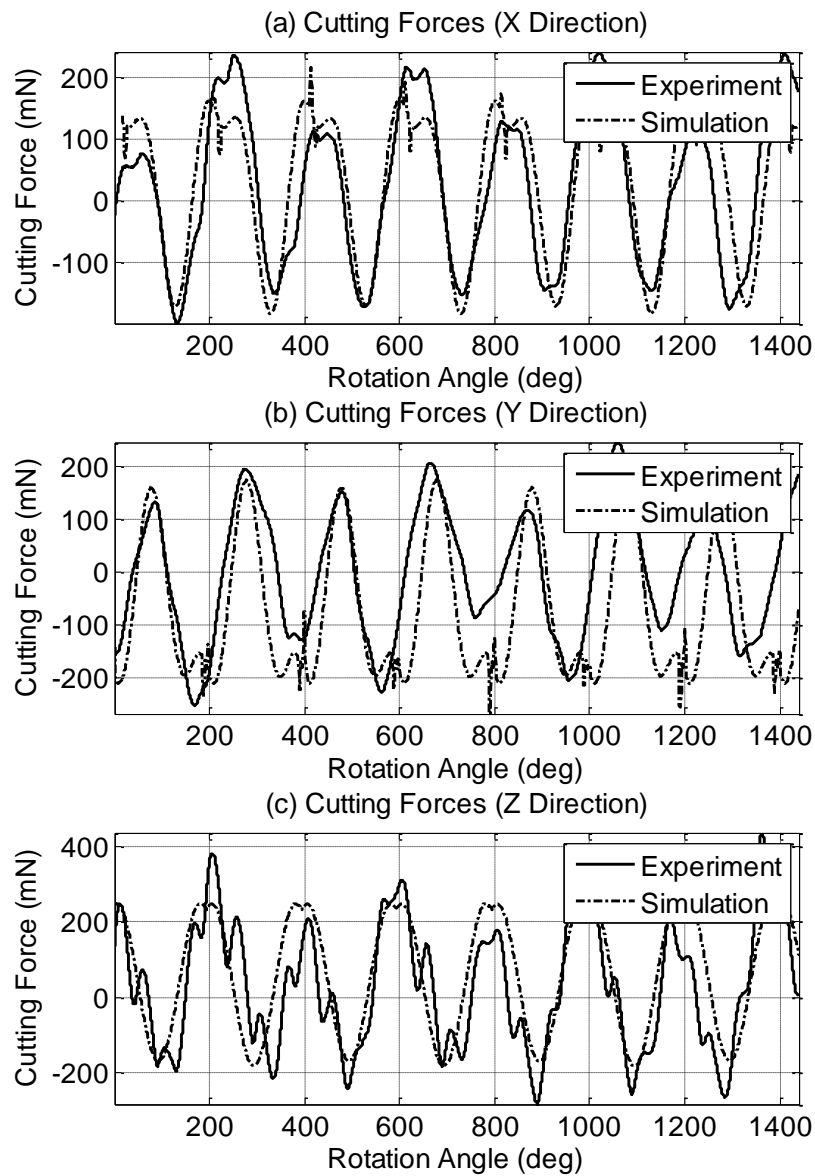
Figure 4.13: Comparison of experimental and simulated cutting forces (on 10 Vol.% Mg-MMCs)

Case II: spindle speed is 35,000 RPM, feed speed is 1.0 mm/s ($f_t = 0.857$ μm/t) and depth of cut is 20 μm using 1 mm diameter end mill.

Figure 4.14 shows the experimental and simulated cutting forces for 10 Vol.% Mg-MMCs. From Table 4.2, the f_t value in cutting condition in Case II leads the cutting to the ploughing-dominant regime. Thus, the cutting force profiles become more complex than that of the shearing-dominant regime. However, the proposed model can also track the significant variations of the force values in all three directions.

The cutting force magnitude of F_x and F_y does not change much, while the magnitude of F_z increases significantly as the feed per tooth decreases from 3.0 to 0.857 μm/t. The possible reason is that the bottom of the flutes of the end mill also experienced different cutting mechanism during cutting. This effect of the bottom of the flutes is not explicitly included in this model. Additionally, except the traditional shearing-dominant regime in homogenous materials (e.g. cutting condition in Case II for pure Mg), all other tested cutting conditions on pure Mg and all the tested cutting conditions on Mg-MMCs resulted in larger F_z values. Similar results were also found in our previous work [113]. This phenomenon can also be attributed to the effect of bottom of the flutes.
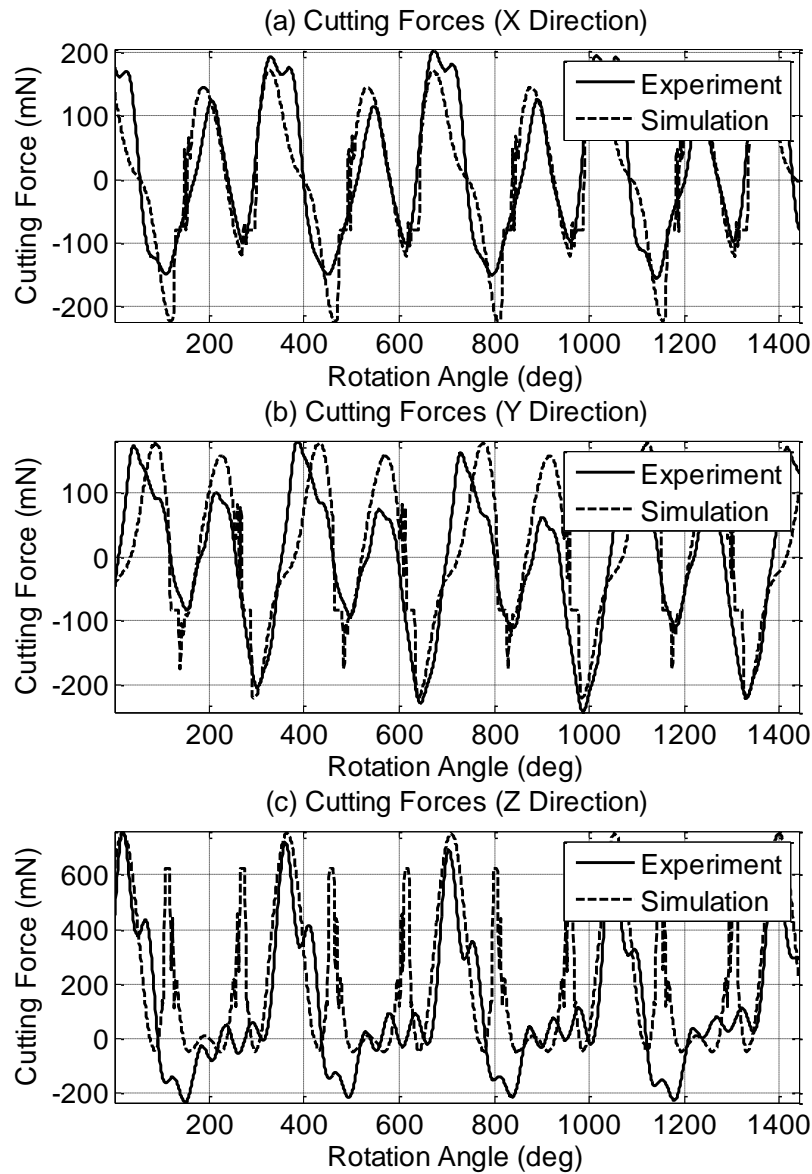
Figure 4.14: Comparison of experimental and simulated cutting forces (on 10 Vol.% Mg-MMCs)

Case III: spindle speed is 40,000 RPM, feed speed is 1.334 mm/s (f_t = 1.0 μm/t) and depth of cut is 10 μm using 100 μm diameter end mill.

Figure 4.15 shows the experimental and simulated cutting forces for 5, 10, and 15 Vol.% Mg-MMCs using cutting condition in Case III. In general, the simulated cutting force profiles do match major variations of the experimental data, and thus reveals the effect of the volume

fraction on the cutting force. It can be seen that all the cutting forces under the investigated cutting condition do not exhibit crisp force profiles for each tooth. As the volume fraction increases, more disturbances show up and the F_x profile displays more distinct trend to split into two teeth in a single revolution. This is mainly due to the low rigidity and small size of the 100 μm tool, so that the tool vibration/deflection plays more influential role in altering the force profile rather than the strengthening effect of nanoparticles. Furthermore, due to the small tool size, the increasing trend of the cutting force peak-to-peak value as volume fraction increases is not as obvious as that for 1 mm tool. This phenomenon is also related to nanoparticle size effect; therefore investigations are needed to clarify the root reason.
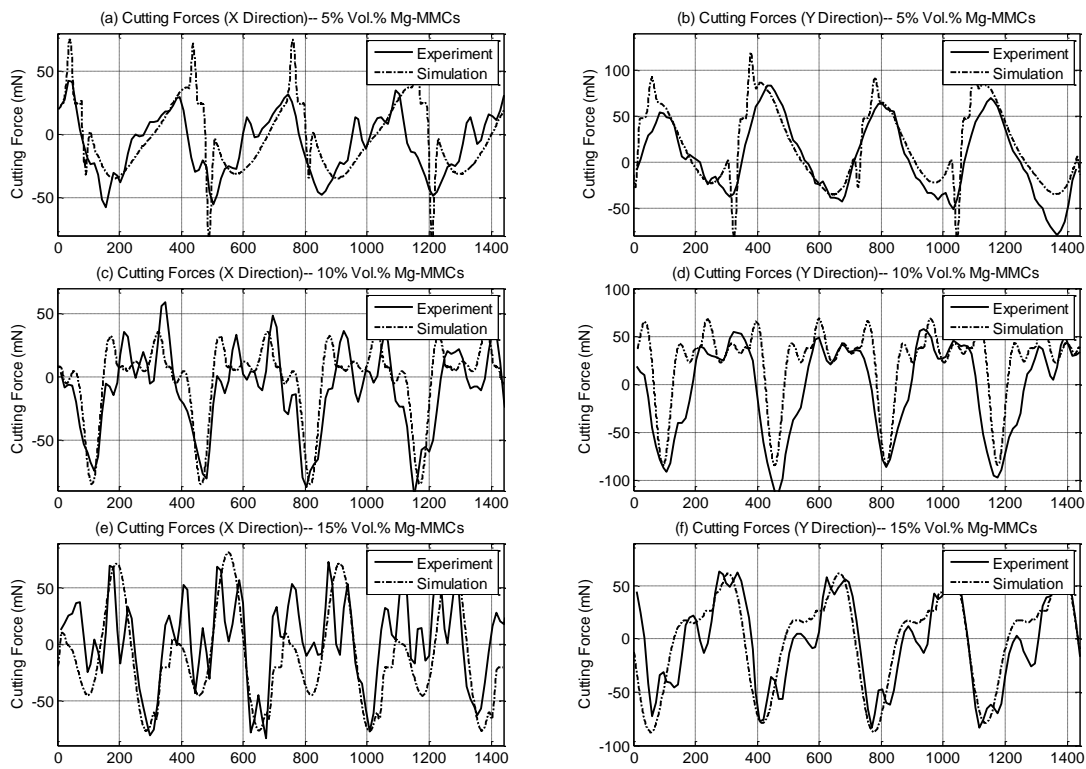
Figure 4.15: Comparison of experimental and simulated cutting forces with cutting condition ③ on Composite A: (a)~(b), Composite B: (c)~(d) and Composite C: (e)~(f)

In summary, the cutting force prediction is challenging for Mg-MMCs with nano-reinforcements in the micro milling process [62]. In the dynamic micro milling process, unexpected events occurred during the tool-workpiece interactions because of several dominant effects. These effects include the effect of nanoparticles (volume fraction and particle size), size effect, minimum chip thickness effect, effect of tool deflection and bottom of the flutes effect. In the proposed cutting force model, only the first three dominant effects are incorporated. Therefore, cutting force prediction errors are still observable and the max simulation error is relatively larger than the average one. The maximum and mean error values for some simulation studies are listed in Table 4.4. In order to predict cutting forces more accurately, the ignored effects in micro-cutting Mg-MMCs will be considered in future work.

Table 4.4: Simulation errors (%)

	F_x		F_y		F_z	
	Mean	Max	Mean	Max	Mean	Max
pure Mg (Case I cutting condition)	9.20	34.02	13.30	44.78	24.85	76.61
10 Vol.% Mg-MMCs (Case I cutting condition)	13.06	47.30	19.64	66.30	12.11	37.22
10 Vol.% Mg-MMCs (Case II cutting condition)	12.59	40.54	14.37	45.22	17.78	79.80

4.5 Summary

The main objective of this study is to construct a cutting force model to predict cutting forces when micro-mill nano-reinforced Magnesium metal matrix composites (Mg-MMCs) with high volume fractions. The nanoparticles reinforcement's effect is taken into consideration, as the particle size and volume fraction are incorporated explicitly in the cutting force model. The

material studied was Mg-MMC reinforced with SiC nanoparticles. To calibrate and validate the model, an experimental procedure was established and various cutting conditions were tested on pure Mg and Mg-MMCs with different volume fractions (0 Vol.%, 5 Vol.%, 10 Vol.% and 15 Vol.%). The comparison between the experimental and simulated cutting forces implies that the proposed model can effectively capture the major cutting force characteristics of nano-reinforced Mg-MMCs. The main results are concluded as follows:

1). Cutting force magnitudes greatly increase as the nanoparticles' volume fraction increases. This is attributed to the improved yield strength and fracture strength by adding SiC nanoparticles. The phenomenon is more obvious when using a larger diameter cutting tool.

2). Cutting force profiles of Mg-MMCs are not as smooth as those of pure Mg. The reason for that is the existence of ceramic nanoparticles influences the chip formation of Mg-MMCs. Mg-MMCs with different volume fractions of nanoparticles express different strengthened yield strengths and fracture strengths. Therefore, the cutting mechanisms and the SiC particles' behaviors in three cutting regimes are different. Consequently, cutting force profiles behave differently among pure Mg and Mg-MMCs with different volume fractions.

3). When using 100 μm cutting tools, all the cutting forces under the investigated cutting conditions on Mg-MMCs do not exhibit crisp force profiles for each tooth. As the volume fraction increases, more disturbances show up and the feed direction force displays more distinct trend to split into two teeth in a single revolution. Moreover, compared to 1 mm tool, the peak-to-peak cutting force increasing trend with the rising of volume fraction is not obvious. This is mainly due to the small size and low rigidity of the 100 μm tool. Consequently, the tool

vibration/deflection plays more influential role in altering cutting force profiles rather than the strengthening effect of nanoparticles.

The prediction inaccuracy of current model arises from the ignorance of tool vibration effect, tool wear effect, imperfection of the materials and bottom of the flutes effect. These effects will be further investigated and compensated in the future.

CHAPTER 5 EFFECTS OF FRACTURE MODELS ON CUTTING SIMULATION

In this chapter, a systematic evaluation of six ductile fracture models is conducted to identify the most suitable fracture criterion for metal cutting processes. Six fracture models are evaluated in this study, including constant fracture strain, Johnson-Cook, Johnson-Cook coupling criterion, Wilkins, modified Cockcroft-Latham, and Bao-Wierzbicki fracture criterion. By means of Abaqus built-in commands and a user material subroutine (VUMAT), these fracture models are implemented into a Finite Element (FE) model of orthogonal cutting processes in ABAQUS/Explicit platform. The local parameters (stress, strain, fracture factor, velocity fields) and global variables (chip morphology, cutting forces, temperature, shear angle, and machined surface integrity) are evaluated. The numerical simulation results are examined by comparing to experimental results of 2024-T3 aluminum alloy published in open literatures. Based on the results, it is found that damage evolution should be considered in cutting process FE simulation. Moreover, the B-W fracture model with consideration of rate dependency, temperature effect and damage evolution gives the best prediction of chip removal behavior of ductile metals.

5.1 Background Introduction

In the area of metal cutting simulation, there has been considerable amount of research dedicated to Finite Element Analysis (FEA) based numerical models due to their potential to provide predictions in various process variables such as stresses, strains and temperatures, as well as tool wear, tool breakage and machined surface integrity [81, 123, 124]. Most continuum-based FEA simulations depends on either Eulerian or Lagrangian formulations. Eulerian formulation can be used to model continuous chip formation at steady state [125, 126]. It requires fewer elements and thus computation load is relatively low. A chip separation criterion is not required in Eulerian based methods, but the shear angle needs to be determined experimentally prior to the simulation.

Two important factors in the FEA cutting simulations have been systematically studied by previous researchers, including the material constitutive model and the friction model. Shi and Liu [127] compared four different material constitutive models which incorporate strain rate and temperature effects. The material models applied in FEA modeling of orthogonal machining on HY-100 steel include Litonski-Batra [128, 129], power law [130], Johnson-Cook [131], and Bodner-Partom [132]. Results indicates that except the Litonski-Batra model, all other three models can give consistent predictions in cutting forces, chip thickness and shear angle with adequate accuracy. In the other aspect, friction modeling in the tool-workpiece interface has significant influence on the performance of FEA cutting simulation. Ozel [124] investigated several friction modeling techniques by developing constant and variable friction coefficient based models. It was found that the most accurate one for FEA simulation is the one with variable friction coefficient.

When pure Lagrangian formulation is applied without adequate remeshing, chip separation criterion cannot be avoided. Huang and Black [133] carefully examined different chip separation criteria, mainly including the criterion based on distance and the criterion based on stress. A combination of geometric and physical criteria was recommended. However, which fracture criterion is most suitable to simulate the chip separation process for ductile metal is still unknown. Zhang [134] conducted an evaluation on the reliability of the existing cutting chip separation criteria, including effective plastic strain, strain energy density, normal failure stress and distance between separation element node and tool tip. It was concluded that single quantity cannot be used reliably as a universal separation rule in metal cutting problems. Thus a more comprehensive and feasible criterion needs to be established in order to provide consistent and reliable FEA simulations for cutting processes.

In recent decades, several fracture models employed in pure Lagrangian-based FEA simulations were proposed for ductile metals. These models have been applied in various applications, including metal forming, high velocity impact, forging etc. In this chapter, six different fracture models are re-visited and re-evaluated specifically for metal cutting processes. These models include constant fracture strain, Johnson-Cook, Johnson-Cook coupling criterion, Wilkins, modified Cockcroft-Latham, and Bao-Wierzbicki fracture model. Teng and Wierzbicki [135] have evaluated some of them in a rigorous study for high velocity perforation simulation. The first objective of this research is to implement the above fracture models into ABAQUS/Explicit through a user material subroutine (VUMAT) and then further explore the influence of different fracture criteria on cutting performance. The second objective of this study

is to identify the most suitable ductile fracture model for metal cutting simulation based on FEA approach. The material properties of aluminum alloy A2024-T351 is used in the simulation.

5.2 FEA Formulation of Machining Process

In order to improve physical comprehension of the chip formation during cutting of ductile metals, a proper fracture criterion is needed. To focus on the physical inherence of the influence of the fracture models on cutting performance, a 2-D finite element model under plane strain deformation was used based on ABAQUS/Explicit platform. The radial cutting depth a_p is fixed at 4 mm. In the turning configuration, the feed rate (or the axial cutting depth) f is much lower than the radial cutting depth, as it is in the end milling process, where the feed speed (radial direction) is generally much lower than axial depth of cut, therefore plane strain assumption for building the model is reasonable for this study [123, 134].

Figure 5.1 shows a schematic representation of the constructed FEA model. It illustrates the geometries of the cutting tool and the workpiece. Quadrilateral continuum element CPE4RT was used for a coupled temperature-displacement dynamic analysis, so that the temperature distribution in the cutting process can also be obtained. The mesh size of the workpiece is 20 μm and the mesh size of the cutting tool is 50 μm without any remeshing rules assigned. In this way, the material elements' fracture evolution process can be observed in the FEA analysis, and the effects of different fracture models can be examined. Moreover, self-contact was not configured in the model due to the high computation cost, and only the contact between cutting tool and workpiece is assigned.

As shown in Figure 5.1, two different configurations were set up for this study:

a) The multi-part workpiece model is composed of three parts: Part 1 - the chip, Part 2 - the tool-tip passage zone, and Part 3 - the workpiece support. The assembly of the different parts in workpiece was achieved by setting a constraint type joining (Tie constraint).

b) The single-part workpiece model is composed of the tool part and the workpiece part.
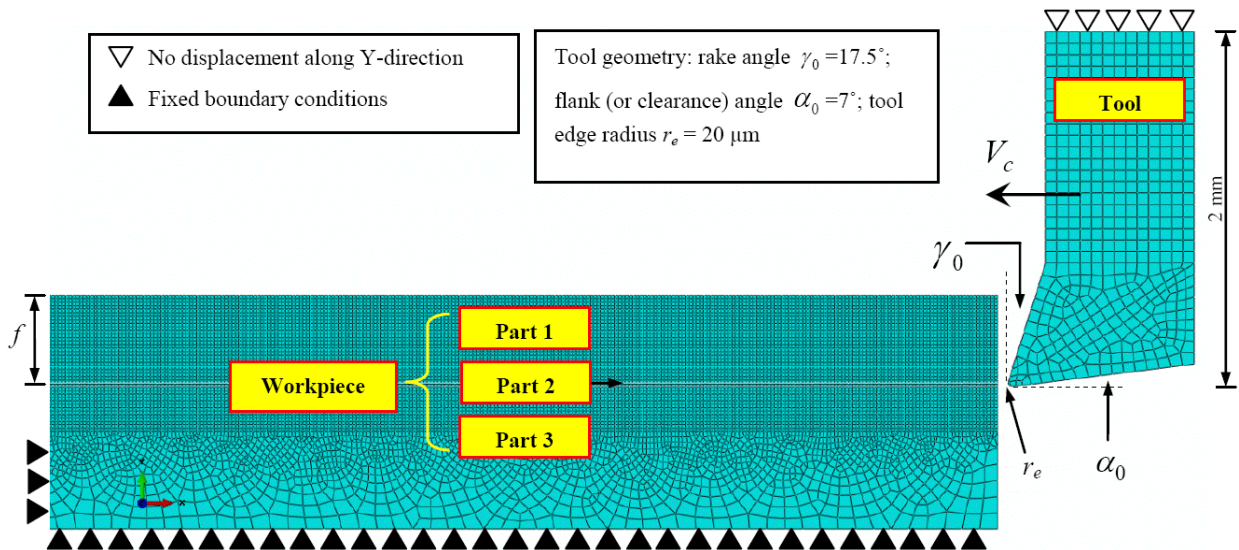
Figure 5.1: FEA model for the machining problem

The above two cutting assemblies were used to compare the various fracture criteria including the ones which require multi-part configuration.

Since the flow stress, namely instantaneous yield strength at which the material initiates plastic deformation is mostly affected by strain, strain rate and process temperature. Therefore, a widely accepted Johnson-Cook constitutive model [131], considering large deformation hardening, strain rate effect and temperature-dependence, is adopted in this study. The equivalent plastic flow stress is presented by:

106

$$\bar{\sigma} = [\mathrm{A} + B(\,\bar{\varepsilon}^{\,pl}\,)^n][1 + C\ln(\frac{\dot{\bar{\varepsilon}}^{\,pl}}{\dot{\varepsilon}_0})][1 - (\frac{T - T_{room}}{T_{melt} - T_{room}})^m] \tag{28}$$

where A, B and n are material constants for strain hardening; C is the material constant for strain-rate hardening; m is the material constant for thermal softening effect; T_{room} is the reference ambient temperature; T_{melt} is the melting temperature of the workpiece material and T is the current process temperature.

Based on the form of Equation (26), some modifications can be conducted for different materials in order to obtain a better data fitting. The Johnson-Cook parameters used in this study are listed in Table 5.1 and the physical properties of the workpiece and the cutting tools are summarized in Table 5.2. Reference strain rate $\dot{\varepsilon}_0$ is 0.000333 based on [135].

Table 5.1: Johnson-Cook parameter values for A2024-T351[135]

A	B	n	C	m
352	440	0.42	0.0083	1

Table 5.2: Physical properties of workpiece and cutting tool [123]

Physical parameter	Workpiece (A2024-T351)	Tool (Tungsten Carbide)
Density, ρ (kg/m^3)	2700	11900
Elastic modulus, E (GPa)	73	534
Poisson's ratio, v	0.33	0.22
Specific heat, C_p (J/kg$^\circ$C)	C_p=0.557T+877.6	400
Thermal conductivity, λ (W/m$^\circ$C)	$25 \leq T \leq 300$ λ =0.247T+114.4 $300 \leq T \leq T_{melt}$ λ =0.125T+226.0	50
Thermal expansion, α_d (μm.m/$^\circ$C)	α_d =8.9$\times$10^{-3}T+22.2	$\times$
T_{melt} ($^\circ$C)	520	$\times$
T_{room} ($^\circ$C)	25	25

For simplicity, the frictional interaction between the cutting tool and the workpiece was modeled according to References [136, 137]. Sticking and sliding friction conditions were applied between the tool and the workpiece material. Sticking friction occurs near the cutting edge contacting with the workpiece, and the frictional shear stress τ is equal to the average shear flow stress limit τ_{crit}. Meanwhile, sliding occurs far away from the contacting area, where the frictional shear stress is calculated by using friction coefficient μ. In this study, the friction coefficient is chosen to be 0.17 and τ_{crit} is set to be 161 MPa according to Reference [138].

$$\tau=\tau_{\text{crit}} \quad when \quad \mu\sigma > \tau_{\text{crit}} \quad (in \quad sticking \quad zone) \tag{29}$$

$$\tau=\mu\sigma \quad when \quad \mu\sigma < \tau_{\text{crit}} \quad (in \quad sliding \quad zone) \tag{30}$$

5.3 Fracture Model Formulation

5.3.1 Constant Fracture Strain

A constant effective plastic strain to fracture can be used to simulate the chip formation and provide cutting process variable values for reference. This approach assumes that there exists a critical equivalent plastic strain to failure $\bar{\varepsilon}_f^{pl}$. When the equivalent plastic strain reaches the value of the constant fracture strain threshold $\bar{\varepsilon}_f^{pl}$, the corresponding material element will be deleted. This method has been successfully implemented in modeling macro-sized orthogonal cutting processes of various soft and hard materials [139-141].

$$\bar{\varepsilon}^{\text{pl}} \geq \bar{\varepsilon}_f^{pl} \quad \text{(Material element removal criterion)}$$

(31)

Under the plane strain assumption, the equivalent plastic strain (marked as PEEQ in Abaqus) is defined as:

$$\bar{\varepsilon}^{\text{pl}} = \frac{1}{\sqrt{3}}\sqrt{2(\varepsilon_{p(11)}^2 + \varepsilon_{p(22)}^2) + \varepsilon_{p(12)}^2}$$

(32)

where $\varepsilon_{p(11)}$, $\varepsilon_{p(22)}$ and $\varepsilon_{p(12)}$ are the components of plastic strain in the 2-D plane strain coordinate system. In this study, different $\bar{\varepsilon}_f^{pl}$ values including 0.21, 0.3, 0.6, 0.9 were tested in the simulation. The range of the $\bar{\varepsilon}_f^{pl}$ values is determined according to Reference [135].

5.3.2 Johnson-Cook Fracture Criterion

Johnson-Cook (J-C) fracture model [142] incorporates strain hardening effect, strain rate effect and temperature dependency. It has been employed to simulate the chip separation behavior by many previous researchers [137]. The failure model is based on calculation of

damage parameter *D*, which is defined in Equation (31) and updated in every FEA solving step. Elements are assumed to fail and be deleted when the damage parameter exceeds unity.

$$D = \sum \frac{\Delta \bar{\varepsilon}^{pl}}{\bar{\varepsilon}_f^{pl}} \tag{33}$$

where $\Delta \bar{\varepsilon}^{pl}$ is the increment of the equivalent plastic strain, which is updated at every analysis step; $\bar{\varepsilon}_f^{pl}$ is the equivalent strain at failure and expressed in the following equation:

$$\bar{\varepsilon}_f^{pl} = (d_1 + d_2 e^{d_3 \eta})[1 + d_4 \ln(\frac{\bar{\dot{\varepsilon}}^{pl}}{\dot{\varepsilon}_0})][1 + d_5(\frac{T - T_{room}}{T_{melt} - T_{room}})] \tag{34}$$

where $d_1 \sim d_5$ are damage constants determined through experiments. Constants of J-C failure model for A2024-T351 are specified in Table 5.3. η is triaxiality (a dimensionless ratio of pressure versus Mises stress), which equals p/q (*p* is the pressure stress and *q* is the Mises stress). *p* and *q* are expressed as follows:

$$p = \frac{\sigma_1 + \sigma_2 + \sigma_3}{3}, \qquad q = \sqrt{\frac{1}{2}[(\sigma_1 - \sigma_2)^2 + (\sigma_3 - \sigma_2)^2 + (\sigma_1 - \sigma_3)^2]} \tag{35}$$

where σ_1, σ_2, and σ_3 are three principal stresses.

Table 5.3: Johnson-Cook failure constants [123]

d_1	d_2	d_3	d_4	d_5
0.13	0.13	-1.5	0.011	0

The Johnson-Cook fracture model has found numerous applications, including metal cutting problems, because of its simplicity of formulation, the ease of calibration and the wide availability of material constants for many ductile metals.

5.3.3 Johnson-Cook Coupling Fracture Criterion

In the coupling fracture criterion, chip formation process is assumed to undergo two steps before complete ductile failure. The first step considers damage initiation, while the second one considers damage evolution based on the fracture energy approach, proposed by Mabrouki, *et al.* [123]. By using this approach, damage accumulation is taken into account in the calculation of stresses and strains.

J-C failure model is used here as a damage initiation criterion, instead of as a failure criterion in a Pure J-C model. Namely, the damage in a given element is initiated when a scalar damage parameter (similar to D in Equation (31)) exceeds unity, based on a cumulative law. Point B in Figure 5.2 represents the damage initiation point after the strain hardening state (from Point A to Point B). Beyond point B, the load-carrying capability of the material elements is reduced until complete fracture. The complete fracture point happens at point D. The deformation during the phase (from Point B to Point D) is governed by the evolution law of the stiffness degradation.
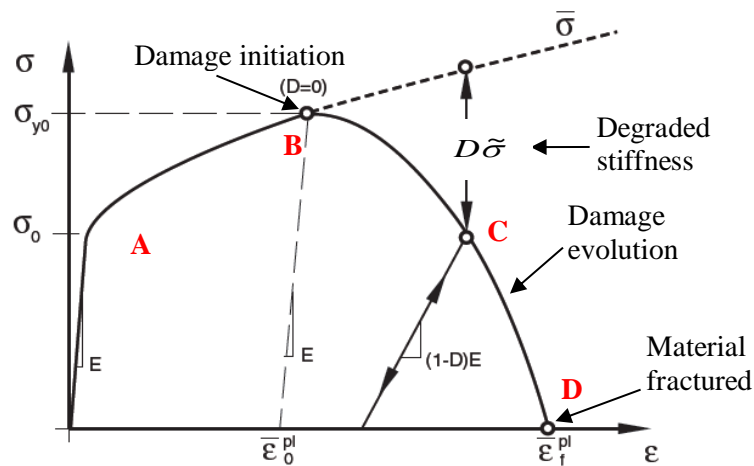
Figure 5.2: Stress-stain curve with progressive damage degradation [123]

Based on Hillerborg's fracture energy proposal [143], the energy G_f required to open a unit area of crack is defined as:

$$G_f = \int_{\bar{\varepsilon}_{0i}}^{\bar{\varepsilon}_f} L\bar{\sigma}_y d\bar{\varepsilon} = \int_0^{\bar{u}_f} \bar{\sigma}_y d\bar{u} \tag{36}$$

where L is the characteristic length of the element, $\bar{u}_f$ is defined as the equivalent plastic displacement as the fracture work conjugate of the yield stress after the onset of damage initiation.

In this approach, the softening response (phase B to D in Figure 5.2) after the damage onset point is characterized by a stress-displacement response. The expression introduces the equivalent plastic displacement $\bar{u}$ as the fracture work conjugate of the yield strength in the damage evolution stage. The length L is required and assumed to be the square root of the integration point element area in this study. Before the onset of damage, the equivalent plastic displacement is zero ($\bar{u}$ =0) as is the rate of this displacement ($\dot{\bar{u}}$ =0). Once a particular damage initiation criterion is satisfied, the materials stiffness and load-carrying ability decrease based on certain damage evolution laws. The equivalent plastic displacement is based on equation: $\dot{\bar{u}} = L\dot{\bar{\varepsilon}}$.

Two damage evolution laws based on energy dissipated during the damage process are given in Equation (36) and Equation (38). At any given time during the damage process, the equivalent plastic stress is given by:

$$\bar{\sigma} = (1-D)\tilde{\sigma} \tag{37}$$

A linear damage evolution law assumes a linear evolution of the damage variable with plastic displacement, which is described as:

$$D = \frac{L\bar{\varepsilon}}{\bar{u}_f} = \frac{\bar{u}}{\bar{u}_f} \tag{38}$$

where the equivalent plastic displacement at failure is:

$$\bar{u}_f = \frac{2G_f}{\sigma_y} \tag{39}$$

The exponential damage evolution rule is given by assuming an exponential evolution of the damage variable as:

$$D = 1 - \exp(-\int_0^{\bar{u}} \frac{\bar{\sigma}}{G_f} d\bar{u}) \tag{40}$$

In order to implement aforementioned damage initiation and evolution criterion, fracture toughness values K_C (shown in Table 5.4) are required to calculate the fracture energy G_f based on the following equation:

$$G_f = (\frac{1-\nu^2}{E})K_C^2 \tag{41}$$

Table 5.4: Fracture toughness properties of A2024-T351 [123]

ν	E	K_{IC}	K_{IIC}	K_{IIIC}
0.33	73	37	26	32

According to fundamentals of fracture mechanics, three fracture modes, including (I) opening mode, (II) sliding mode and (III) tearing mode, can be considered for cutting process simulation. However, in the plane strain cutting simulation, it is reasonable to assume that mode I and mode II are dominant and can exist individually or simultaneously. In this study, the fracture modes are considered in the material damage evolution in two ways: (1) with one fracture mode concerned for the entire workpiece and (2) with two different fracture modes concerned for Part 2 and Part 3, separately (Figure 5.1).

The advantages of this criterion are the load-carrying capacity of the partially damaged elements can be simulated more realistically. Fracture energy is considered besides the plastic work and friction work, which complies with Atkins's recommendations for cutting simulation [81, 144].

5.3.4 Wilkins Fracture Model

The Wilkins fracture model considers the effect of hydrostatic pressure p on damage accumulation in a different way from the Johnson-Cook model. An integral function of effective plastic strain weighted by two terms w_1 and w_2 is implemented [145, 146].

$$D = \int_0^{\bar{\varepsilon}_f} w_1 w_2 \mathrm{d}\bar{\varepsilon}_{pl} \quad in \quad R_{cr} \tag{42}$$

where D is the damage indicator. The magnitude of the critical volume R_{cr} is equal to the size of one element. The weighting terms w_1 and w_2 are defined as:

$$w_1 = (\frac{1}{1 + \alpha p})^{\gamma} \tag{43}$$

$$w_2 = (2 - A)^{\beta} \tag{44}$$

where α, γ and β are material constants. A is the ratio of deviatoric principal stresses defined as:

$$A = \max(\frac{s_2}{s_3}, \frac{s_2}{s_1}), \ s_3 \leq s_2 \leq s_1 \tag{45}$$

where s_1, s_2, and s_3 are the components of deviatoric principal stresses.

Fracture occurs when the damage parameter D reaches a critical value D_{cr}, which is considered as a material characteristic, independent of cutting conditions. An element is considered to fail if the following two conditions are satisfied:

$$\begin{cases} p < p_{cr} \\ \bar{\varepsilon}_{pl} > 0.0 \end{cases} \tag{46}$$

where p_{cr} is the critical hydrostatic tensile stress, given by

$$p_{cr} = -\frac{1}{\alpha} \tag{47}$$

The constants of Wilkins fracture model are given by [135]: D_{cr}=0.93, α=1.20×10^{-9} Pa^{-1}, β=2.18 and γ=2.15. Based on Equation (43), in this study, plane strain corresponds with A=0.

The Wilkins model has been applied in manufacturing and ballistics processes such as penetration and perforation [135] in which fracture occurs, however is not popular in metal cutting processes. When calibrated properly, the Wilkins fracture model is able to be implemented for metal cutting problems with appropriate damage evolution rules, so that a more comprehensive and realistic fracture criterion can be formed.

5.3.5 Modified Cockcroft-Latham Fracture Model

The original Cockcroft-Latham (C-L) fracture criterion and its various modifications have been applied in metal bulk forming processes [135, 147] and metal machining processes [148-150]. The damage is evaluated according to an integral of the normalized maximum principal stress σ_1 with respect to the effective plastic stress $\bar{\sigma}$:

$$D_{cr} = \int_0^{\bar{\varepsilon}_f} \frac{\langle \sigma_1 \rangle}{\bar{\sigma}} \mathrm{d}\bar{\varepsilon}_{pl} \tag{48}$$

where $\langle \sigma_1 \rangle$ is the Macaulay bracket, which drives the value of σ_1 to be unity if σ_1 >0, and zero if $\sigma_1 \leq 0$; $\bar{\sigma}$ is the equivalent stress. In this study, the critical damage value D_{cr} is selected from the range: 0.058 ~ 0.485, based on experimental results from the literature.

Further modification to the C-L fracture model can be carried out in order to optimize the fracture process simulation in cutting processes. For example, Ceretti *et al.* [150] used the C-L criterion combined with a criterion based on the effective stress and successfully predicted the serrated chip formation in the cutting simulation for AISI 1045 steel. Similarly, the C-L fracture model or its modified forms can be employed together with damage evolution for better cutting process prediction.

5.3.6 Empirical Bao-Wierzbicki Fracture Model

Bao and Wierzbicki [151, 152] proposed an empirical fracture model for ductile fracture based on stress triaxiality. Besides the strain intensity, the stress triaxiality is the most important factor that controls initiation of ductile fracture. They found that a ductile material would never fail if the stress triaxiality is less than -1/3. This property distinguishes the Bao-Wierzbicki (B-W) fracture model from other fracture models. They also found that the fracture locus would exhibit three branches in the whole range of stress triaxiality as a result of two failure mechanisms, including void growth and "shear decohesion" (as seen in Figure 5.3). The mathematical expressions of the three branches in the empirical B-W fracture model are given as:

$$\bar{\varepsilon}_{fh} = \begin{cases} 0.1225\left(\dfrac{\sigma_H}{\bar{\sigma}} + \dfrac{1}{3}\right)^{-0.46} & -\dfrac{1}{3} < \left(\dfrac{\sigma_H}{\bar{\sigma}}\right) \leq 0 \\[3mm] 1.9\left(\dfrac{\sigma_H}{\bar{\sigma}}\right)^{2} - 0.18\left(\dfrac{\sigma_H}{\bar{\sigma}}\right) + 0.21 & 0 < \left(\dfrac{\sigma_H}{\bar{\sigma}}\right) \leq 0.4 \\[3mm] 0.15\left(\dfrac{\sigma_H}{\bar{\sigma}}\right)^{-1} & 0.4 < \left(\dfrac{\sigma_H}{\bar{\sigma}}\right) \leq 0.95 \end{cases} \tag{49}$$
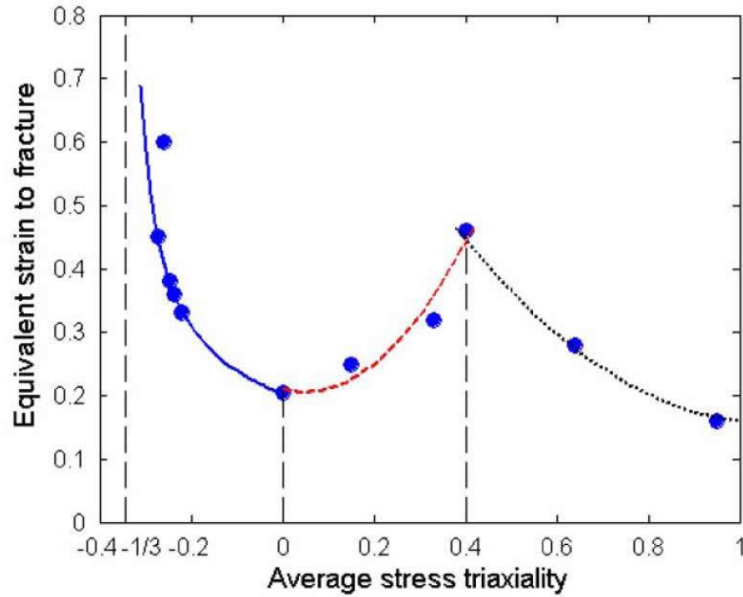
Figure 5.3: Fracture locus of empirical B-W model [151]

The B-W fracture locus provides a more comprehensive fracture reference for manufacturing processes under complex loading conditions, such as metal cutting processes. Therefore, this model is able to reflect the physical mechanism of material removal processes and produce reasonable cutting process predications. Moreover, due to the detailed calibration of triaxiality in a complete range, this rigorous fracture criterion's prediction capability is independent of the cutting conditions when the workpiece material is given.

However, during cutting process, strain-rate effect and temperature effect are also prominent under certain cutting conditions. Therefore, it is necessary to extend the empirical B-W model for various strain-rates and temperatures. An effective way is to couple the additional dependencies in the manner of J-C fracture model. The mathematical expression of the B-W model with rate and temperature effects is given as below.

$$\bar{\varepsilon}_f = \bar{\varepsilon}_{fh}[1 + d_4 \ln(\frac{\dot{\bar{\varepsilon}}^{pl}}{\dot{\varepsilon}_0})][1 + d_5(\frac{T - T_{room}}{T_{melt} - T_{room}})] \tag{50}$$

Further extension of the B-W fracture model is the modified Mohr-Coulomb criterion proposed by Bai and Wierzbicki [153] which will be evaluated in our future work.

Before fracture initiation, all the fracture models are assumed to be uncoupled from material constitutive model; thereafter, the calculation of flow stress and strain is separated from the checking of the fracture condition at each computational step. When the damage indicator reaches a critical value, an element either suddenly fails if damage evolution is ignored in the fracture criterion, or gradually loses its load-carrying capability subject to the progressive damage evolution laws until completely fails. Failed elements are removed to illustrate the chip separation in the cutting zone.

5.4 Cutting Conditions for Simulation Study

In our study, a number of cutting conditions are adopted in the FEA cutting simulation by using different fracture models as chip separation criteria. In order to verify the validity of the fracture models and suggest the most suitable one for metal cutting simulation, the acquired simulation results are compared with experimental results from open literature. Cutting conditions are designed as: cutting speed V_c = 200, 400, 800 m/min and feed rate f = 0.3, 0.4, 0.5 mm/rev. The radial cutting depth is fixed at 4 mm, and the thickness of 2-D plane-strain continuum elements in FEA cutting models is set as the same. Detailed parameter settings for each simulation test are shown in Table 5.5.

118

Table 5.5: Cutting condition settings of FEA simulation

Test #	Fracture criterion	Fracture parameter values	Cutting condition
1	Constant fracture strain	$\overline{\varepsilon}_f^{pl}$ =0.9	
2	Pure Johnson-Cook	See Table 5.3	
3	J-C with damage evolution (mode I)	G_f =16.711	Cutting speed: 800 m/min
4	J-C with damage evolution (mixed mode)	Fracture mode I & II	Feed rate: 0.3, 0.4 and 0.5 mm/rev
5	Wilkins fracture model	0.93, 1.2e-9, 2.15, 2.18	
6	Modified C-L model	D_{cr} =0.058 ~ 0.485	
7	Empirical B-W model	See Equation (47)	
8	B-W with rate and Temp	See Equation (48)	

5.5 Results and Discussion

In this section, eight groups of simulation are performed to evaluate different fracture models. The cutting conditions as well as the fracture model parameters are summarized Table 5.5. Four groups of simulation results are discussed in Section 5.5.1, emphasizing on the effect of damage evolution criterion. Another four groups of simulation are analyzed in Section 5.5.2, focusing on the influence of the B-W fracture criterion.

5.5.1 Effect of Damage Evolution Criterion

In this section, four aspects of cutting performance, including chip morphology, tool tip temperature, cutting forces and surface roughness of FEA cutting simulation, are evaluated for

different fracture models (constant fracture strain, Pure Johnson-Cook fracture model, J-C with mode I damage evolution and J-C with mixed mode damage evolution). The purpose of the analysis in this section is to reveal the effect of damage evolution and establish an efficient way to incorporate fracture energy in the progressive damage model. The overall comparison results are summarized in Table 5.6. The cutting condition used in these simulation tests is: cutting speed 800 m/min and feed rate 0.4 mm/rev. In Table 5.6, "P-P" represents peak-to-peak value of the measurement.

Table 5.6: Results comparison for fracture models in simulation Tests

	Item	Constant strain	Pure J-C	J-C with mode I	J-C with mixed	Results in [123]
workpiece	Chip thickness (μm)	223.6	0	584.1	618.01	~ 550
	Shear angle (˚)	33.95	0	44.4	42.9	~ 50 ˚
	Max Mises stress (MPa)	657	777.8	635.2	634.6	×
	Max pressure (MPa)	1658	100.3	949.7	1303	×
	Max temperature (K)	551.3	326.8	613.9	620.7	×
Tool	Max Mises stress (MPa)	1177	1746	1787	1650	1800
	Max pressure (MPa)	546.8	1060	982.3	870	×
	Max deflection (μm)	4.063	24.7	1.227	0.916	×
	Max temperature (K)	500.8	367.1	677.8	632.4	793
Process variables	RMS Fc (N)	647.47	833.3	840.27	820.93	834
	RMS Ft (N)	128.06	64.44	97.75	100.77	×
	P-P Fc (N)	932.42	3135	914.87	914.84	×
	P-P Ft (N)	336.28	641.15	142.89	152.4	×
	RMS Ra (μm)	0.781	1.1	0.51	0.473	×
	P-P Ra (μm)	3.21	6.78	0.458	1.37	5.5

J-C model combined with mixed damage evolution rules has been proved to be an effective way to simulate the material removal processes [123]. This method requires multiple part configurations. Moreover, it is required to preset a tool-tip passage zone and combine the mode I and II fracture energy into the damage evolution criterion. Results in Figure 5.4 show that FEA model with damage evolution can be simplified to use a single part and combine only mode I to represent the chip separation.

Figure 5.4 shows the chip morphology comparison using different fracture models in the cutting simulation. It shows the chip morphology and Mises stress distribution at cutting instant 200 μs during the simulation. Except for the pure Johnson Cook fracture model, other three models can deliver continuous chip formation. However, constant fracture strain model predicts thinner chip thickness and smaller shear angle comparing to results in Reference [123]. The reason is that in constant fracture strain model, the creation for deleting an element is the same for all the compression, tension, shear and other loading conditions. Due to this reason, the materials in the cutting zone which confront the cutting tool rake face can be unreasonably deleted. Therefore, the chip thickness is even thinner than the uncut depth of cut. In the other aspect, the materials' tension and shear thresholds are set higher than their actual capability. Without considering the rate dependency and temperature effect, the materials in the shear band and tool-workpiece contact surface are difficult to fail. That is the reason why continuous chips can form without segmentations and few elements are stretched in the back of the formed chips. The pure Johnson-Cook model utilizes the traditionally calibrated fracture model parameters, which neglects the "cut-off" value when triaxiality is less than -1/3. This leads the material to be

brittle even though the rate dependency is considered. Thus, the chip formation is not continuous and the shear band is not clear.
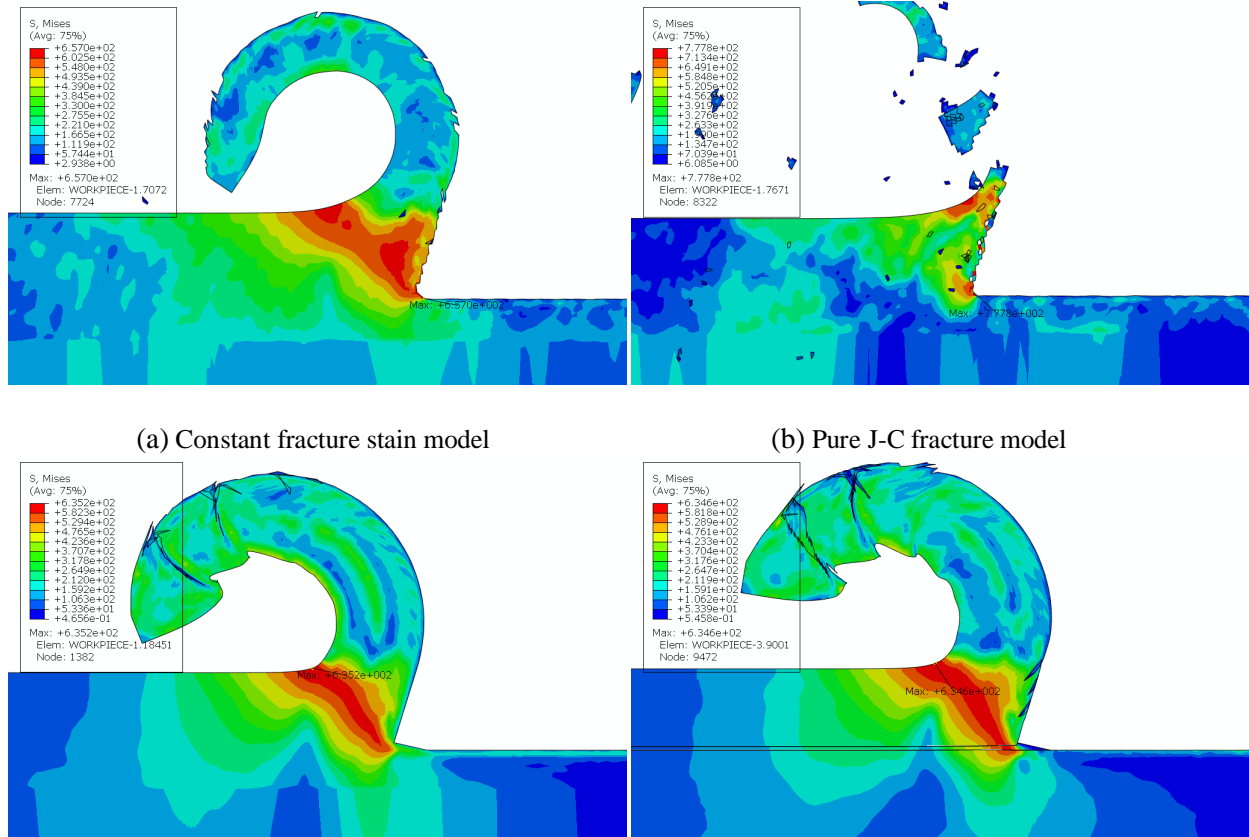
(a) Constant fracture stain model　　　　　　　(b) Pure J-C fracture model

(c) J-C with mode I damage evolution　　　　　(d) J-C with mixed damage evolution
Figure 5.4: Comparison of chip morphology using different fracture models

Figure 5.5 shows the nodal temperature distribution in formed cutting chips and Figure 5.6 indicates the nodal temperature distribution in the cutting tool. It can be seen that except the Pure J-C model, all other three fracture models can predict reasonable cutting temperature contours both in the workpiece and the cutting tool. However, the predicted maximum nodal temperature value and location vary for different fracture criteria. J-C with damage evolution models give very similar temperature distributions, while the constant fracture strain model

results in a much lower predication than the actual temperature value. The reason is because the over-deleted elements, using constant fracture strain model, take away much dissipated energy, which could have resulted in higher heat generation. The unrealistic low temperature value from Pure J-C model is similar because of this reason.
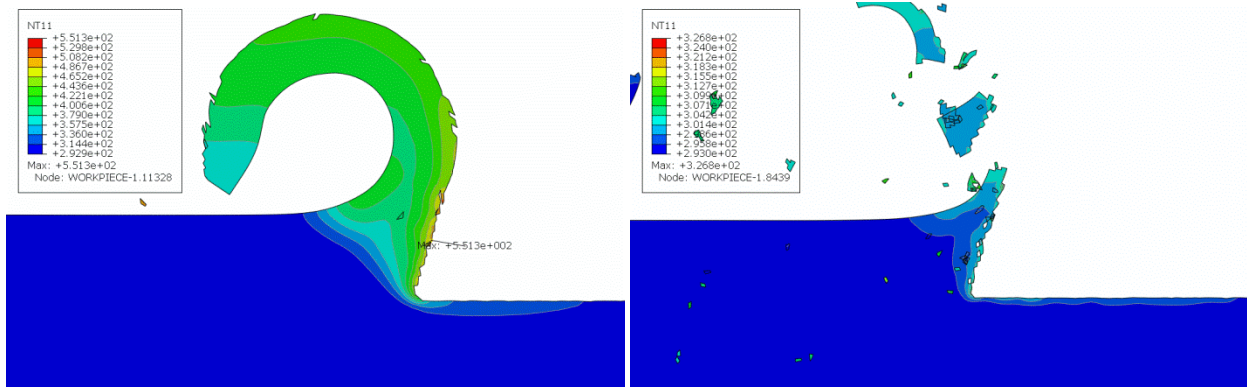
(a) Constant fracture stain model

(b) Pure J-C fracture model
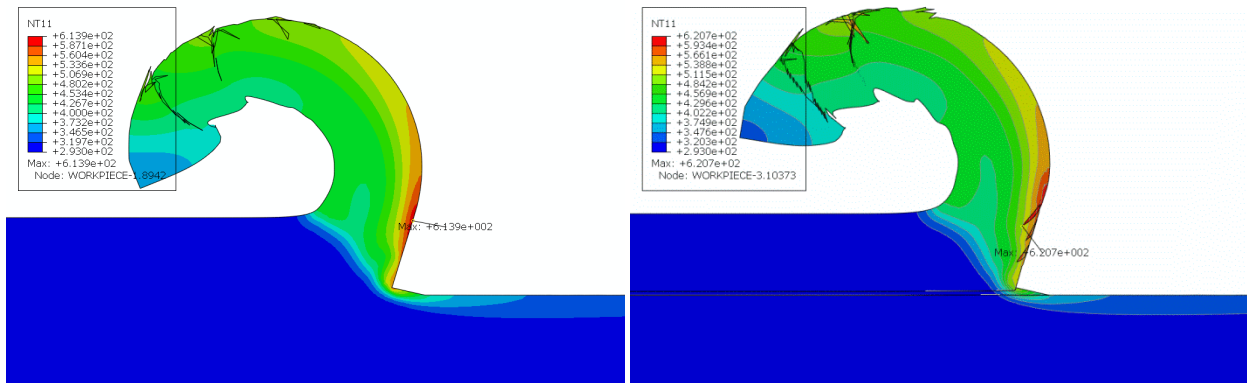
(c) J-C with mode I damage evolution

(d) J-C with mixed damage evolution

Figure 5.5: Comparison of chip temperature using different fracture models

(a) Constant fracture stain model   (b) Pure J-C fracture model

(c) J-C with mode I damage evolution   (d) J-C with mixed damage evolution
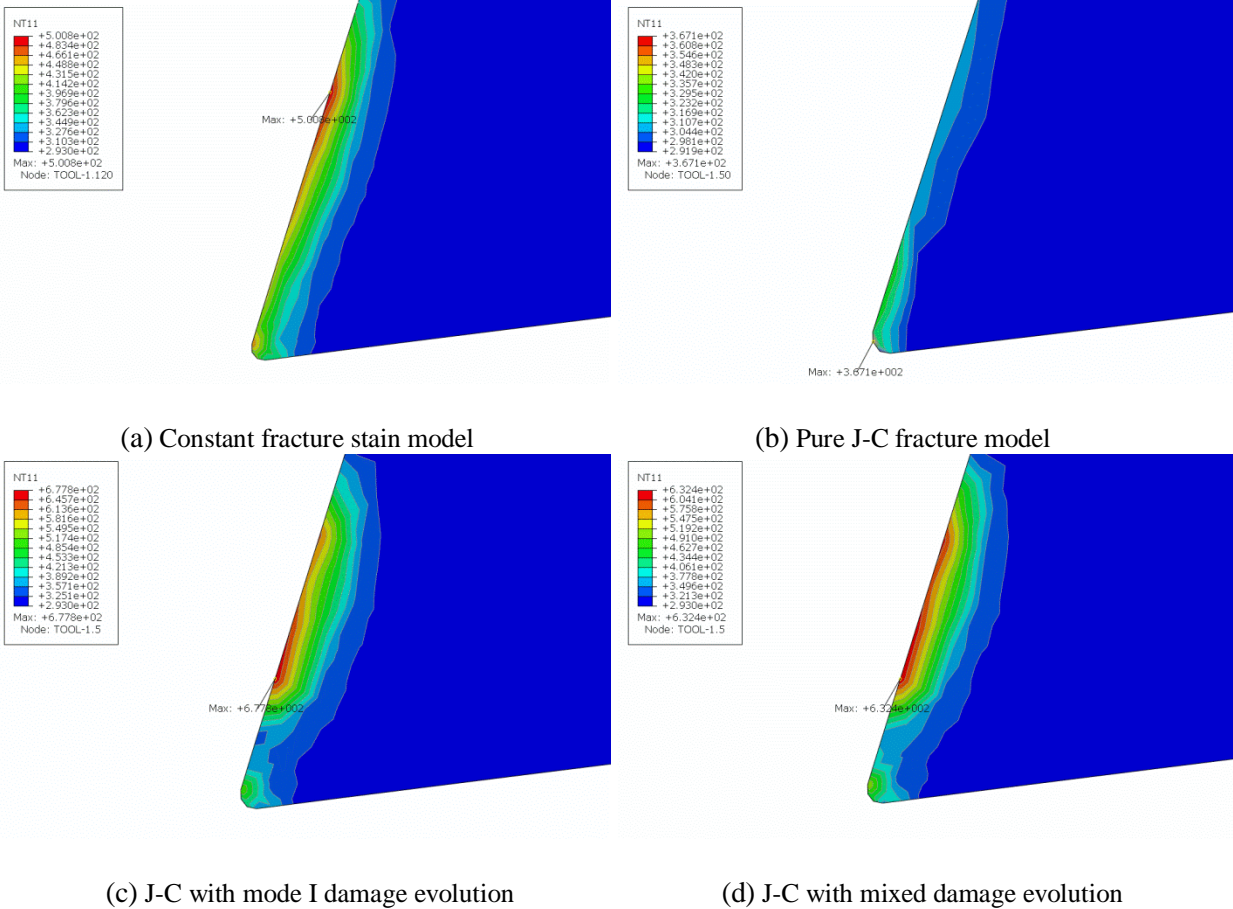
Figure 5.6: Comparison of tool rake face temperature using different fracture models

Figure 5.7 shows the element temperature distributions along the cutting tool rake face starting from the tool tip. Comparing with temperature distribution patterns in [154], it can be seen that the J-C model with damage evolution is better than the other two models in predicting cutting temperatures. The reason why J-C with mode I damage evolution has higher temperature profile than J-C with mixed damage evolution model is because mode I critical fracture value is higher than the other two modes (shown in Table 5.4) for A2024-T351. The dissipated energy within the workpiece material for J-C with mode I fracture model is higher; therefore, the

transferred heat due to plasticity and friction in this model is higher, which leads to higher temperature profile.
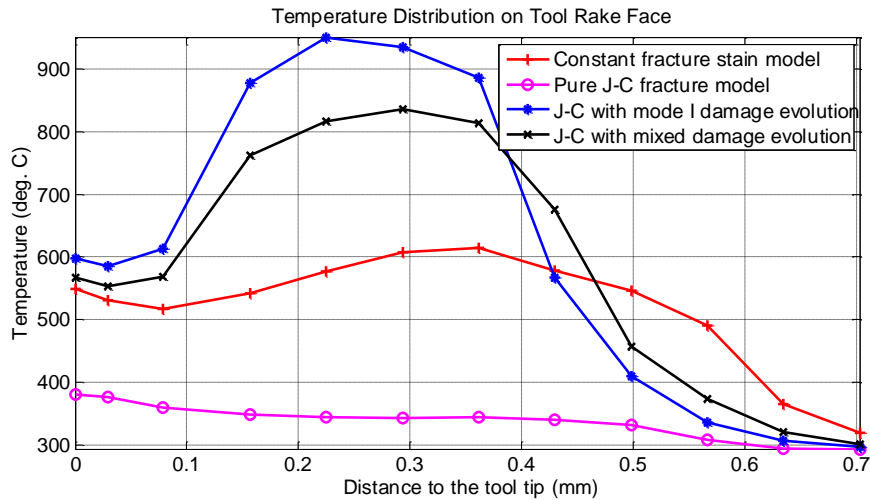
Figure 5.7: Comparison of temperature distribution on tool rake face using different fracture model

The cutting force responses from different fracture models are shown in Figure 5.8. Constant fracture strain model produces lower average cutting force with large fluctuations, comparing to the actual cutting force value from literature. Pure J-C gives much more unrealistic force profile -- at the beginning of the cutting simulation, the cutting force peak value exceeds ten times of the actual force amplitude. This is probably due to the computational noise coming from frequent element deletion by using Pure J-C model. J-C fracture model with damage evolution gives accurate cutting force prediction. Actually, J-C model with mode I damage evolution is good enough for predicting accurate cutting forces.
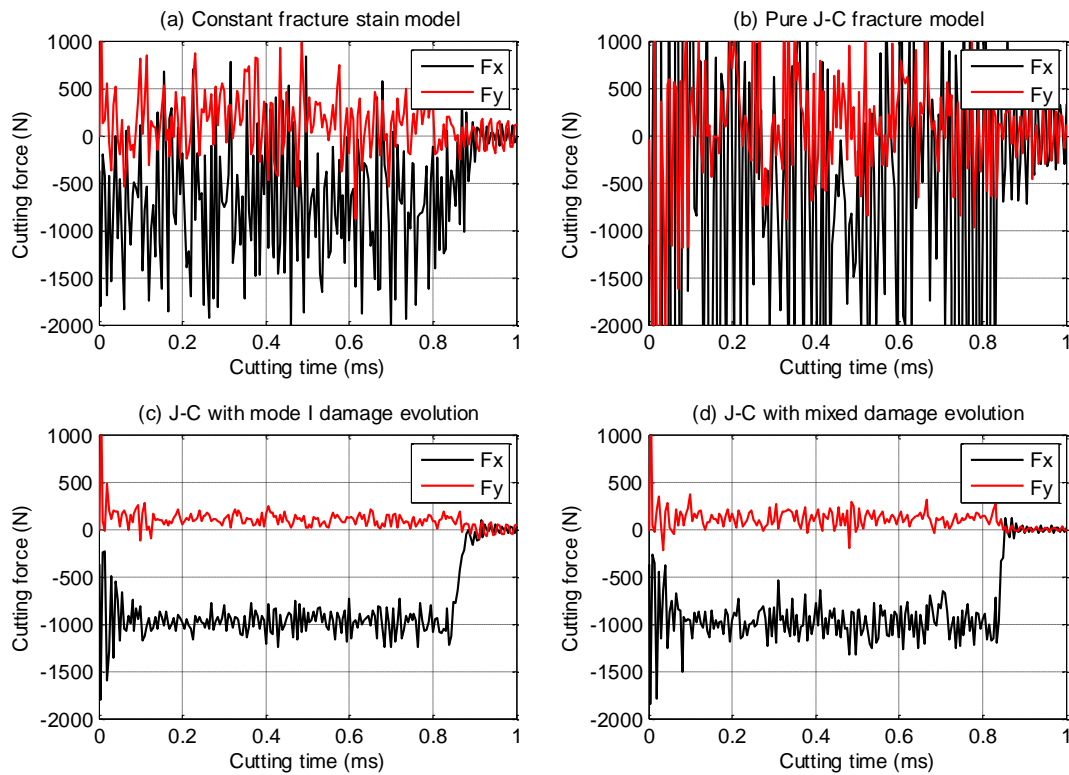
Figure 5.8: Comparison of cutting forces using different fracture models

Figure 5.9 shows the machined surface profile using different material fracture models. Although surface roughness is difficult to predict, the advantage of using damage evolution in the fracture model can be restated by observing the roughness results. According to the variation of materials' load-carrying capability during cutting process (illustrated in Figure 5.2), without using damage evolution, the elements are deleted immediately once damage criterion is met. This results in abrupt change in cutting energy and thus aggravates the vibration of the cutting tool tip. Therefore, surface profile with large fluctuation above and beneath zero line is generated. On the other hand, damage evolution enables the materials retain certain load-carrying capability

so that "elastic recovery" [43, 90] can be modeled in the cutting simulation since most of the

nodal displacement values are larger than zero.
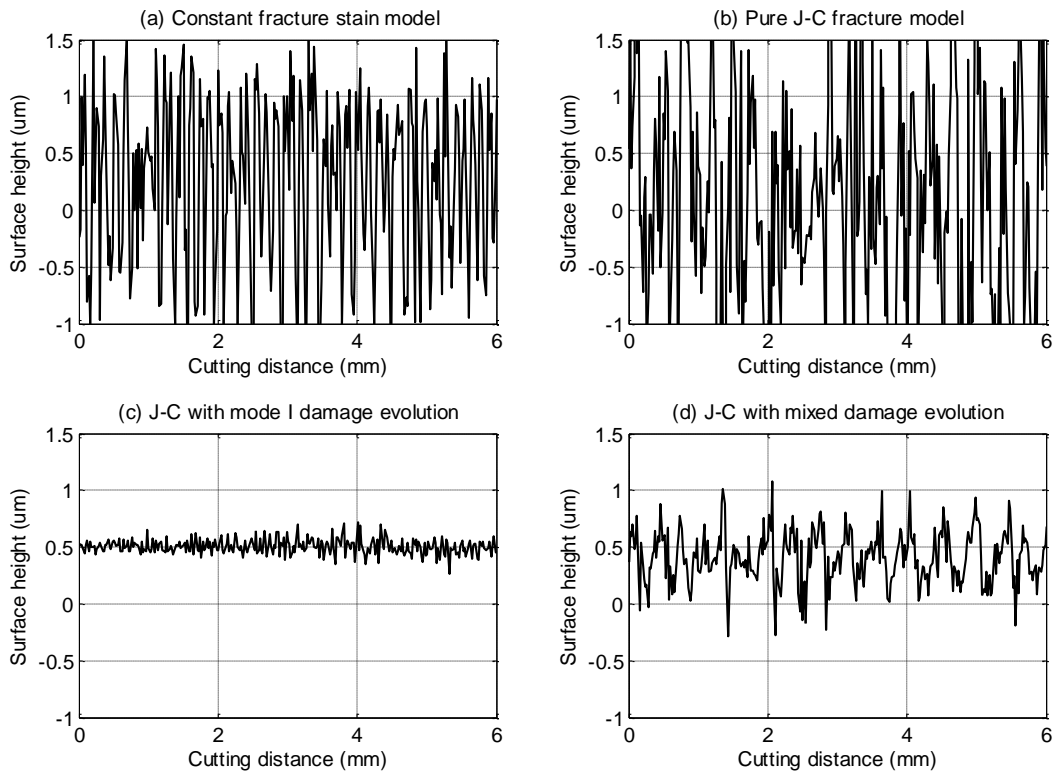
Figure 5.9: Comparison of surface profiles using different fracture models

In all, the fracture model with damage evolution has better performance than the ones

without damage evolution. It is recommended that damage evolution should be incorporated in

FEA cutting simulations if possible. Otherwise, certain amount of energy will be lost and

prediction results may have more discrepancies. This matches the same results as stated by

Atkins [81], who proposed that the fracture energy should be considered, which is related to new

surface generation energy.

5.5.2 Effect of B-W Fracture Criterion

In this section, different aspects of cutting performance of FEA cutting simulation are evaluated for different fracture models including Wilkins, modified Cockcroft Latham, empirical B-W, and B-W with rate and temperature effects. The purpose of the analysis in this section is to establish the effect of B-W fracture model and extend the fracture criterion to achieve better result in cutting simulation. Simulation results of the fracture models are summarized in Table 5.7. The cutting condition used in these simulation tests is: cutting speed 800 m/min and feed rate 0.4 mm/rev. In Table 5.7, "P-P" represents peak-to-peak value of the measurement.

Figure 5.10 shows the chip morphology and von Mises stress distribution of the four different fracture models in Table 5.7. Wilkins fracture model results in intermittent chips, whose thickness is smaller than the uncut chip thickness. Shear angle from this model is smaller than the literature result. The chips exhibit consistent trapezoidal shapes during the entire cutting simulation. Meanwhile, Modified C-L model shows similar intermittent chip shapes, and the shear angle is even smaller than the result of Wilkins model. Saw-tooth like discontinuous cutting chips are observed. However, the volume of each separated chip is smaller than that of the Wilkins model. It is difficult to establish the critical damage threshold for modified C-L model.

Table 5.7: Results comparison summary for fracture models in simulation Tests

Item		Wilkins model	Modified C-L model	Empirical B-W model	B-W with rate and Temp	Results in [123]
workpiece	Chip thickness (μm)	350.3	0	0	520.5	~ 550
	Shear angle (°)	42.1	41.9	45.6	47.5	~ 50
	Max Mises stress (MPa)	617.4	616.8	617.5	620.8	×
	Max pressure (MPa)	1068	671.0	1363	1886	×
	Max temperature (K)	537.4	742.3	718.4	774.5	×
Tool	Max Mises stress (MPa)	1345	1872	3116	1821.0	1800
	Max pressure (MPa)	584.3	1073	1549	1210	×
	Max deflection (μm)	5.707	1.348	1.956	1.718	×
	Max temperature (K)	515.9	705.6	547.1	797.8	793
Process values	RMS Fc (N)	1002.78	812.58	576.17	826.28	834
	RMS Ft (N)	273.97	160.22	153.67	148.19	×
	P-P Fc (N)	3733.04	1228.36	1800.84	988.21	×
	P-P Ft (N)	1393.35	679.0	860.80	771.61	×
	RMS Ra (μm)	1.11	1.66	1.92	2.52	×
	P-P Ra (μm)	4.33	6.49	13.2	11.4	5.5

The empirical B-W model gives intermittent chips as well, which have consistent trapezoidal shapes during the simulation. The thickness of each trapezoidal chip is determined by cutting conditions. When embedding rate dependency and temperature effect into the empirical

B-W model, the cutting chips become saw-tooth like and present more realistic chip shape predictions. Shear angle prediction from this fracture model is the most accurate among the simulation tests. Overall, B-W fracture criterion with rate and temperature effects has the most comprehensive representations of the material's fracture characteristics in terms of different loading modes, loading directions, strain rate and processing temperature. This is the reason why its chip morphology has the closest shape as saw-tooth like as in Mabrouki's work [123].
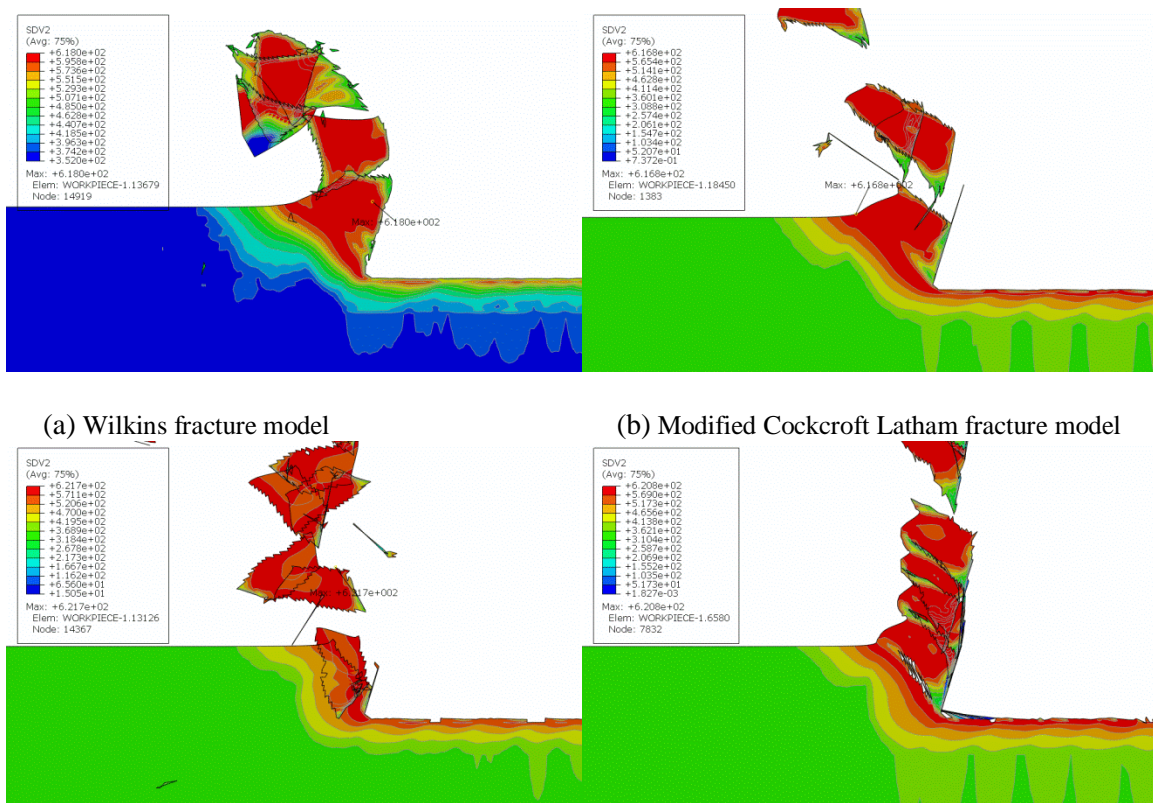
(a) Wilkins fracture model   (b) Modified Cockcroft Latham fracture model

(c) Empirical B-W fracture model   (d) B-W with rate and temperature effects
Figure 5.10: Comparison of Von Mises Stress using different fracture models

State Dependent Variable (SDV) 4 in the Fortran material subroutine saves the temperature distribution induced by plastic deformation (Figure 5.11). In the continuously formed cutting chips from B-W with rate and temperature model, the shear band has higher

temperature, while the islands between shear bands have lower temperature. This phenomenon also can be observed in the empirical B-W model and the modified C-L model, even though the chips are discontinuous. However, since Wilkins fracture model does not directly include the effect of triaxiality (the mean pressure is used instead), the shear bands are not distinct in the cutting simulation. That is the reason why the temperature distribution in the workpiece is lower and more uniform than the other three models. Therefore, it can be concluded that the way how the triaxiality is considered in the fracture model has significant influence on the temperature distribution predictions.
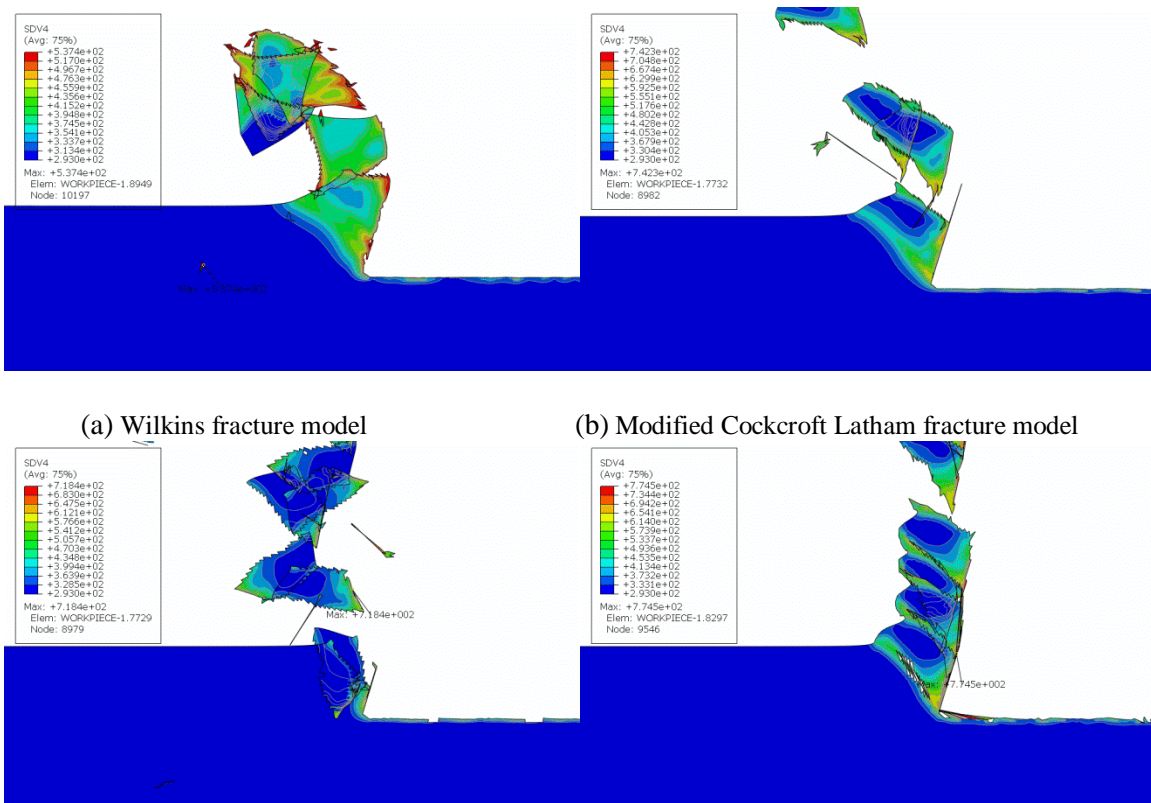
(a) Wilkins fracture model   (b) Modified Cockcroft Latham fracture model

(c) Empirical B-W fracture model   (d) B-W with rate and temperature effects

Figure 5.11: Comparison of plastic temperature using different fracture models

It can be seen in Figure 5.12 that all the four models cannot predict cutting tool temperature distribution accurately at the selected cutting instant. As the cutting process proceeds, the Wilkins fracture model delivers similar temperature pattern as J-C with damage evolution model. Empirical B-W model and B-W model with rate/temperature effects model cannot deliver correct temperature patterns mainly because the formed cutting chips cannot stay in contact with the tool rake face for adequate length of time. As for empirical B-W model, the energy in the intermittent chips dissipates after chips depart from the shear band. Besides, due to the ignorance of the contact among the formed cutting chips, the back of the cutting chips do not have full contact with the tool rake face. Therefore, the contact definition has certain influence on the cutting tool temperature predictions, and it could be further improved to acquire more realistic temperature predictions. Note that damage evolution has not been applied in the B-W model, which could be a potential reason.

(a) Wilkins fracture model   (b) Modified Cockcroft Latham fracture model

(c) Empirical B-W fracture model   (d) B-W with rate and temperature effects

Figure 5.12: Comparison of tool tip temperature using different fracture models
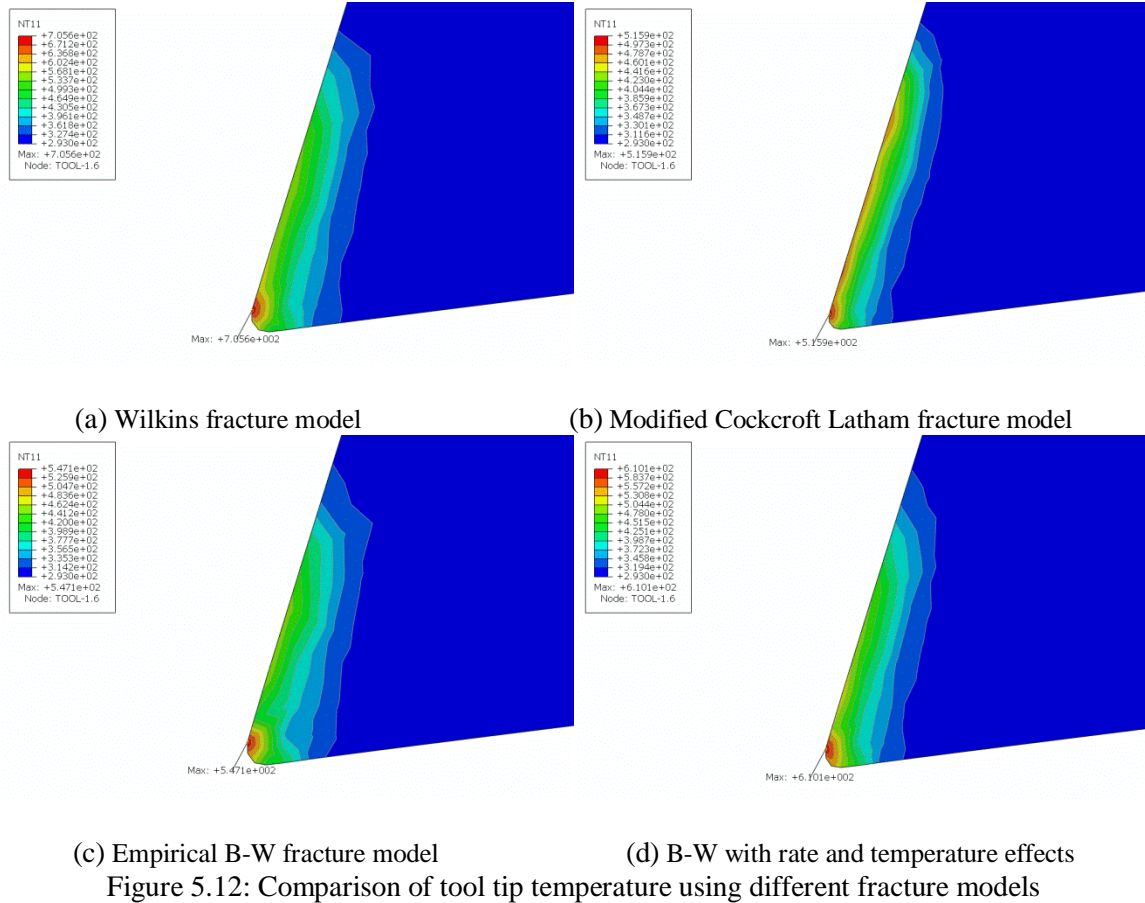
Figure 5.13 shows the temperature profile along the cutting tool rake face starting from the tool tip. All the four fracture models have a maximum temperature point near the tool tip. The further from the tool tip, the lower the temperature. This is probably due to the intermittent cutting chips do not have enough interaction with the tool rake face, so that the cutting heat has not accumulated as much as in the simulation tests of section 5.5.1. The Wilkins model has larger intermittent chips so that the high temperature range (> 450 K) is larger than the other three models.
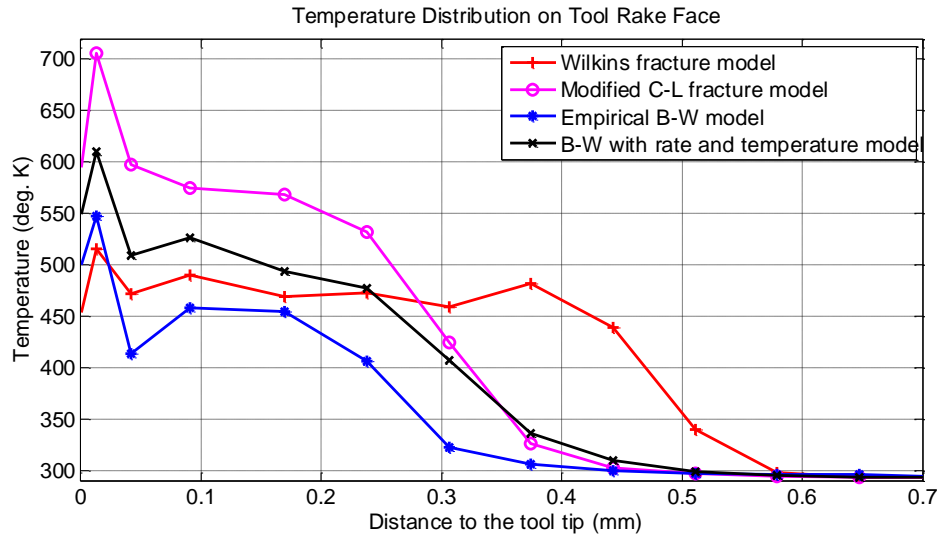
Figure 5.13: Temperature distributions on the tool rake face for different fracture models

Figure 5.14 illustrates the cutting force evolution during the cutting simulation. Wilkins fracture model has unreasonable large fluctuations, even though the average force value is close to the experimental one. Large tool deflection is observed when using Wilkins model, which may be the cause of large force fluctuation. Both modified C-L model and B-W with rate/temperature effects model give proper force predictions, while the latter's result is more accurate. Due to the ignorance of the rate and temperature effects, the empirical B-W model gives inaccurate average force values as well as unreasonable peak-to-peak force values.
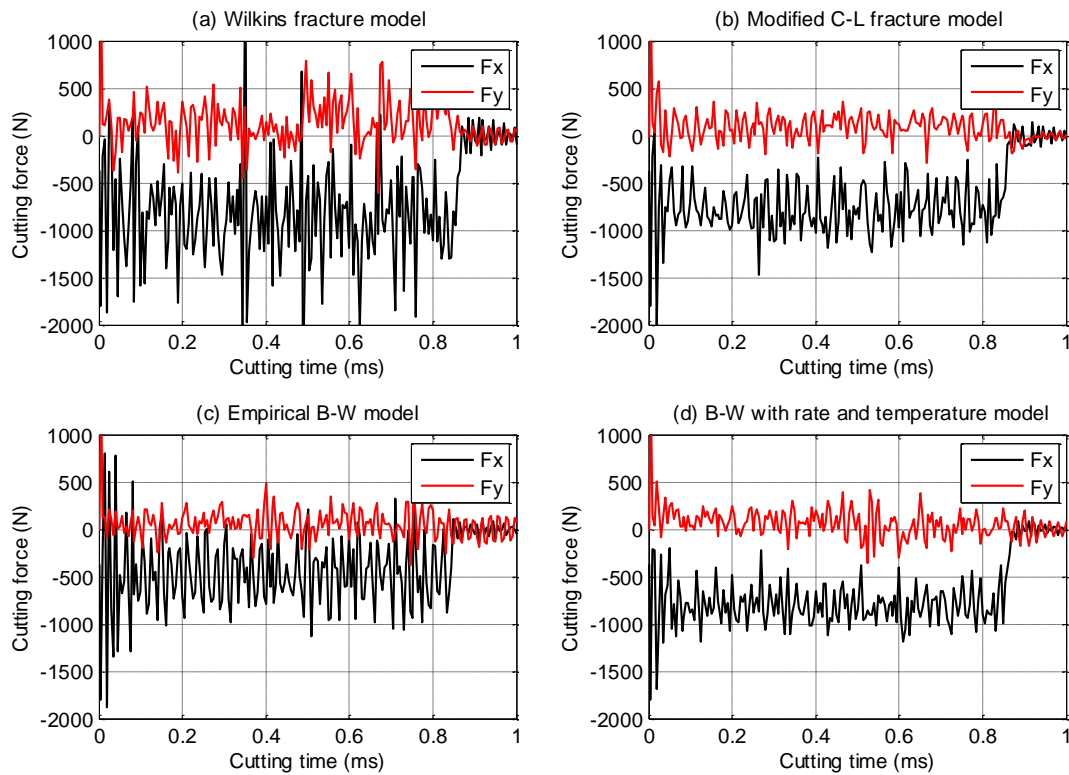
Figure 5.14: Cutting force comparison for different fracture models

Machined surface profiles are summarized in Figure 5.15. It can be seen that Wilkins fracture model has the smoothest surface. Modified C-L and B-W with rate/temperature have surface roughness R_a prediction values close to the literature reference results. However, R_a values of both models are larger than the reference data. The reason is because the damage evolution algorithm is not considered in the fracture models, which generates a rougher machined surface than the fracture models with damage evolution.
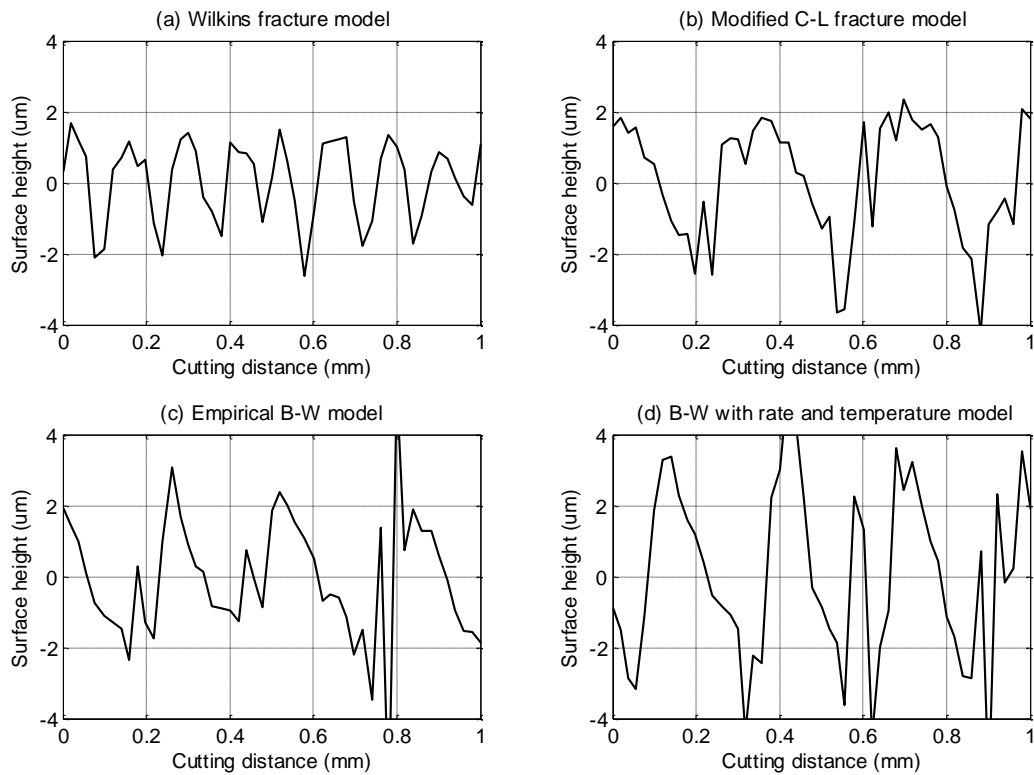
Figure 5.15: Surface profile comparison for different fracture models

Figure 5.16 illustrates the damage factor distributions. Wilkins fracture model has a wide shear band and the intermittent cutting chips are sheared off from there. The Modified C-L model and the B-W with rate/temperature model demonstrate single crack initiation in the middle of the shear band. Comparing to the experimental chip formation in Figure 5.17, it can be concluded that the B-W with rate/temperature fracture criterion has the best capability to predict the chip morphology.

<div style="text-align:center">(a) Wilkins fracture model   (b) Modified Cockcroft Latham fracture model</div>

<div style="text-align:center">(c) Empirical B-W fracture model   (d) B-W with rate and temperature effects</div>

Figure 5.16: Comparison of damage factor values using different fracture models

<div style="text-align:center">(a)   (b)</div>
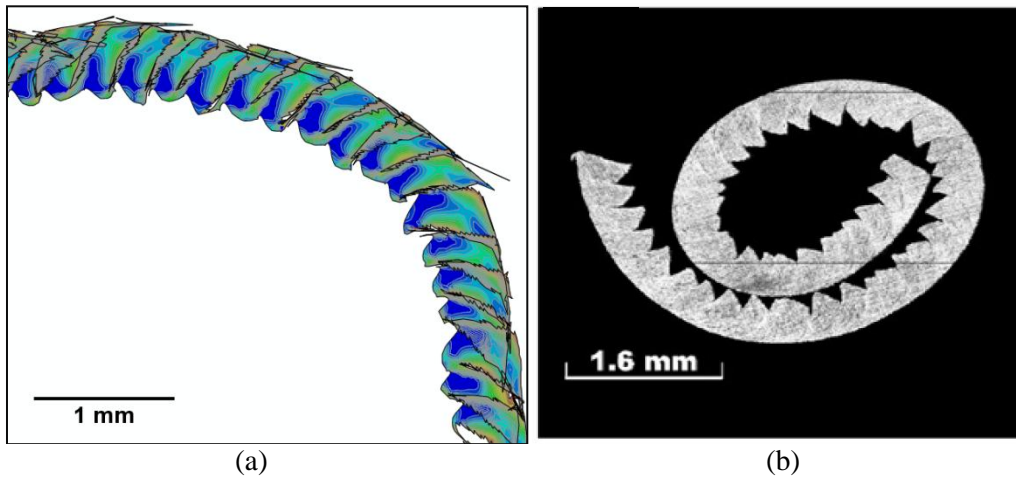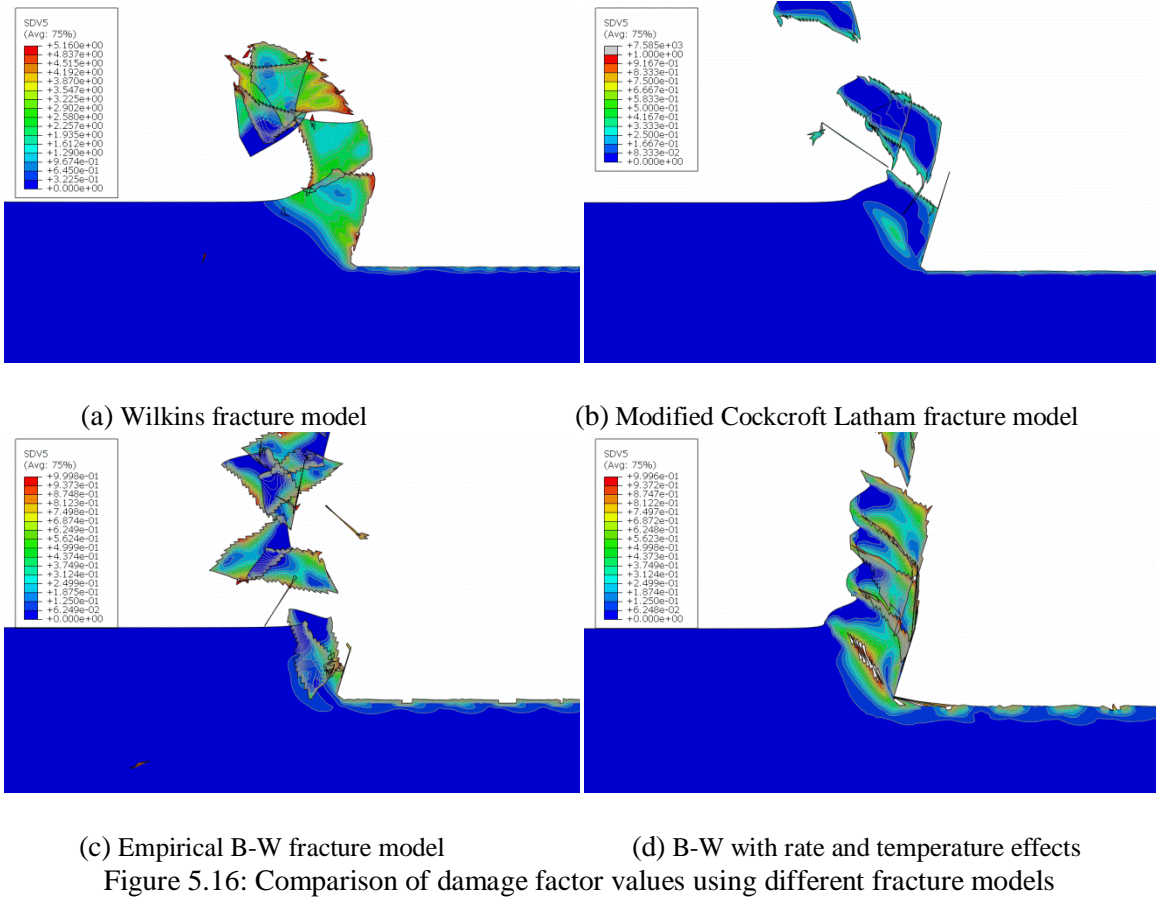
Figure 5.17: Comparison of (a) simulated chip formation of BWRT model and (b) real chip formation from literature [123]

5.6 Summary

The advantages and disadvantages of six ductile fracture models in predicting cutting performance have been compared and analyzed. Results can be summarized as below:

1). The constant fracture strain model fails to provide accurate chip morphology prediction in a wide range of failure strains. The Wilkins fracture model also cannot provide accurate continuous chip formation prediction. The experimental shear angle, cutting temperature, cutting force and surface roughness values are not satisfied from these two fracture criteria.

2). The Johnson-Cook fracture model and the empirical Bao-Wierzbicki fracture model formulated in the space of stress triaxiality and equivalent fracture strain are capable of predicting realistic stress/strain/temperature distributions, cutting forces and surface roughness. However, pure J-C model is not sufficient to predict chip formation and cutting forces, due to the ignorance of the "cut-off" value for ductile metal when triaxiality is less than -1/3 (chip formation becomes more intermittent and cutting force has excessive fluctuations).

3). By coupling with material damage evolution and its fracture energy, the capability of Johnson-Cook and Bao-Wierzbicki can be further extended to predict accurate chip morphology. The fracture model with damage evolution has better performance than those without damage evolution. It is recommended to consider damage evolution in FEA cutting simulations. Otherwise, certain amount of energy will be lost and prediction results will be adversely affected.

4). The B-W fracture model with consideration of rate dependency, temperature effect and damage evolution is the most comprehensive model to describe the chip removal behavior of ductile materials. The only drawback is that this comprehensive fracture criterion requires

numerous fracture parameters, some of which are difficult to be obtained from experiments directly.

Material fracture data and machining testing results of 2024-T351 aluminum alloy from open literatures are used in this study. The results provide valuable reference for selecting fracture models in the FEA cutting simulation study on engineering materials.

CHAPTER 6   NUMERICAL MODELING OF MICRO-CUTTING

MG-MMCS

In this chapter, micro-cutting performance of MMCs materials is investigated through simulation studies. Finite Element Analysis (FEA) method is used to predict cutting responses. Firstly, homogenized material properties are employed in FEA cutting models to evaluate the effect of volume fraction by considering calibrated plasticity and fracture curves. A set of materials' properties of Mg-MMCs from the literature are used in the cutting simulation. Secondly, actual microstructures of the two-phase material are modeled in the FEA cutting models by considering uniformly dispersed particles. The interface between the matrix material and the reinforcement material are modeled by using shared nodes method. Micro-sized SiC particles and nano-sized SiC particles are modeled into the matrix material and cutting performance is studied. The effects of reinforcement ceramic particles on micro-cutting performance are carefully evaluated.

6.1 Micro-cutting Homogenized Nano-MMCs

In this section, Magnesium Metal Matrix Composites (Mg-MMCs) reinforced with SiC nanoparticles is evaluated in the simulation case study. Different reinforcement volume fraction results in different mechanical properties of the material and thus affects the micro-cutting

performance. A FEA micro-cutting model is set up and used to study the effect of volume fracture on micro-cutting responses, mainly in terms of cutting forces, chip formation and surface roughness. Homogenized mechanical properties are adapted in this section.

6.1.1 FEA Cutting Model Setup

As shown in Figure 6.1, in this cutting model, the cutting tool is modeled as a rigid body and the workpiece is modeled as a deformable elastic-plastic component with fracture properties. 2-D plain strain condition is assumed and CPE4RT element is employed with initial minimum meshing size of 2 μm.
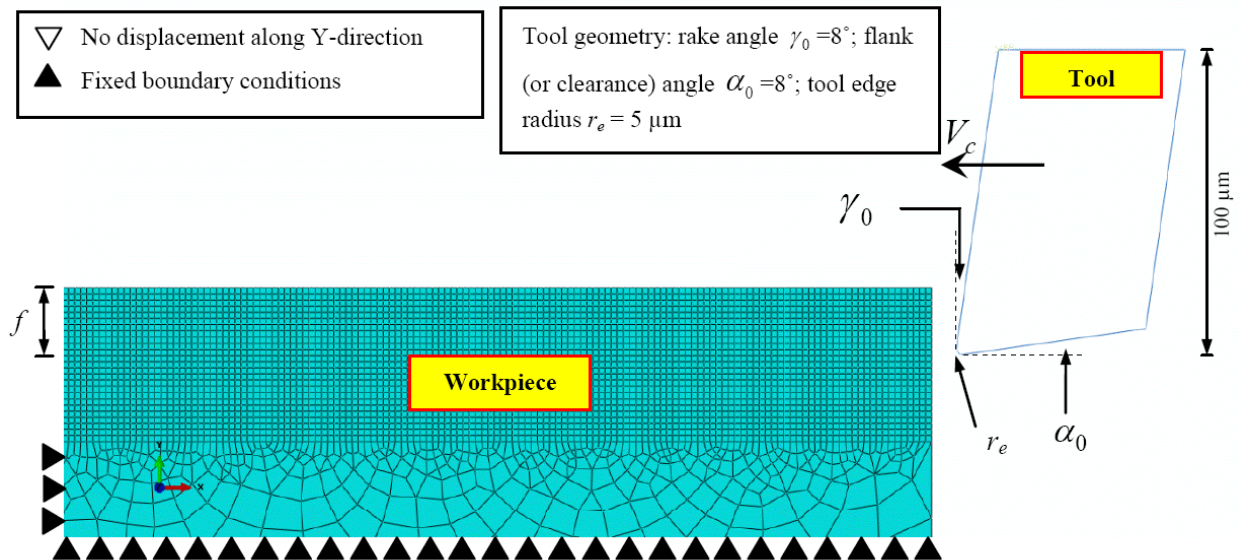
Figure 6.1: FEA model setup for micro-cutting MMCs with nano reinforcements

The mechanical properties of Mg-MMCs are from literature [18], and the detailed parameters are summarized in Table 6.1. The percentage value in the first column indicates the weight fraction of the reinforcements in the composite materials. As it can be seen, the modulus

increases as the weight fraction increases. However, the ductility decreases as the weight fraction increases. Monotonic trends are not observed for yield strength and ultimate tensile strength, which exhibit largest values around 10.2 wt. %.

Table 6.1: Mg-MMCs mechanical properties of ambient room temperature [18]

Material	Modulus E (GPa)	0.2% YS (MPa)	UTS (MPa)	Ductility (%)
Mg	39.82	153±8	207±4	9.2±1.4
Mg/4.8% SiC	45.60	182±2	219±2	2.1±0.9
Mg/10.2% SiC	47.22	171±3	221±14	1.5±0.2
Mg/15.4% SiC	48.24	155±1	207±9	1.4±0.1

In order to use above material properties in FEA cutting models, the Johnson-Cook constitutive model is used to calibrate material plasticity. Since the data in Table 6.1 was obtained at ambient room temperature under quasi-static condition, the rate dependence and the temperature dependence are not considered in this study. Therefore, the material constants of rate and temperature dependences are set to be the same (0.013 and 1.5 [155]) for all four different materials. Therefore, the volume fraction effect on the cutting performance can be revealed.

Recall the Johnson-Cook plastic flow stress is expressed by:

$$\bar{\sigma} = [A + B(\bar{\varepsilon}^{pl})^n][1 + C\ln(\frac{\dot{\bar{\varepsilon}}^{pl}}{\dot{\varepsilon}_0})][1 - (\frac{T - T_{room}}{T_{melt} - T_{room}})^m]$$

(51)

The identified parameters C_2 and n for four different materials are shown in Table 6.2 and the stress-strain curve comparison is shown in Figure 6.2.

Table 6.2: Identified plastic flow parameters for Mg-MMCs

	Mg	Mg 4.8% SiC	Mg 10.2% SiC	Mg 15.4% SiC
Volume fraction	0	3.06 Vol.%	7.35 Vol.%	10.68 Vol.%
C_2	291.8	315	397	410.5
n	0.1026	0.08702	0.1342	0.1555
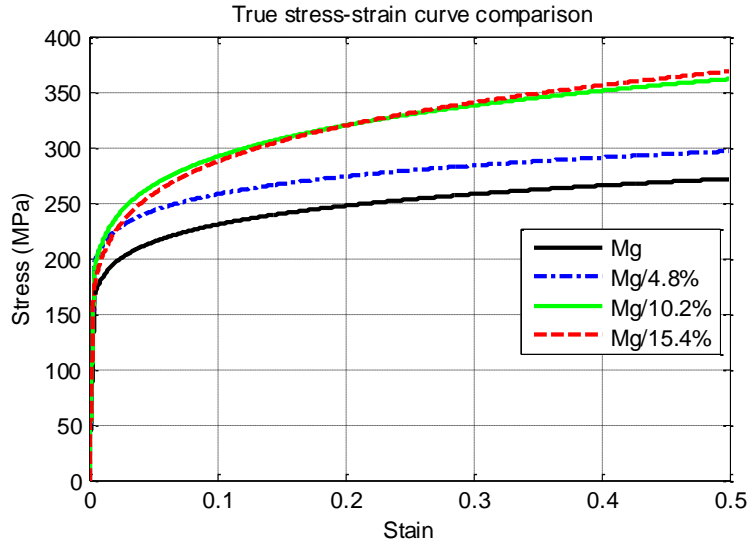
Figure 6.2: Identified stress-strain curve comparison for Mg-MMCs

The fracture model of the MMCs materials is applied by incorporating the triaxiality-based Johnson-Cook dynamic failure criterion, which is recalled as below:

$$\bar{\varepsilon}_f^{pl} = (d_1 + d_2 e^{d_3\eta})[1 + d_4 \ln(\frac{\bar{\dot{\varepsilon}}^{pl}}{\dot{\varepsilon}_0})](1 + d_5\hat{\theta}_T) \tag{52}$$

By using the ductility value in Table 6.1 as a reference point, the triaxiality curve can be regressed by using a reasonably estimated fracture strain value at -1/3 triaxiality point. The identified parameters d2 and d3 for all the four different materials are shown in Table 6.3. The triaxiality comparison is depicted in Figure 6.3. Similarly, due to lack of experimental data for mechanical properties at different temperatures and different strain rates, the temperature and rate dependency are not considered in this study. Thus, a constant value (1) is assigned to d_4 and d_5 parameters for all four different materials.

Table 6.3: Identified fracture parameters for Mg-MMCs

	Mg	Mg 4.8% SiC	Mg 10.2% SiC	Mg 15.4% SiC
Volume fraction	0	3.06 Vol.%	7.35 Vol.%	10.68 Vol.%
d_2	0.2895	0.1293	0.1059	0.1032
d_3	-3.719	-6.138	-6.736	-6.814
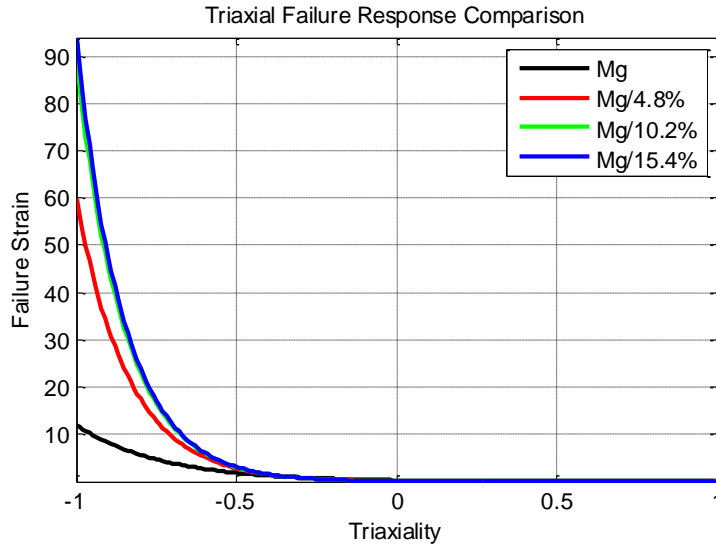
Figure 6.3: Identified triaxiality comparison for Mg-MMCs

The melting temperature of Mg-based alloys and composites from literature [156] is used for Mg-MMCs in this study. The melting temperature is set to be 1085 °C and the transition temperature is set to be 20 °C. In the J-C fracture model, the temperature dependency parameter d_4 is assumed to be unity.

Moreover, based on research findings in previous chapter, damage evolution of the workpiece material is considered in this study. The fracture mode I energy for Magnesium (15 GPa) is applied in a linear manner into the J-C fracture model for all four different materials.

Based on following equations, uncut chip thickness and cutting velocity can be calculated from selected micro end-milling conditions.

$$\bar{f}_t = d_p = \frac{60f}{Nn}$$

(53)

$$v = \frac{\pi Rn}{30}$$

(54)

where n is spindle speed; v is the tangential cutting velocity in local configuration; f is feed speed; d_p is depth of cut; N is the number of teeth of the cutting tool and R is the cutting tool diameter.

According to the above equations, the cutting conditions of this cutting simulation study are designed as below.

Table 6.4: Micro-cutting conditions design for Mg-MMCs

Cutting condition	Value
Rake angle (°)	8, 0, -8
Tool edge radius (μm)	2, 3.5, 5
Depth of cut (μm)	0.5, 1.71, 3, 10, 20, 50
Cutting speed (mm/s)	699.2

6.1.2 Results on Micro-cutting of Homogenized MMCs

FEA micro-cutting simulation results using homogenized material properties for nano-MMCs are summarized in this section. Stress, pressure and strain distributions are compared between pure Mg and Mg-MMCs. Moreover, chip morphology, cutting force and machined surface roughness are also analyzed. The simulation results in this section are based on cutting condition: rake angle 8°; tool edge radius 2 μm; depth of cut 20 μm; cutting speed 699.2 mm/s.

Figure 6.4 illustrates the Von Mises stress distribution in the deformed cutting chips for pure Mg and Mg-MMCs with different weight fractions. Except the 4.8 wt.% Mg-MMCs, all other three materials exhibit distinct shear band in the primary cutting zone. The maximum Von

Mises stress occurs consistently at the tool tip, however the value of the maximum Von Mises stress increases with the increase of the weight fraction of nano-reinforcements until weight fraction reaches 10.2 wt.%. When more nanoparticles (15.4 wt.%) are added to the material, the maximum Von Mises stress decreases compared with 10.2 wt.% nano-reinforced Mg-MMCs. The ultimate tensile strength has similar trend as weight fraction of the reinforcement increases.
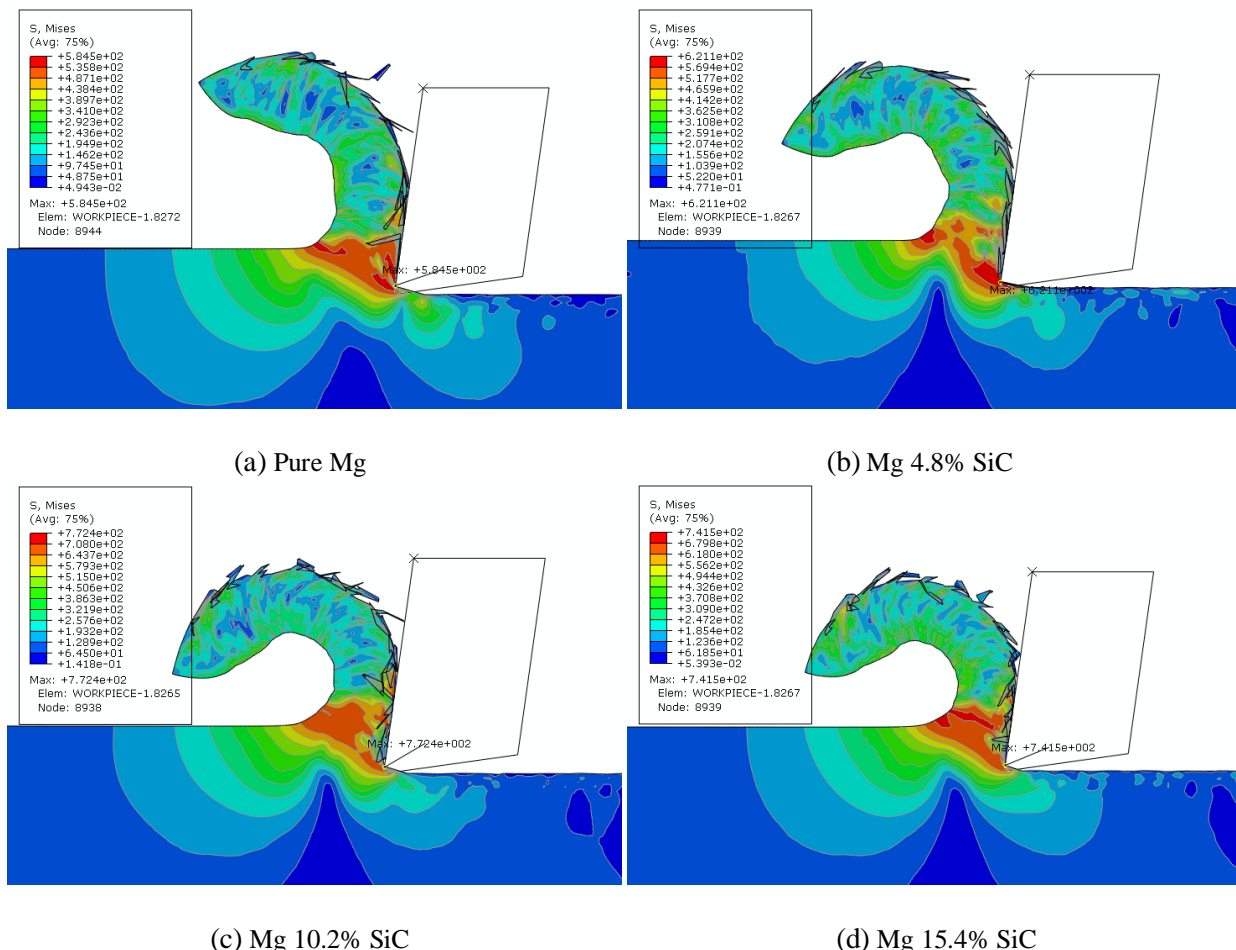
(a) Pure Mg

(b) Mg 4.8% SiC

(c) Mg 10.2% SiC

(d) Mg 15.4% SiC

Figure 6.4: Von Mises stress distribution of the (a) Pure Magnesium and (b) ~ (d) Mg-MMCs with different weight fractions of SiC nanoparticles

Figure 6.5 shows the equivalent plastic strain (PEEQ) distributions as the reinforcement's weight fraction is changed. It can be seen that PEEQ distribution pattern does not change much

as weight fraction increases. Large deformations occur on the back of the cutting chips where the maximum PEEQ values are observed in the simulation. The maximum PEEQ value decreases monotonically with the increase of the nanoparticles' weight fraction. A certain amount of elements are removed due to the interface contact force and rough surfaces are obtained on the back of the cutting chips.

(a) Pure Mg

(b) Mg 4.8% SiC

(c) Mg 10.2% SiC

(d) Mg 15.4% SiC
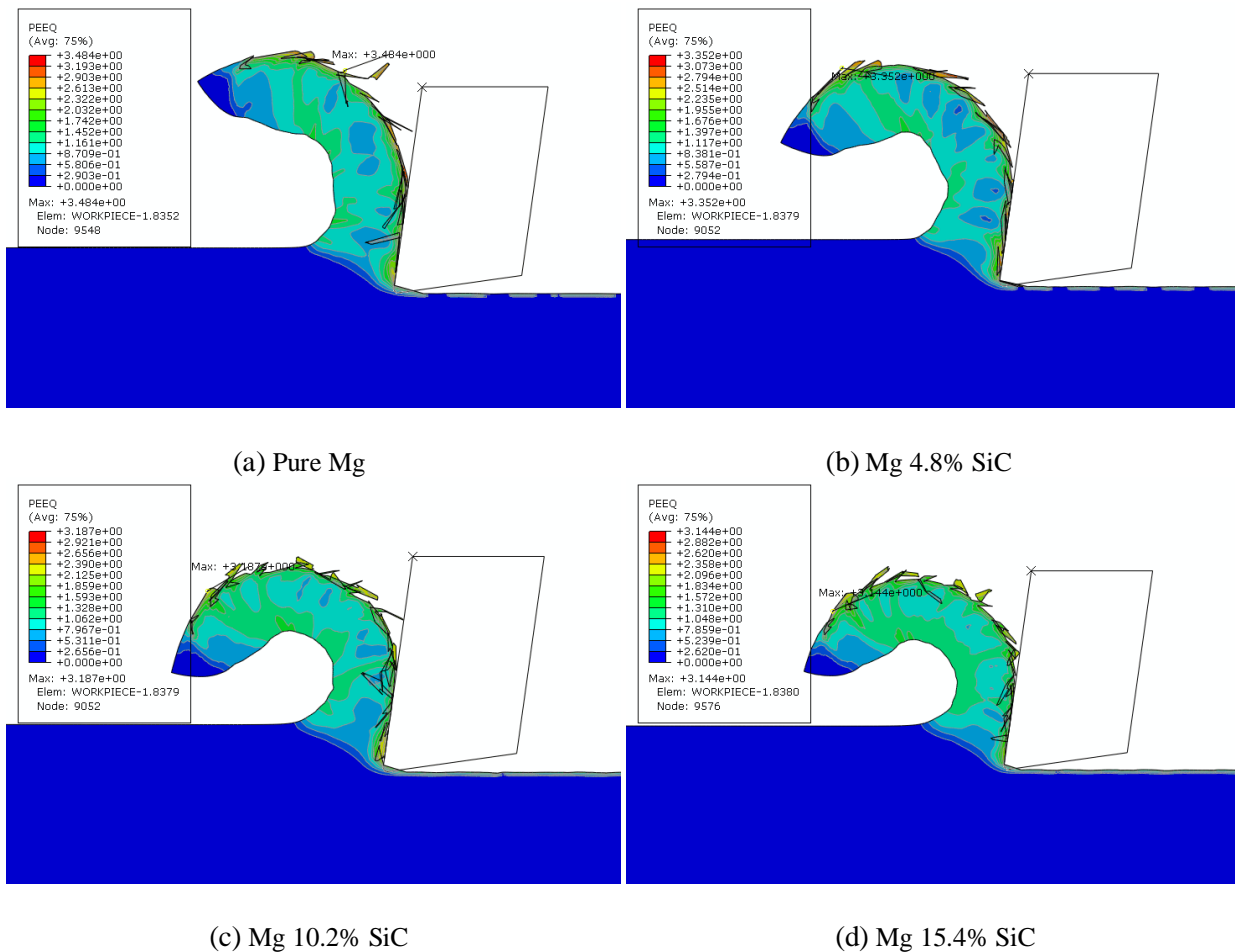
Figure 6.5: Equivalent plastic strain distribution of the (a) Pure Magnesium and (b) ~ (d) Mg-MMCs with different weight fractions of SiC nanoparticles

In Figure 6.6, equivalent pressure stress distributions are shown. For pure Mg, the maximum compressive pressure point occurs at the tool tip and the magnitude is larger than Mg-

MMCs. However, for Mg-MMCs, except the one reinforced with 4.8 wt.% SiC nanoparticles, the other two composites show the maximum compressive pressure point on the cutting tool rake face far from the tool tip. Moreover, the magnitude of the maximum pressure stress increases as the weight fraction increases.

The unique cutting performance of Mg-MMCs reinforced with nanoparticles can also be revealed by observing the tensile pressure stress distributions under and in front of the tool tip. It can be seen that pure Mg shows one single tensile pressure area under the tool tip while all other three composites also show another tensile area in front of the tool tip. Due to the enhanced mechanical strength, these aforementioned two high tensile stress areas merge together in the 15.4 wt.% Mg-MMCs.

(a) Pure Mg

(b) Mg 4.8% SiC
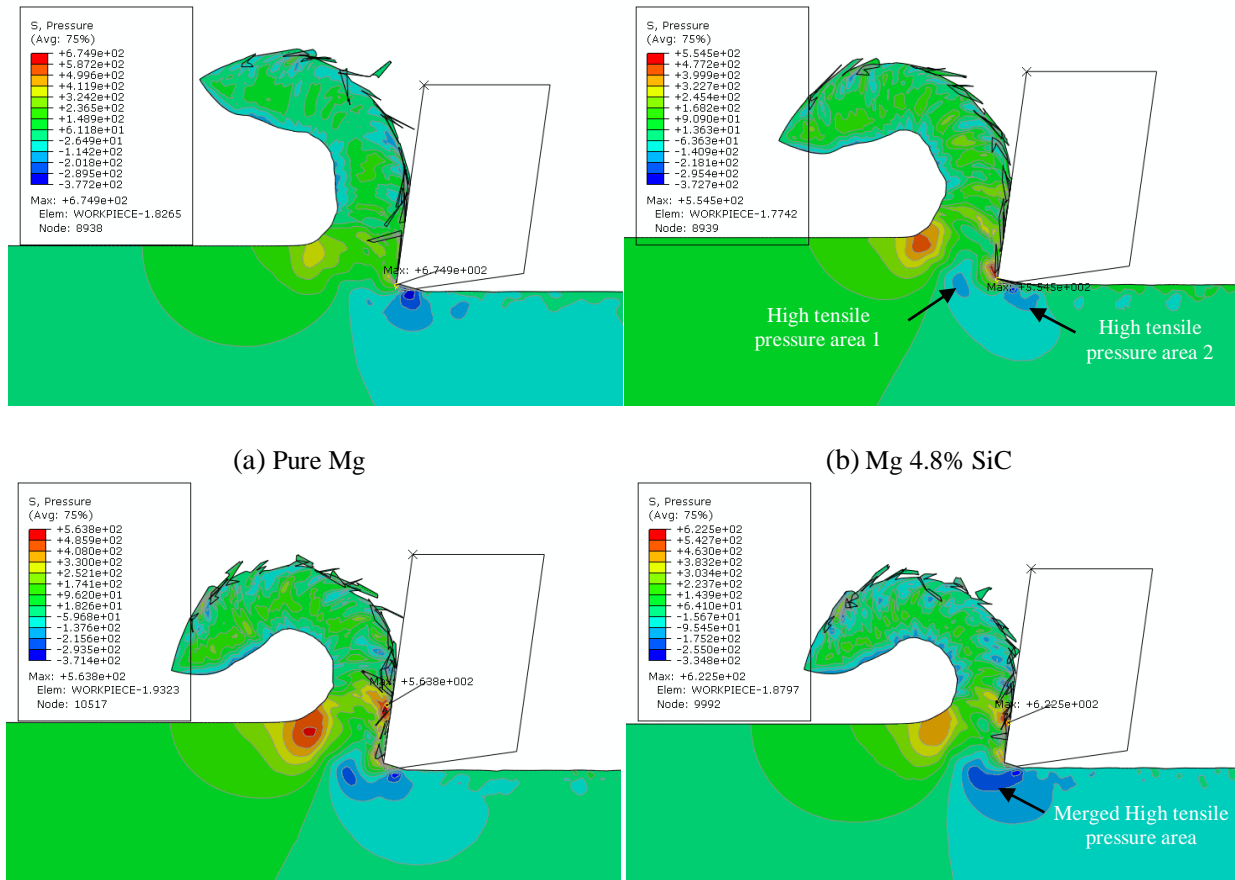
(c) Mg 10.2% SiC

(d) Mg 15.4% SiC

Figure 6.6: Pressure stress distribution of the (a) Pure Magnesium and (b) ~ (d) Mg-MMCs with different weight fractions of SiC nanoparticles

Chip thickness values were obtained by averaging multiple distance measurements across the formed cutting chips. Shear angle values were measured based on the contour of the simulated shear band. All these measurement values are summarized in Figure 6.7. The pure Mg shows smaller chip thickness and smaller shear angle values than Mg-MMCs. This indicates that adding nanoparticles does affect the chip formation in micro-cutting process. However, the effect of the weight fraction on the chip morphology is not significant because the measurements of

149

these two parameters stay relatively steady as weight fraction increases. This phenomenon has also been observed in a previous study for minimum chip thickness testing [62].
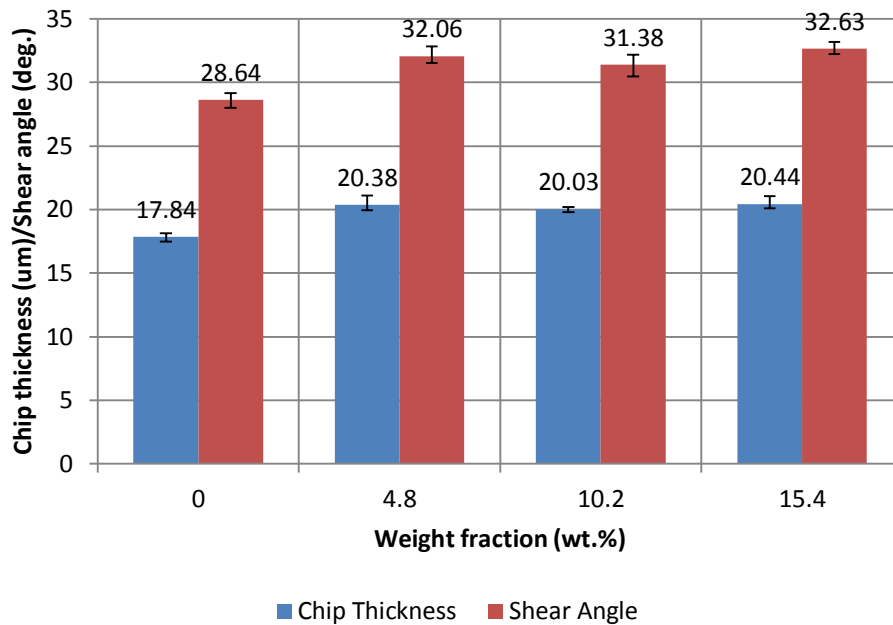
Figure 6.7: Chip morphology comparisons for Pure Mg and Mg-MMCs with different weight fractions from 4.8 ~ 15.4 wt. %

By analyzing the instantaneous cutting force profiles, it can be concluded that the cutting force and the thrust force are not significantly influenced by weight fraction. Cutting force profiles are very similar between pure Mg and Mg-MMCs due to the homogenization assumption. However, difference in average cutting force magnitude can be detected as weight fraction varies (shown in Figure 6.8). In the cutting direction, the average force magnitude (F_x) follows the trend of yield strength and ultimate tensile strength (see Table 6.1). Meanwhile, the average thrust force (F_y) follows the trend of elastic modulus. Surface roughness value was

measured along the machined surface after each simulation by using vertical displacement values.

It also shows the same trend as strength values.
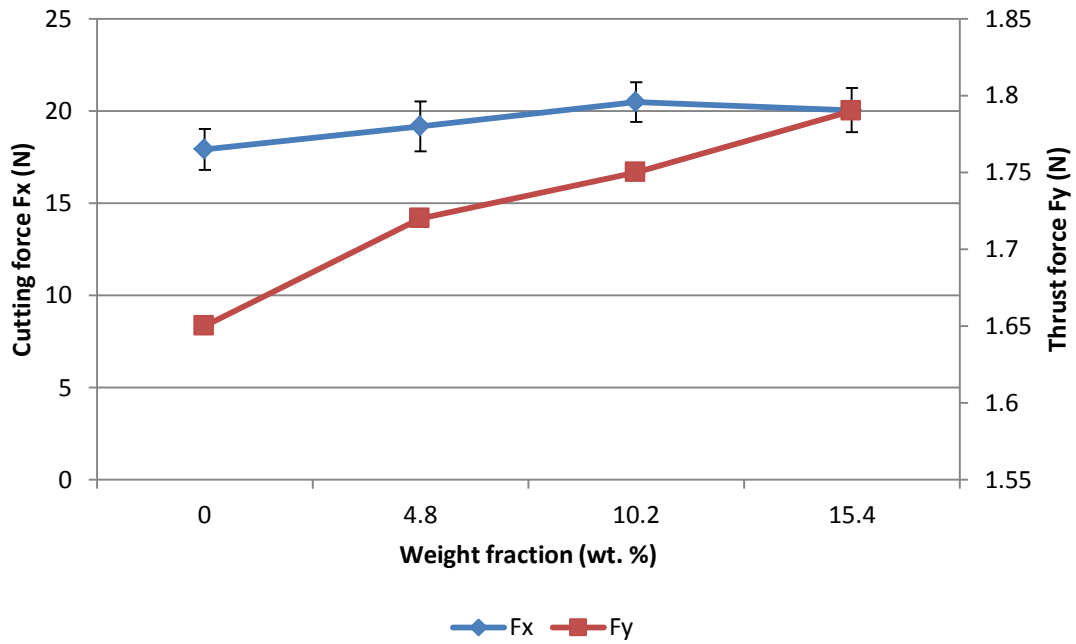
Figure 6.8: Cutting force and thrust force comparisons for Pure Mg and Mg-MMCs with different weight fractions from 4.8 ~ 15.4 wt. %
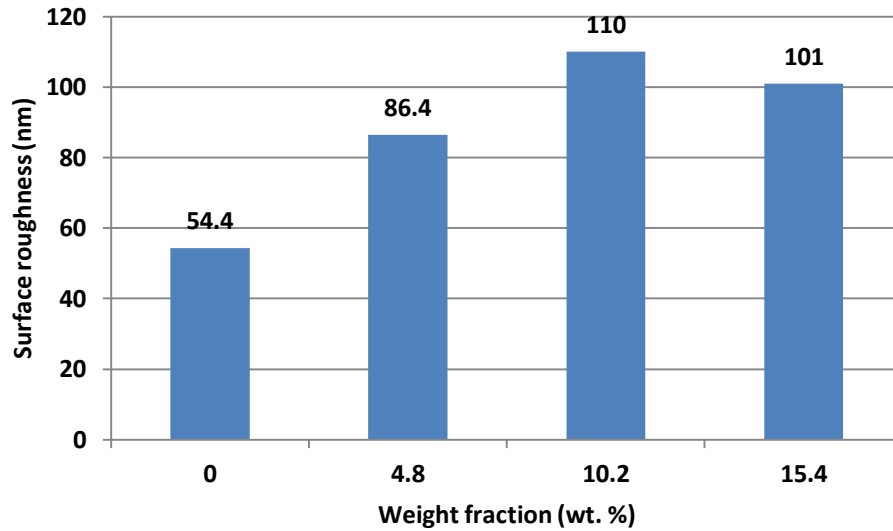
Figure 6.9: Surface roughness comparison for Pure Mg and Mg-MMCs with different weight fractions from 4.8 ~ 15.4 wt. %

In summary, by using calibrated homogenized material properties based on Johnson-Cook plasticity and Johnson-Cook fracture model with damage evolution, the micro-cutting performance of Mg-MMCs can be predicted. The influence of reinforcement nanoparticles and weight fraction (or volume fraction) can be anticipated. Given accurate experimental data for Johnson-Cook models' calibration, the proposed homogenization simulation method is capable of providing accurate trend prediction of the micro-machining process variables, including chip formation, stress-strain distributions, cutting forces and surface roughness.

However, the drawbacks of this method are: (1) the local interaction between the reinforcement particles and the cutting tool cannot be visualized due to the homogenization assumption; (2) it highly depends on experimental data of mechanical properties. Therefore, in order to approach a more fundamental methodology and gain better understanding of

reinforcement particles' influence on cutting performance, the micro/nano structures of the two phase material Mg-MMCs should be constructed in FEA cutting simulation model.

<div align="center">6.2 Modeling of Two Phase Materials</div>

In order to model the microstructure of MMCs in FEA cutting models, different material phases of the composite should be modeled separately into the workpiece with distinct boundary geometries. As for interface modeling between the matrix and the reinforcement particles, there are mainly three methods, including shared nodes method, tie constraints method [85] and cohesive element method [88]. Tie constraint method is computationally expensive because during the simulation frequent contact checks will be conducted on the constrained surfaces. Since the cohesive material properties are still unknown for Mg-MMCs, cohesive element method is not available for Mg-MMCs. Therefore, in this study, the shared nodes method is applied to model the interface. The assumption is made that the fracture of the matrix material surrounding the reinforcement is responsible for particles' debonding and particles' failure, as employed elsewhere in [48]. In Figure 6.10, it shows an example of modeled microstructure of MMCs with uniformly dispersed SiC particles. Meshing procedure is conducted by using Hypermesh and the shared nodes in the matrix-particle interface are applied.
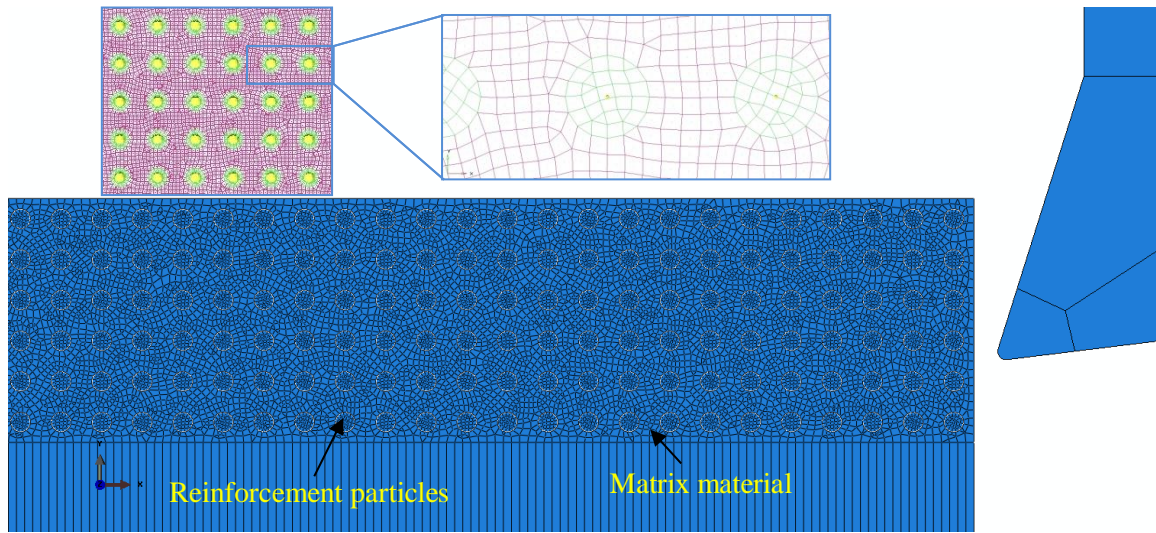
Figure 6.10: FEA micro structural modeling of MMCs materials

Since the matrix metal is ductile metal, the local stress distribution is more complex than that in the homogenized configuration in section 6.1. A suitable fracture criterion based on Chapter 5 is applied here for the matrix material in order to describe its fracture behavior. In this way, the fracture process of micro-cutting MMCs can be predicted. Due to the lack of material constants of the B-W fracture model for pure Mg, the Johnson-Cook fracture model with damage evolution is applied in this chapter. For simplicity, thermal response is not incorporated in this study.

With the purpose of embedding micro-sized ceramic particles and nano-sized ceramic particles into the ductile metal matrix, two appropriate unit systems are designed and implemented for length scales of micrometer and nanometer (as seen in Table 6.5).

Table 6.5: Consistent units for MMCs cutting simulation

Quantity	SI	SI (mm)	SI (μm)	SI (nm)
Length	m	mm	μm	nm
Time	s	s	s	ms
Mass	kg	ton	g	mg
Force	N	N	mN	nN
Temperature	K	K	K	K
Area	m^2	mm^2	$μm^2$	nm^2
Velocity	m/s	mm/s	μm/s	nm/ms
Density	kg/m^3	ton/mm^3	$g/μm^3$	mg/nm^3
Pressure	Pa	MPa	kPa	GPa
Thermal Expansion Coefficient	1/ K	1/ K	1/ K	1/ K
Energy	J	mJ	μJ	nJ
Power	W	mW	μW	μW
Thermal Conductivity	W/m·K	mW/mm·K	μW/μm·K	μW/nm·K
Specific Heat	J/kg·K	mJ/ton·K	μJ/g·K	nJ/mg·K
Fracture Toughness	$Pa\sqrt{m}$	$MPa\sqrt{mm}$	$kPa\sqrt{μm}$	$GPa\sqrt{nm}$

6.3 Micro-cutting of Micro-reinforced MMCs

In this section, the effect of micro-sized reinforcement particles is examined by using a FEA cutting model with explicit material micro-structures. A case study is conducted to simulate the micro-cutting process on micro-reinforced MMCs. The cutting tool is treated as a rigid body in order to reduce computation time. The cutting condition is chosen similarly to the study in section 6.1: tool rake angel 8°, clearance angle 8°, edge radius 2 μm, depth of cut 16~48 μm and cutting speed 699.2 mm/s. Plasticity and fracture property of the matrix material is shown in Table 6.6. The SiC particles are assumed as an elastically deformable body without failure. The

diameter of the particles is 20 μm. The physical properties of the matrix pure Mg and SiC particles are listed as below in Table 6.7.

Table 6.6: Johnson-Cook parameter values for Pure Mg

A	B	n	C	m
153	291.8	0.1026	0.013	1.5
d_1	d_2	d_3	d_4	d_5
0.5	0.2895	3.719	0.013	1.5

Table 6.7: Physical properties of workpiece and cutting tool

Physical parameter	Pure Mg	SiC particles
Density, ρ (kg/m^3)	1738	3200
Elastic modulus, E (GPa)	39.82	408
Poisson's ratio, V	0.35	0.183
T_{melt} (˚C)	600	×
T_{room} (˚C)	20	×

By adding micro-sized SiC particles into Mg metal matrix, the overall chip formation process is different from the one without reinforcement particles. Figure 6.11 shows the chip formation process when micro-cutting micro-reinforced Mg-MMCs using depth of cut 48 μm. Four SiC particles are modeled in the FEA cutting model and dispersed uniformly along the tool path. When the shear band firstly initiates, the shape of the shear band and the stress distribution are similar to homogeneous pure Mg material. As the SiC particle is approached by the cutting tool, it begins to take more stress load due to the shear flow in the shear band. The maximum Von Mises stress point begins to appear on the particle (Figure 6.11 (b)).
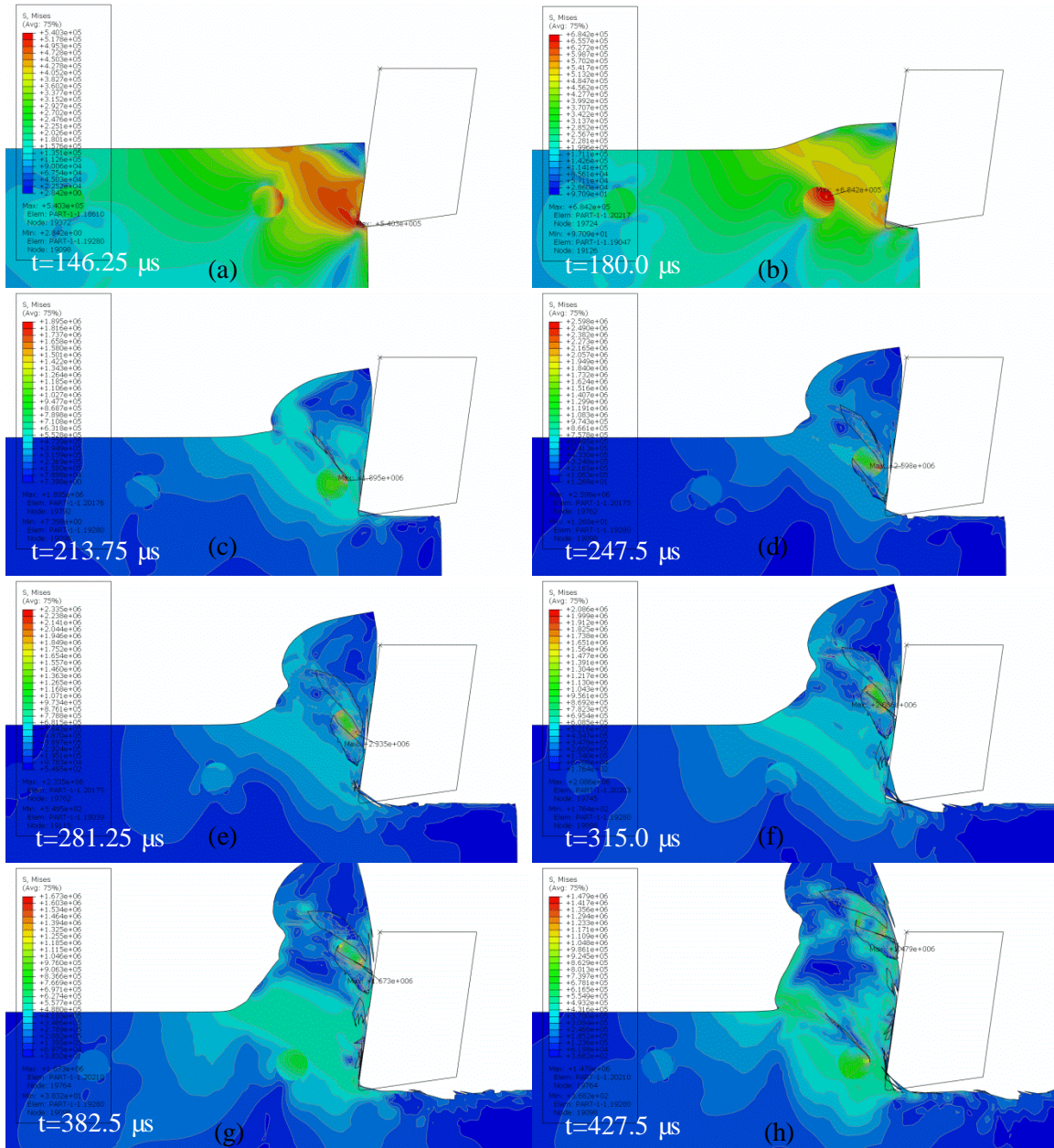
Figure 6.11: Chip formation process of Mg-MMCs reinforced with micro-sized SiC particles

When the cutting tool approaches to a SiC particle, a crack above the SiC particle is generated (Figure 6.11 (c)) immediately followed by another one underneath the particle (Figure 6.11 (d)). In Figure 6.11(e) and (f), it shows the continuing motion of the SiC particle along the

tool rake face as well as the growth of the formed cracks. At the same time, another SiC particle is approached by the cutting tool and the aforementioned procedure begins to repeat. A zoom-in view of the shear band plastic deformation PEEQ is shown in Figure 6.12, where detailed plastic deformation and SiC particles' behavior are shown.
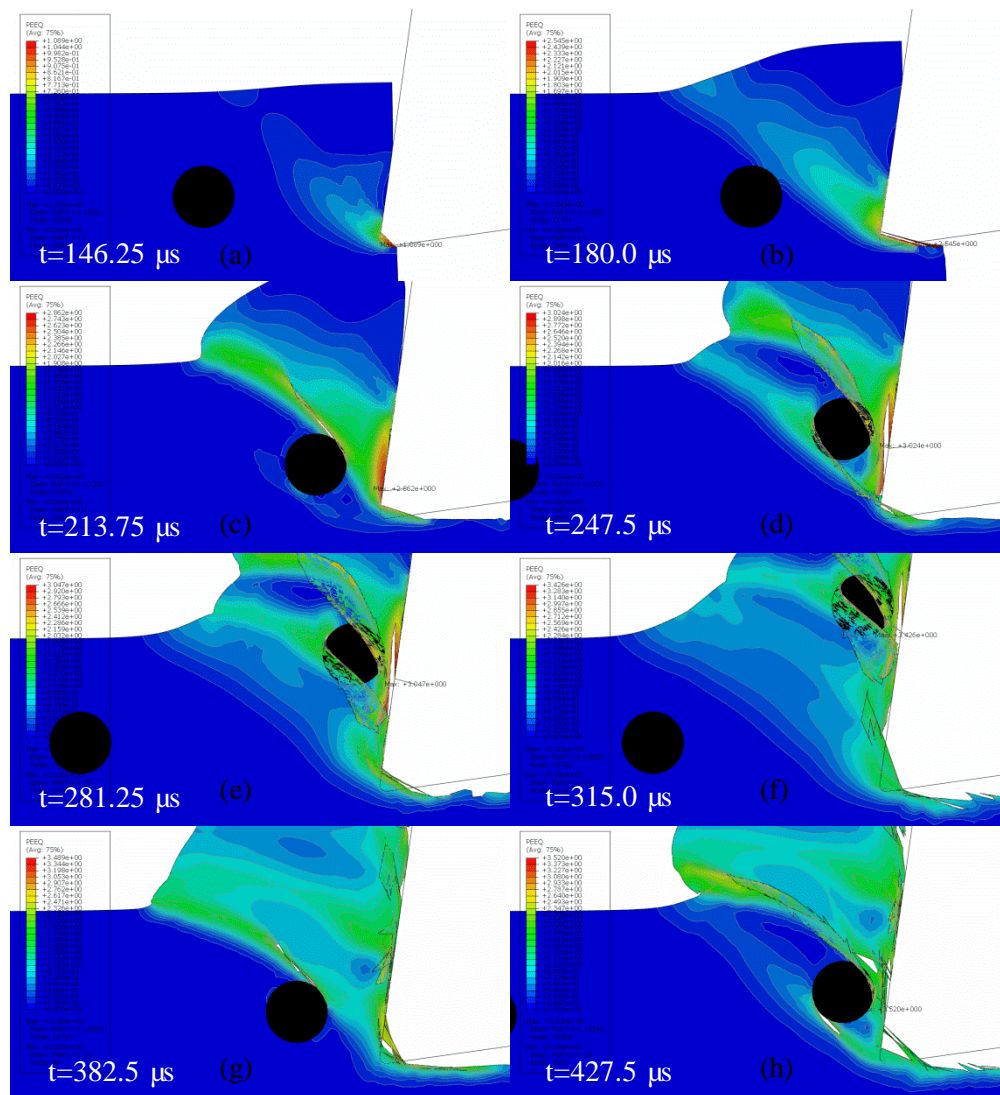
Figure 6.12: PEEQ evolution during the chip formation process for micro-reinforced Mg-MMCs

The reason of the "double-crack" formation mainly comes from the local behavior of the SiC particles interacting with the plastic flowing matrix materials. In this simulation case study, particle rotation phenomenon is present. The plastic flow direction of the matrix material is governed by two major aspects in terms of constitutive model and the tool-workpiece friction model. The former aspect guides the material to go towards the shear band direction regardless of tool rake angle values. However, the latter one forces the materials either to slide apart from the tool tip or towards the tool tip based on various tool rake angle values. As a result, when there exits micro-sized SiC particles in the matrix, the plastic flow of the matrix material will go either beyond the particle or beneath the particle as the cutting tool "pushes" the workpiece material forward.
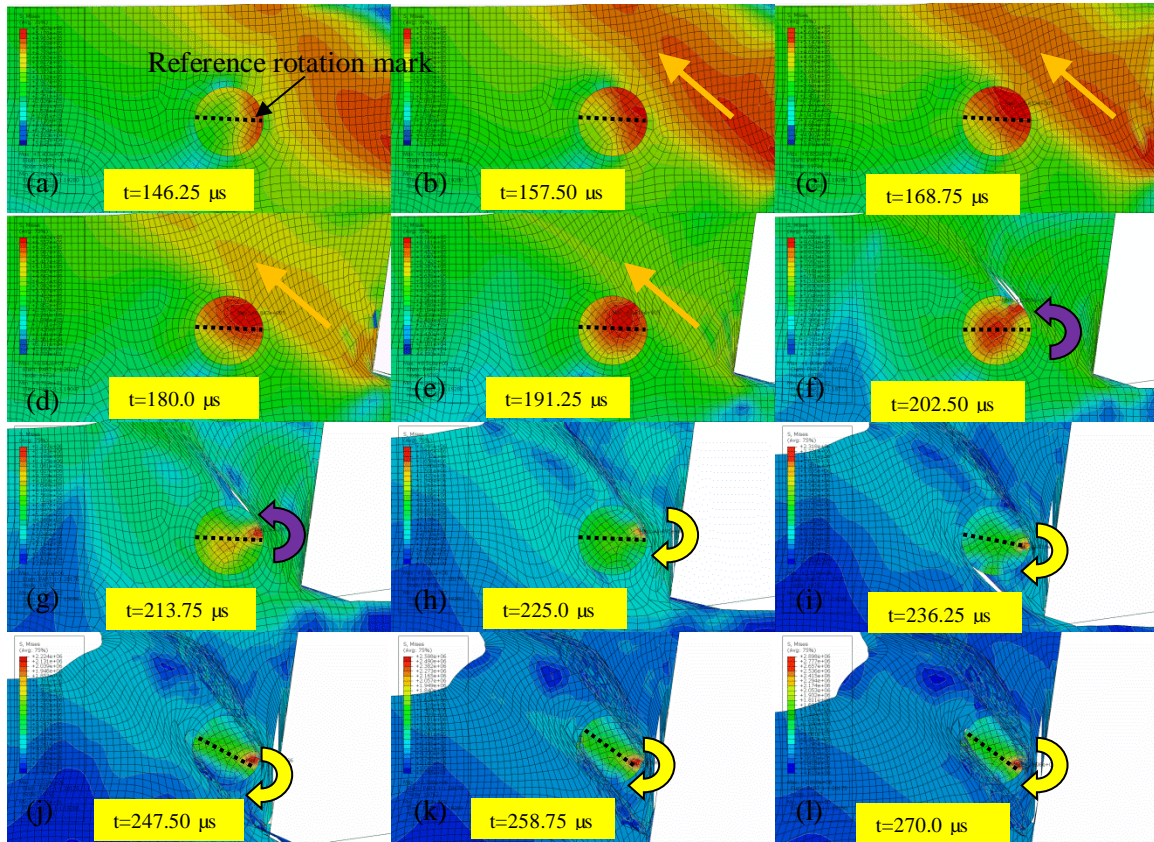
Figure 6.13: Particle rotation during micro-cutting Mg-MMCs

As shown from Figure 6.13, the SiC particle firstly undergoes anti-clockwise rotation due to the dominant shear band plastic flow of the matrix material. During this step, the initial crack above the particle forms (Figure 6.13 (f)). However, as the cutting tool gets closer to the particle, the tool-workpiece interaction plays more important role in governing the material flow adjacent to the SiC particle. Based on the Coulomb friction law, the matrix material will stick on the tool rake face during contacting until the shear stress reaches a critical value. However, the matrix material connecting to the contacting material along the tool paths tends to flow upwards. Therefore, a rotational moment would apply on the SiC particle which exhibits clockwise rotation in the following chip formation process. Even though the SiC particle does not have

160

direct contact with the tool rake face, it seems the SiC particle "rolls" on the rake face as the cutting chip flies up.
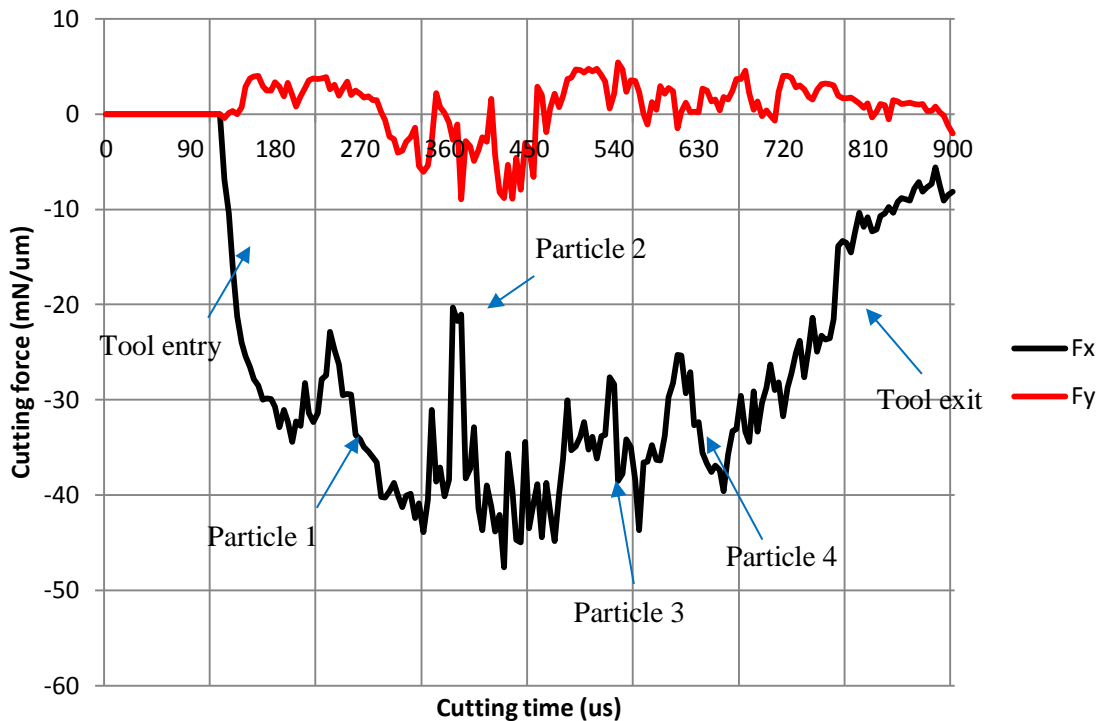
Figure 6.14: Cutting force of Mg-MMCs reinforced with micro-sized SiC particles

Figure 6.14 presents the cutting force profile of micro-cutting Mg-MMCs reinforced with micro-sized SiC particles. The maximum cutting energy along the cutting direction is around 937.5 MPa. The thrust force (F_y) is more difficult to predict for Mg-MMCs than its homogeneous counterpart. According to previous simulation results, although the particles do not interact directly with the cutting tool rake face, cutting force (F_x) still has large fluctuations when a particle is being cut. Due to the short cutting length in this simulation, the effect of the

reinforcement particles is also mixed with the tool entry and exit effects, thus the force fluctuation magnitude is not adequately consistent during this test.

6.4 Micro-cutting of Nano-reinforced MMCs

In this section, a simulation case study is conducted to simulate the micro-cutting of nano-reinforced MMCs. The effect of nano-sized reinforcement particles is examined by using a FEA cutting simulation model with explicit material micro-structures. Cutting tool is modeled as an elastic deformable component and its properties are similar as shown in Table 5.2. Cutting conditions are chosen as below: tool rake angel 8˚, clearance angle 8˚, edge radius 0.1 μm, depth of cut 100 nm and cutting speed 699.2 mm/s. Plasticity and fracture property of the matrix material is shown in Table 6.6. The SiC particles are assumed to be elastic deformable body without failure definition. The diameter of the particles is 50 nm. The physical properties of matrix pure Mg and SiC particles are listed in Table 6.7.

Figure 6.15 shows the chip initiation process during micro-cutting nano-reinforced Mg-MMCs. The initial crack appears underneath the first ceramic nanoparticle. As the cutting tool advances, the cracks above the nanoparticles begin to show up along the shear band direction. Eventually, a triangle shaped chip is formed and tends to fly up along the tool rake face as seen in Figure 6.15(d).
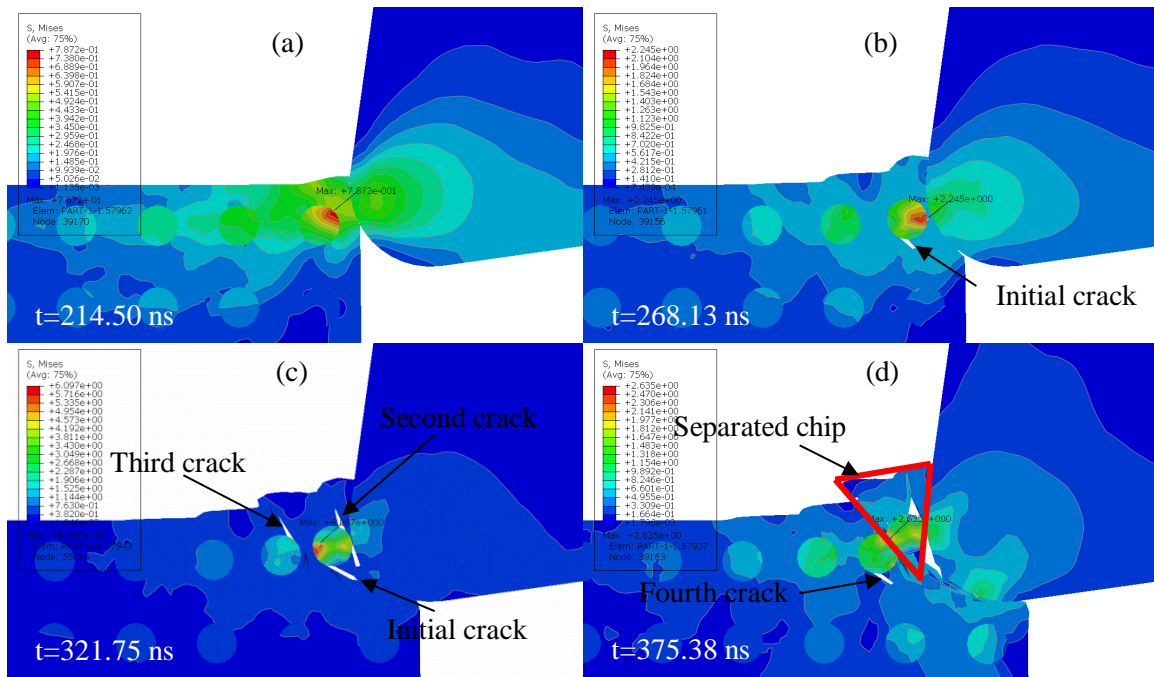
Figure 6.15: Chip initiation process of Mg-MMCs reinforced with nano-sized SiC particles

Figure 6.16 illustrates the chip formation mechanism in the steady state cutting process for nano-reinforced Mg-MMCs. Under the tested cutting condition for nano-reinforced Mg-MMCs, the chip formation is different from traditional homogeneous material. Due to the existing nanoparticles, continuous cutting chips cannot be generated. Instead, triangular intermittent chips form, which either fly out or stick on the machined surface. This indicates the nanoparticles greatly change the ductility of the material in micro-scale. A "double shear band" appears which forces a certain amount of matrix material and a single particle to form a triangular intermittent chip. This phenomenon is shown in detail in Figure 6.17.
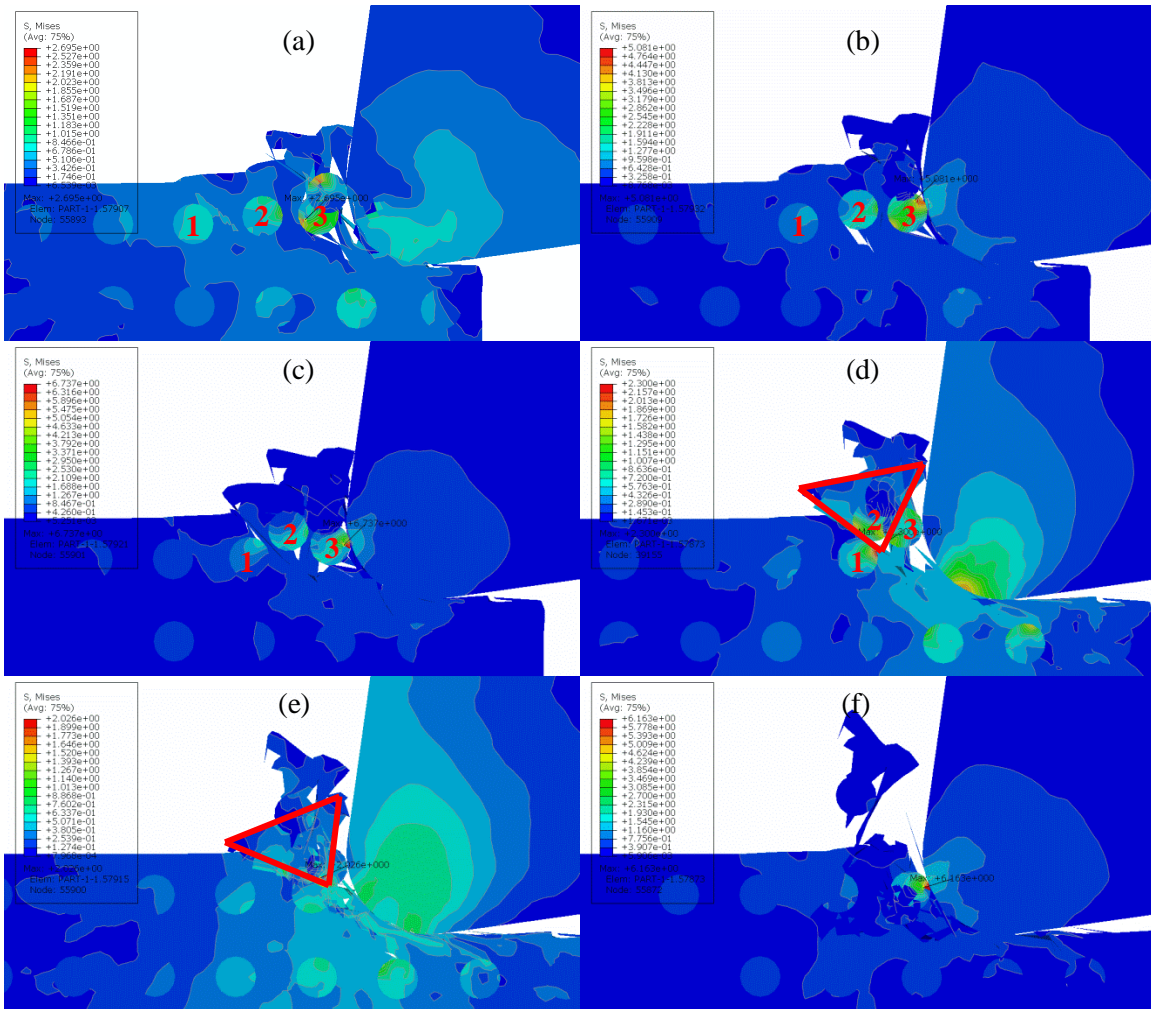
Figure 6.16: Steady chip formation process of Mg-MMCs reinforced with nano-sized SiC particles

Figure 6.17 shows the PEEQ distribution of the steady state cutting process for nano-reinforced Mg-MMCs. The evolutions of the three nanoparticles marked as #1, #2 and #3 are clearly demonstrated. As the cutting tool interacts with particle #3, particle #3 moves forward as part of the cutting tool. Thus it enhances the formation of regular shear band towards the cutting direction. As the particle #2 is slightly sheared up with some matrix material, due to the symmetry position of particles #1 and #3 relative to particle #2, particle #1 can be viewed as a "tool tip" moving towards particle #3. Therefore, another shear band towards the cutting tool is

164

formed and the "double shear band" is shown in Figure 6.17(b) and (c). After the shear bands initiate, cracks are generated inside the shear bands and the triangular cutting chip with a single nanoparticle is formed until it releases from the workpiece. Similar observations can also be obtained by analyzing the particles #1~3 marked in Figure 6.16(a) ~ (d). Since there are no formed continuous chips, particles' rotation is not noticeable for nano-reinforced Mg-MMCs.
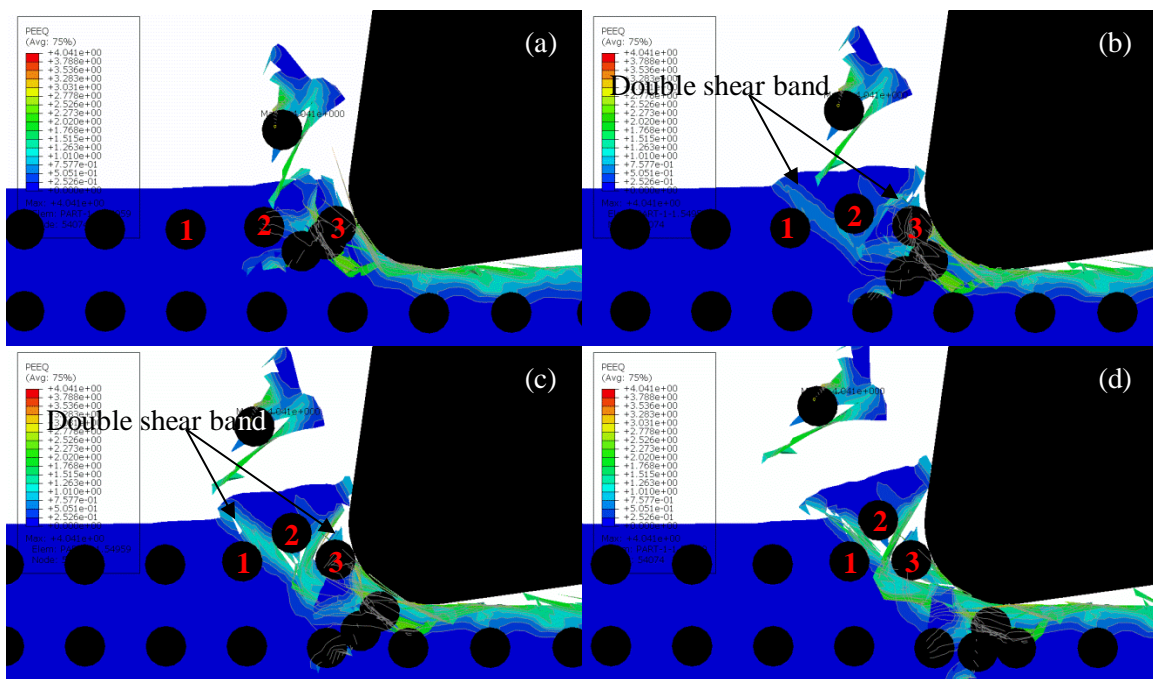
Figure 6.17: PEEQ distribution of micro-cutting Mg-MMCs reinforced with nano-sized SiC particles

Figure 6.18 shows the cutting force responses of nano-reinforced Mg-MMCs. Due to the small depth of cut, tool edge radius effect and intermittent chip formation mechanism, very limited amount of workpiece material can slide onto the tool rake face. Therefore, the thrust cutting force is mainly ploughing force and pushing the cutting tool away from the workpiece. Therefore, the magnitude and profile of thrust force are different from its micro-reinforced counterparts as shown in section 6.3.

Moreover, the nanoparticles have significant influence on the cutting force behavior. As it can be seen in Figure 6.18, the cutting force has periodic fluctuations which correspond to the formation of triangular cutting chips. Each time when "double shear band" initially forms, the cutting force reaches its maximum magnitude. When the chips are released, the force value drops to a valley. The average cutting force value in the lateral cutting direction is 112.76 μN/μm and the corresponding cutting energy is 1.12 GPa.
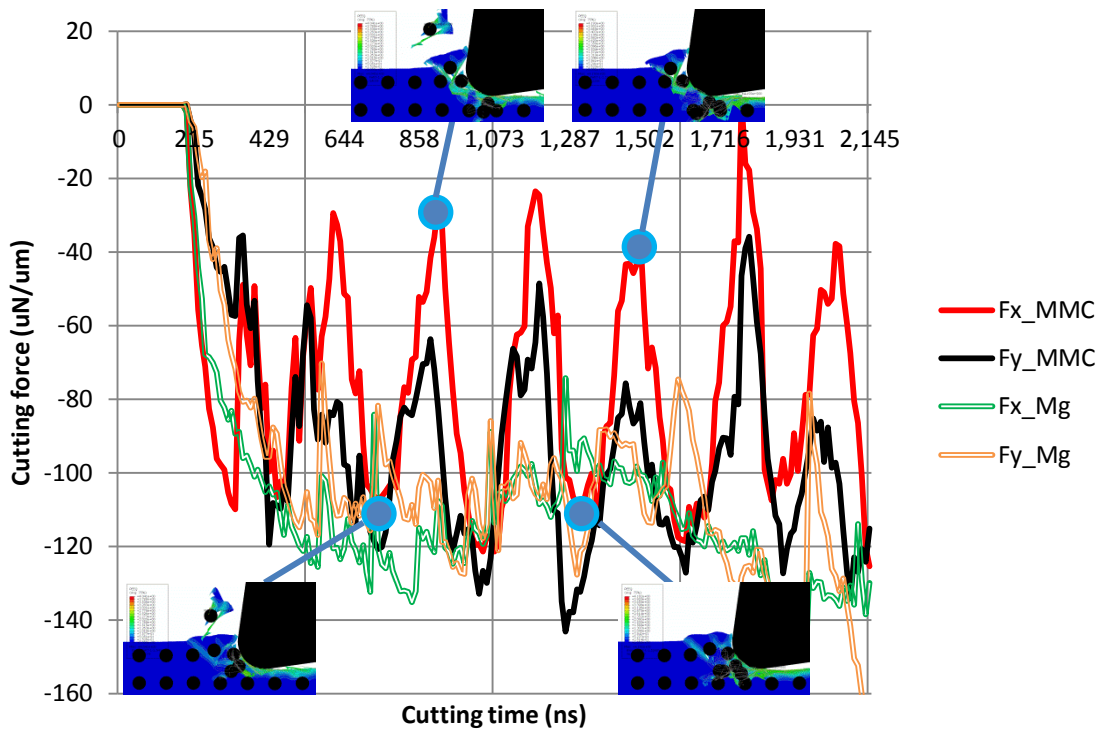
Figure 6.18: Cutting forces of micro-cutting Mg-MMCs reinforced with nano-sized SiC particles

6.5 Summary

In this chapter, micro-cutting simulations are conducted by using FEA cutting simulation model for Mg-MMCs reinforced with SiC ceramic particles. Both homogenized Mg-MMCs material model and heterogeneous material model are evaluated. The following conclusions can be reached:

1). By using homogenized material properties based on Johnson-Cook plasticity and Johnson-Cook fracture model with damage evolution, the micro-cutting performance of nano-reinforced Mg-MMCs can be predicted. The overall micro-cutting performance has similar trend to the material's mechanical properties. As long as accurate experimental data can be obtained for calibration, the proposed homogenization FEA micro-cutting model is capable of providing accurate trend prediction of micro-machining variables, including chip formation, stress-strain distributions, cutting forces and surface roughness.

2). Crack generation mechanism for Mg-MMCs reinforced with SiC particles is different from that of its homogeneous counterpart. Moreover, the behavior of the reinforcement particles varies with particle size. Under the tested cutting conditions in this simulation study, the effect of micro-sized particles is different from the one of nano-sized particles on micro-cutting performance.

3). When machining micro-reinforced Mg-MMCs, different from generating a single crack in the shear band for homogeneous materials, the fracture crack firstly initiates above the SiC particle and then immediately occurs underneath the particle. Particle rotation phenomenon is present, which is the fundamental reason of the "double-crack" mechanism.

4). When machining nano-reinforced Mg-MMCs with a depth of cut close to the tool edge radius, the fracture cracks also initiate beside the ceramic particles, either above or underneath the nanoparticle depending on whether it is in the initial transit cutting or the steady state cutting. Triangular shaped cutting chips are formed intermittently, which is the result of the "double shear band" mechanism due to the existence of nanoparticles.

CHAPTER 7   CONCLUSION AND FUTURE WORK

7.1 Summary and Conclusions

This research was motivated by increasing demands of miniaturized components in various industrial applications. Mg-MMCs become one of the best material candidates due to its light weight, high strength, and high creep/wear resistance. However, the improved mechanical properties have brought great challenges to the subsequent micro-machining process. The objective of this study was to develop analytical and numerical process models for mechanical micro-machining of heterogeneous materials such as Mg-MMCs. These models were constructed to assist in selecting process parameters for micro-machining of advanced materials as well as to gain better understanding of the unique cutting mechanism for particle reinforced heterogeneous materials.

Systematic experimental investigations on the machinability of Mg-MMCs reinforced with SiC nano-particles have been conducted by using the Design of Experiment (DOE) method on the nanocomposites containing 5 Vol.%, 10 Vol.% and 15 Vol.% reinforcements, and pure magnesium. Based on the Response Surface Methodology (RSM) design, experimental models and related contour plots were developed to predict cutting force, surface roughness, and to optimize micro-machining conditions. The varied parameters considered in the experiments are spindle speed, feedrate and volume fraction. Based on the measured cutting force signals and

machined surface roughness, the following conclusions can be reached: i). The normal force F_x, the feed force F_y and the axial force F_z all increase with the increasing of either the spindle speed or the feedrate. The increasing rate of the axial force F_z and the normal force F_x is larger, while that of the feed force F_y is moderate for most cases. ii). The nano-particles' volume fraction has a considerable effect on the cutting force. The cutting force increases accordingly with the increase of volume fraction. The largest increasing slope occurs at the transition from 5 to 10 Vol.%, which is agreeable with the rapid change of material mechanical property around 10 Vol.%. However, when the spindle speed goes up to 60,000 rpm, the increase rate of the cutting forces is much larger than the ones when the spindle speeds are at 20,000 rpm and 40,000 rpm. The increasing slopes of the cutting force are maintained at the same level for both regions of from 5 to 10 Vol.% and from 10 to 15 Vol.%. iii). The influence of a single experimental variable (feedrate, spindle speed or volume fraction) on the machined surface roughness is not obvious. The results from SEM show a decent machined surface can be reached by micro-milling Mg-MMCs. iv). The experimental models derived by Response Surface Methodology Design of Experiment (RSM DOE) can be used to predict the cutting force and the surface roughness with different machining parameters. The related contour plots can be combined together to determine the most suitable cutting conditions for the required cutting force and surface roughness. This method builds the connection between material properties and machining performance successfully.

An analytical cutting force model has been developed to predict cutting forces of nano-reinforced Mg-MMCs in micro-milling process. This model is different from previous ones by encompassing the behaviors of nanoparticles in three cutting scenarios, i.e., shearing, ploughing

and elastic recovery. By using the enhanced yield strength, three major strengthening factors were incorporated including load-bearing effect, enhanced dislocation density strengthening effect and Orowan strengthening effect. To validate the model, various cutting conditions using two types of end mills (diameters as 100 μm and 1 mm) were conducted. The simulated cutting forces showed good agreements with the experimental data. The proposed model can predict major force amplitude variations and force profile changes with the nanoparticles' volume fraction. The effects of the nano-sized reinforcements on the machinability of Mg-MMCs were studied through theoretical analysis and experimental validation. The comparison between the experimental and simulated cutting forces implies that the proposed model can effectively capture the major cutting force characteristics of nano-reinforced Mg-MMCs. According to the simulation and experimental results, some important findings are concluded: i). Cutting force magnitudes greatly increase as the nanoparticles' volume fraction increases. This is attributed to the improved yield strength and fracture strength by adding SiC nanoparticles. The phenomenon is more obvious when using a larger diameter cutting tool. ii). Cutting force profiles of Mg-MMCs are not as smooth as those of pure Mg. The reason for that is the existence of ceramic nanoparticles influences the chip formation of Mg-MMCs. Mg-MMCs with different volume fractions of nanoparticles express different strengthened yield strengths and fracture strengths. Therefore, the cutting mechanisms and the SiC particles' behaviors in three cutting regimes are different. Consequently, cutting force profiles behave differently among pure Mg and Mg-MMCs with different volume fractions. iii). When using 100 μm cutting tools, all the cutting forces under the investigated cutting conditions on Mg-MMCs do not exhibit crisp force profiles for each tooth. As the volume fraction increases, more disturbances show up and the feed

direction force displays more distinct trend to split into two teeth in a single revolution. Moreover, compared to 1 mm tool, the peak-to-peak cutting force increasing trend with the rising of volume fraction is not obvious. This is mainly due to the small size and low rigidity of the 100 μm tool. Consequently, the tool vibration/deflection plays more influential role in altering cutting force profiles rather than the strengthening effect of nanoparticles.

Furthermore, a comprehensive evaluation of ductile fracture models has been conducted to identify the most suitable fracture criterion for metal cutting processes. Six fracture models are evaluated in this study, including constant fracture strain, Johnson-Cook (J-C), J-C coupling criterion, Wilkins, modified Cockcroft-Latham, and Bao-Wierzbicki (B-W) fracture criterion. Results indicate that by coupling with the damage evolution, the capability of J-C and B-W can be further extended to predict accurate chip morphology. B-W based coupling model provides the best simulation results in this study. The major results are summarized as below: i). The constant fracture strain model fails to provide accurate chip morphology prediction in a wide range of failure strains. The Wilkins fracture model also cannot provide accurate continuous chip formation prediction. The experimental shear angle, cutting temperature, cutting force and surface roughness values are not satisfied from these two fracture criteria. ii). The Johnson-Cook fracture model and the empirical Bao-Wierzbicki fracture model formulated in the space of stress triaxiality and equivalent fracture strain are capable of predicting realistic stress/strain/temperature distributions, cutting forces and surface roughness. However, pure J-C model is not sufficient to predict chip formation and cutting forces, due to the ignorance of the "cut-off" value for ductile metal when triaxiality is less than -1/3 (chip formation becomes more intermittent and cutting force has excessive fluctuations). iii). By coupling with material damage

evolution and its fracture energy, the capability of Johnson-Cook and Bao-Wierzbicki can be further extended to predict accurate chip morphology. The fracture model with damage evolution has better performance than those without damage evolution. It is recommended to consider damage evolution in FEA cutting simulations. Otherwise, certain amount of energy will be lost and prediction results will be adversely affected. iv). The B-W fracture model with consideration of rate dependency, temperature effect and damage evolution is the most comprehensive model to describe the chip removal behavior of ductile materials. The only drawback is that this comprehensive fracture criterion requires numerous fracture parameters, some of which are difficult to be obtained from experiments directly.

A 2-D FEA micro-cutting model has been constructed to study the micro-cutting performance of Mg-MMCs materials. Firstly, homogenized material properties were employed to evaluate effect of the volume fraction. Secondly, micro-structures of the two-phase material were modeled explicitly in FEA cutting models. The effects of SiC particles were evaluated in two case studies. By using the homogenized material properties, the micro-cutting performance of nano-reinforced Mg-MMCs can be predicted. During micro-cutting process, crack generation mechanism of Mg-MMCs is different from its homogeneous counterparts. Both the homogenized Mg-MMCs material model and heterogeneous material model were evaluated. The following conclusions can be reached: i). By using homogenized material properties based on Johnson-Cook plasticity and Johnson-Cook fracture model with damage evolution, the micro-cutting performance of nano-reinforced Mg-MMCs can be predicted. The overall micro-cutting performance has similar trend to the material's mechanical properties. As long as accurate experimental data can be obtained for calibration, the proposed homogenization FEA micro-

173

cutting model is capable of providing accurate trend prediction of micro-machining variables, including chip formation, stress-strain distributions, cutting forces and surface roughness. ii). Crack generation mechanism for Mg-MMCs reinforced with SiC particles is different from that of its homogeneous counterpart. Moreover, the behavior of the reinforcement particles varies with particle size. Under the tested cutting conditions in this simulation study, the effect of micro-sized particles is different from the one of nano-sized particles on micro-cutting performance. iii). When machining micro-reinforced Mg-MMCs, different from generating a single crack in the shear band for homogeneous materials, the fracture crack firstly initiates above the SiC particle and then immediately occurs underneath the particle. Particle rotation phenomenon is present, which is the fundamental reason of the "double-crack" mechanism. iv). When machining nano-reinforced Mg-MMCs with a depth of cut close to the tool edge radius, the fracture cracks also initiate beside the ceramic particles, either above or underneath the nanoparticle depending on whether it is in the initial transit cutting or the steady state cutting. Triangular shaped cutting chips are formed intermittently, which is the result of the "double shear band" mechanism due to the existence of nanoparticles.

Through this research, a better understanding of the unique cutting mechanism for particle reinforced heterogeneous materials has been obtained and the effect of reinforcements on micro-cutting performance is revealed. The proposed analytical and numerical models can be used to optimize process parameters for both preparing and micro-machining of the heterogeneous material. This will eventually facilitate the automation of MMCs' micro-machining process.

7.2 Future Work

Micro-machining of particle reinforced heterogeneous materials is a new research area and shows promise of applying into various industries such as aerospace, energy, medical and transportation, which are demanding large amount of high performance mechanical components in small scales. However, one must answer many questions on materials science, micro-mechanics, fracture mechanics, and manufacturing engineering in order to fully understand and be able to control the process. Although this study has provided an initial investigation on Mg-MMCs, more work is still needed to be achieved to further understand the underlying phenomena and to improve the process conditions. With the purpose of enhancing prediction capability of the proposed process models, following research work is recommended for future research regarding MMCs' mechanical micro-machining.

1). Calibration of mechanical properties of Mg-MMCs: Homogenized mechanical properties for Mg-MMCs should be calibrated in order to acquire accurate parameters for further constitutive modeling study and fracture mechanism study. Accurately calibrated elasticity, plasticity and fracture properties of pure Mg and SiC are also needed for FEA micro-cutting models and interface behavior study.

2). Modeling of reinforcement interface: Properties of the interface between matrix material and reinforcement material are important and influencing the behavior of the reinforcements during the micro-machining process. Therefore, the interface properties should be systematically studied through experimental and modeling approaches. Appropriate cohesive zone model and its parameters are desired to integrate into micro-cutting process models.

3). Tool wear study for Mg-MMCs: The improved strength and abrasive nature of the reinforcements bring great challenges for the subsequent inevitable machining process. Tool wear is one of the challenges. The tool wear of machining Mg-MMCs should be studied through experimental approach. The effects of the particle size, cutting conditions and tool coating on the tool wear should be systematically analyzed. Moreover, the machined surface quality and instantaneous cutting forces could be correlated with the tool wear by using advanced signal processing techniques. Based on the results, the tool wear mechanism for particle reinforced heterogeneous materials can be revealed. This will provide important guidelines for selecting cutting conditions in micro-machining ceramic particle reinforced MMCs, and also benefit the online monitoring and control the tool wear.

4). 3-D micro-cutting simulation: Based on properly calibrated constitutive models and fracture models for the matrix, the reinforcement and the bonding interface, a 3-D FEA micro-cutting process model could be constructed and used to predict machinability of MMCs accurately. The FEA modeling technique should be enhanced in order to tackle with high computational cost and computational noise. The proposed scheme can be applied in various micro-cutting processes including micro-turning, micro-milling, micro-drilling etc., and used to optimize machining conditions as well as reach deeper understanding of the micro-cutting mechanism.

LIST OF REFERENCES

[1] Kainer, K. U., 2006, Metal Matrix Composites -- Custom-made Materials for Automotive and Aerospace Engineering, Wiley-VCH Verlag GmbH & Co. KGaA.

[2] Liu, X., 2006, "Cutting mechanisms in micro-endmilling and their influence on surface generation," Ph.D. Dissertation, University of Illinois at Urbana-Champaign.

[3] Chae, J., Park, S. S., and Freiheit, T., 2006, "Investigation of micro-cutting operations," International Journal of Machine Tools and Manufacture, 46(3–4), pp. 313-332.

[4] Rawal, S., 2001, "Metal-matrix composites for space applications," JOM Journal of the Minerals, Metals and Materials Society, 53(4), pp. 14-17.

[5] Deng, W., 2008, "Fundamentals and applications of multiplexed electrosprays," Ph.D. Dissertation, Yale University.

[6] Kyritsis, D. C., Roychoudhury, S., McEnally, C. S., Pfefferle, L. D., and Gomez, A., 2004, "Mesoscale combustion: a first step towards liquid fueled batteries," Experimental Thermal and Fluid Science, 28(7), pp. 763-770.

[7] Aust, E., Elsaesser, M., Hort, N. and Limberg, W., 2006, "Machining of hybrid reinforced Mg-MMCs using abrasive water jetting," 7th Magnesium Technology Symposium, pp. 345-348.

[8] Goh, C. S., Gupta, M., Wei, J., and Lee, L. C., 2007, "Characterization of High Performance Mg/MgO Nanocomposites," Journal of Composite Materials, 41(19), pp. 2325-2335.

[9] Lim, C. Y. H., Lim, S. C., Gupta, M., 2003, "Wear behaviour of SiCp-reinforced magnesium matrix composites," Wear, 255(1-6), pp. 629-637.

[10] Müller, F., and Monaghan, J., 2000, "Non-conventional machining of particle reinforced metal matrix composite," International Journal of Machine Tools and Manufacture, 40(9), pp. 1351-1366.

[11] Yao, Y., Li, D., and Yuan, Z., "Mill-Grinding Machining for Particle Reinforced Aluminum Matrix Composites," Proceedings of The Seventh International Conference on Progress of Machining Technology, Aviation Industry Press, pp. 258-263.

[12] Ferkel, H., and Mordike, B. L., 2001, "Magnesium strengthened by SiC nanoparticles," Materials Science and Engineering A, 298(1-2), pp. 193-199.

[13] He, F., Han, Q. and Jackson, M. J., 2008, "Nanoparticulate Reinforced Metal Matrix Nanocomposites," International Journal of Nanoparticles, 1(4), pp. 301-309.

[14] Poddar, P., Mukherjee, S. and Sahoo, K. L., 2009, "The Microstructure and Mechanical Properties of SiC Reinforced Magnesium Based Composites by Rheocasting Process," Journal of Materials Engineering and Performance, 18(7), pp. 849-855.

[15] An, L., Qu, J., Luo, J., Fan, Y., Zhang, L., Liu, J., Xu, C. and Blau, P. J. , 2011, "Aluminum nanocomposites having wear resistance better than stainless steel," Journal of Materials Research, 26 (19), pp. pp 2479-2483

[16] Prabhu, B., Suryanarayana, C., An, L., and Vaidyanathan, R., 2006, "Synthesis and characterization of high volume fraction Al-Al$_2$O$_3$ nanocomposite powders by high-energy milling," Materials Science and Engineering: A, 425(1-2), pp. 192-200.

[17] Charles, S., and Arunachalam, V. P., 2006, "Characterization of properties of cryogenically treated Al-SiC composites fabricated by powder metallurgy," Materials and Manufacturing Processes, 21(5), pp. 535-541.

[18] Reddy, S. U., Srikanth, N., Gupta, M., and Sinha, S. K., 2004, "Enhancing the Properties of Magnesium using SiC Particulates in Sub-micron Length Scale," Advanced Engineering Materials, 6(12), pp. 957-964.

[19] Cao, G., Konishi, H., and Li, X., 2008, "Mechanical Properties and Microstructure of Mg/SiC Nanocomposites Fabricated by Ultrasonic Cavitation Based Nanomanufacturing," Journal of Manufacturing Science and Engineering, 130(3), pp. 031105-031106.

[20] Lim, C. Y. H., Leo, D. K., Ang, J. J. S., and Gupta, M., 2005, "Wear of magnesium composites reinforced with nano-sized alumina particulates," Wear, 259(1-6), pp. 620-625.

[21] Amini, S., Ni, C., and Barsoum, M. W., 2009, "Processing, microstructural characterization and mechanical properties of a Ti_2AlC/nanocrystalline Mg-matrix composite," Composites Science and Technology, 69(3-4), pp. 414-420.

[22] Khorshid, M. T., Jahromi, S. A. J., and Moshksar, M. M., 2010, "Mechanical properties of tri-modal Al matrix composites reinforced by nano- and submicron-sized Al_2O_3 particulates developed by wet attrition milling and hot extrusion," Materials & Design, 31(8), pp. 3880-3884.

[23] Rajkovic, V., Bozic, D., and Jovanovic, M. T., 2008, "Properties of copper matrix reinforced with various size and amount of Al_2O_3 particles," Journal of Materials Processing Technology, 200(1-3), pp. 106-114.

[24] Tjong, S. C., 2007, "Novel Nanoparticle-Reinforced Metal Matrix Composites with Enhanced Mechanical Properties," Advanced Engineering Materials, 9(8), pp. 639-652.

[25] Zhang, H., Ramesh, K. T., and Chin, E. S. C., 2008, "A multi-axial constitutive model for metal matrix composites," Journal of the Mechanics and Physics of Solids, 56(10), pp. 2972-2983.

[26] Biner, S. B., and Hu, S. Y., 2009, "Simulation of damage evolution in discontinously reinforced metal matrix composites: A phase-field model," International Journal of Fracture, 158(2), pp. 99-105.

[27] Ilie, D. E., O'Donnell, B. P., McGarry, J. P., and McHugh, P. E., 2007, "Computational modelling of the extrusion of an Al-SiC metal matrix composite using macroscale and microscale methods," Journal of Strain Analysis for Engineering Design, 42(4), pp. 237-252.

[28] Aghdam, M. M., Gorji, M., and Falahatgar, S. R., 2009, "Interface damage of SiC/Ti metal matrix composites subjected to combined thermal and axial shear loading," Computational Materials Science, 46(3), pp. 626-631.

[29] Mahmoodi, M. J., Aghdam, M. M., and Shakeri, M., 2010, "Micromechanical modeling of interface damage of metal matrix composites subjected to off-axis loading," Materials and Design, 31(2), pp. 829-836.

[30] Xia, X., McQueen, H. J., and Zhu, H., 2002, "Fracture Behavior of Particle Reinforced Metal Matrix Composites," Applied Composite Materials, 9(1), pp. 17-31.

[31] Rabiei, A., Vendra, L., and Kishi, T., 2008, "Fracture behavior of particle reinforced metal matrix composites," Composites Part A: Applied Science and Manufacturing, 39(2), pp. 294-300.

[32] Manna, A., and Bhattacharayya, B., 2005, "Influence of machining parameters on the machinability of particulate reinforced Al/SiC-MMC," International Journal of Advanced Manufacturing Technology, 25(9-10), pp. 850-856.

[33] Muthukrishnan, N., Murugan, M., and Rao, K. P., 2008, "An investigation on the machinability of Al-SiC metal matrix composites using pcd inserts," International Journal of Advanced Manufacturing Technology, 38(5-6), pp. 447-454.

[34] Davim, J. P., Silva, J., and Baptista, A. M., 2007, "Experimental cutting model of metal matrix composites (MMCs)," Journal of Materials Processing Technology, 183(2-3), pp. 358-362.

[35] Kannan, S., Kishawy, H. A., and Deiab, I., 2009, "Cutting forces and TEM analysis of the generated surface during machining metal matrix composites," Journal of Materials Processing Technology, 209(5), pp. 2260-2269.

[36] Pramanik, A., Zhang, L. C., and Arsecularatne, J. A., 2008, "Machining of metal matrix composites: Effect of ceramic particles on residual stress, surface roughness and chip formation," International Journal of Machine Tools and Manufacture, 48(15), pp. 1613-1625.

[37] Pramanik, A., Zhang, L. C., and Arsecularatne, J. A., 2006, "Prediction of cutting forces in machining of metal matrix composites," International Journal of Machine Tools and Manufacture, 46(14), pp. 1795-1803.

[38] Dabade, U. A., and Joshi, S. S., 2009, "Analysis of chip formation mechanism in machining of Al/SiCp metal matrix composites," Journal of Materials Processing Technology, 209(10), pp. 4704-4710.

[39] Kwak, J. S., and Kim, Y. S., 2008, "Mechanical properties and grinding performance on aluminum-based metal matrix composites," Journal of Materials Processing Technology, 201(1-3), pp. 596-600.

[40] Basavarajappa, S., Chandramohan, G., and Davim, J. P., 2008, "Some studies on drilling of hybrid metal matrix composites based on Taguchi techniques," Journal of Materials Processing Technology, 196(1-3), pp. 332-338.

[41] Gaitonde, V. N., Karnik, S. R., and Davim, J. P., 2009, "Some studies in metal matrix composites machining using response surface methodology," Journal of Reinforced Plastics and Composites, 28(20), pp. 2445-2457.

[42] Palanikumar, K., Shanmugam, K., and Davim, J. P., 2010, "Analysis and optimisation of cutting parameters for surface roughness in machining Al/SiC particulate composites by PCD tool," International Journal of Materials and Product Technology, 37(1-2), pp. 117-128.

[43] Liu, X., DeVor, R. E., Kapoor, S. G., and Ehmann, K. F., 2004, "The Mechanics of Machining at the Microscale: Assessment of the Current State of the Science," Journal of Manufacturing Science and Engineering, 126(4), pp. 666-678.

[44] Vogler, M. P., DeVor, R. E., and Kapoor, S. G., 2003, "Microstructure-level force prediction model for micro-milling of multi-phase materials," Journal of Manufacturing Science and Engineering, 125(2), pp. 202-209.

[45] Chuzhoy, L., DeVor, R. E., and Kapoor, S. G., 2003, "Machining Simulation of Ductile Iron and Its Constituents, Part 2: Numerical Simulation and Experimental Validation of Machining," Journal of Manufacturing Science and Engineering, 125(2), pp. 192-201.

[46] Chuzhoy, L., DeVor, R. E., Kapoor, S. G., and Bammann, D. J., 2002, "Microstructure-Level Modeling of Ductile Iron Machining," Journal of Manufacturing Science and Engineering, 124(2), pp. 162-169.

[47] Chuzhoy, L., DeVor, R. E., Kapoor, S. G., Beaudoin, A. J., and Bammann, D. J., 2003, "Machining Simulation of Ductile Iron and Its Constituents, Part 1: Estimation of Material Model Parameters and Their Validation," Journal of Manufacturing Science and Engineering, 125(2), pp. 181-191.

[48] Pramanik, A., Zhang, L. C., and Arsecularatne, J. A., 2007, "An FEM investigation into the behavior of metal matrix composites: Tool-particle interaction during orthogonal cutting," International Journal of Machine Tools and Manufacture, 47(10), pp. 1497-1506.

[49] Dikshit, A., Samuel, J., DeVor, R. E., and Kapoor, S. G., 2008, "A Microstructure-Level Material Model for Simulating the Machining of Carbon Nanotube Reinforced Polymer Composites," Journal of Manufacturing Science and Engineering, 130(3), pp. 031110-031118.

[50] Dikshit, A., Samuel, J., DeVor, R. E., and Kapoor, S. G., 2008, "Microstructure-Level Machining Simulation of Carbon Nanotube Reinforced Polymer Composites---Part I: Model Development and Validation," Journal of Manufacturing Science and Engineering, 130(3), pp. 031114-031118.

[51] Dikshit, A., Samuel, J., DeVor, R. E., and Kapoor, S. G., 2008, "Microstructure-Level Machining Simulation of Carbon Nanotube Reinforced Polymer Composites---Part II: Model Interpretation and Application," Journal of Manufacturing Science and Engineering, 130(3), pp. 031115-031118.

[52] Zhang, Z., and Chen, D. L., 2006, "Consideration of orowan strengthening effect in particulate-reinforced metal matrix nanocomposites: A model for predicting their yield strength," Scripa Materialia, 54(7), pp. 1321-1326.

[53] Zhang, Z., and Chen, D. L., 2008, "Contribution of Orowan Strengthening Effect in Particulate-Reinforced Metal Matrix Nanocomposites," Materials Science and Engineering A, 483-484, pp. 148-152.

[54] Zhang, Z., and Chen, D. L., 2007, "Prediction of Fracture Strength in Al_2O_3/SiCp Ceramic Matrix Nanocomposites," Science and Technology of Advance Materials, 8(1-2), pp. 5-10.

[55] Lloyd, D. J., 1994, "Particle reinforced aluminium and magnesium matrix composites," International Materials Reviews, 39(1), pp. 1-23.

[56] Inem, B., and Pollard, G., 1993, "Interface structure and fractography of a magnesium-alloy, metal-matrix composite reinforced with SiC particles," Journal of Materials Science, 28(16), pp. 4427-4434.

[57] Fang, N., and Wu, Q., 2004, "A new methodology for modeling material constitutive behavior using an orthogonal machining test," Transactions of NAMRI/SME, 32, pp. 95-102.

[58] Liu, K., and Melkote, S. N., 2006, "Material Strengthening Mechanisms and Their Contribution to Size Effect in Micro-Cutting," Journal of Manufacturing Science and Engineering, 128(3), pp. 730-738.

[59] Lai, X., Li, H., Li, C., Lin, Z., and Ni, J., 2008, "Modelling and analysis of micro scale milling considering size effect, micro cutter edge radius and minimum chip thickness," International Journal of Machine Tools and Manufacture, 48(1), pp. 1-14.

[60] Dornfeld, D., Min, S., and Takeuchi, Y., 2006, "Recent Advances in Mechanical Micromachining," CIRP Annals - Manufacturing Technology, 55(2), pp. 745-768.

[61] Aramcharoen, A., and Mativenga, P. T., 2009, "Size effect and tool geometry in micromilling of tool steel," Precision Engineering, 33(4), pp. 402-407.

[62] Liu, J., Li, J., Ji, Y., and Xu, C., 2011, "Investigation on the Effect of SiC Nanoparticles on Cutting Forces for Micro-Milling Magnesium Matrix Composites," Proceedings of ASME International Manufacturing Science and Engineering Conference (MSEC2011), 2, pp. 525-536

[63] Kim, C.-J., Mayor, J. R., and Ni, J., 2004, "A Static Model of Chip Formation in Microscale Milling," Journal of Manufacturing Science and Engineering, 126(4), pp. 710-718.

[64] Kim, C. J., Bono, M., and Ni, J., 2002, "Experimental Analysis of Chip Formation in Micro-Milling," Transactions of NAMRI/SME, 30, pp. 1-8.

[65] Weule, H., Hüntrup, V., and Tritschler, H., 2001, "Micro-Cutting of Steel to Meet New Requirements in Miniaturization," CIRP Annals - Manufacturing Technology, 50(1), pp. 61-64.

[66] Liu, X., DeVor, R. E., and Kapoor, S. G., 2006, "An Analytical Model for the Prediction of Minimum Chip Thickness in Micromachining," Journal of Manufacturing Science and Engineering, 128(2), pp. 474-481.

[67] Komanduri, R., Chandrasekaran, N., and Raff, L. M., 1998, "Effect of tool geometry in nanometric cutting: a molecular dynamics simulation approach," Wear, 219(1), pp. 84-97.

[68] Komanduri, R., Chandrasekaran, N., and Raff, L. M., 1999, "Orientation Effects in Nanometric Cutting of Single Crystal Materials: An MD Simulation Approach," CIRP Annals - Manufacturing Technology, 48(1), pp. 67-72.

[69] Komanduri, R., Chandrasekaran, N., and Raff, L. M., 2000, "M.D. Simulation of nanometric cutting of single crystal aluminum-effect of crystal orientation and direction of cutting," Wear, 242(1-2), pp. 60-88.

[70] Inamura, T., Takezawa, N., and Kumaki, Y., 1993, "Mechanics and Energy Dissipation in Nanoscale Cutting," CIRP Annals - Manufacturing Technology, 42(1), pp. 79-82.

[71] Inamura, T., Takezawa, N., Kumaki, Y., and Sata, T., 1994, "On a Possible Mechanism of Shear Deformation in Nanoscale Cutting," CIRP Annals - Manufacturing Technology, 43(1), pp. 47-50.

[72] Ueda, K., Sugita, T., Hiraga, H., and Iwata, K., 1991, "A J-Integral Approach to Material Removal Mechanisms in Microcutting of Ceramics," CIRP Annals - Manufacturing Technology, 40(1), pp. 61-64.

[73] Ueda, K., and Manabe, K., 1992, "Chip Formation Mechanism in Microcutting of an Amorphous Metal," CIRP Annals - Manufacturing Technology, 41(1), pp. 129-132.

[74] Moriwaki, T., Sugimura, N., and Luan, S., 1993, "Combined Stress, Material Flow and Heat Analysis of Orthogonal Micromachining of Copper," CIRP Annals - Manufacturing Technology, 42(1), pp. 75-78.

[75] Jin, X., and Altintas, Y., 2011, "Slip-line field model of micro-cutting process with round tool edge effect," Journal of Materials Processing Technology, 211(3), pp. 339-355.

[76] Nasr, M. N. A., Ng, E. G., and Elbestawi, M. A., 2007, "Modelling the effects of tool-edge radius on residual stresses when orthogonal cutting AISI 316L," International Journal of Machine Tools and Manufacture, 47(2), pp. 401-411.

[77] Özel, T., and Zeren, E., 2007, "Finite element modeling the influence of edge roundness on the stress and temperature fields induced by high-speed machining," The International Journal of Advanced Manufacturing Technology, 35(3), pp. 255-267.

[78] Liu, K., and Melkote, S. N., 2007, "Finite element analysis of the influence of tool edge radius on size effect in orthogonal micro-cutting process," International Journal of Mechanical Sciences, 49(5), pp. 650-660.

[79] Salahshoor, M., and Guo, Y. B., 2011, "Cutting mechanics in high speed dry machining of biomedical magnesium-calcium alloy using internal state variable plasticity model," International Journal of Machine Tools and Manufacture, 51(7-8), pp. 579-590.

[80] Ding, H., and Shin, Y. C., 2011, "Dislocation Density-based Grain Refinement Modeling of Orthogonal Cutting of Commercially Pure Titanium," Proceedings of ASME International Manufacturing Science and Engineering Conference (MSEC2011), 2, pp. 89-98

[81] Atkins, T., 2009, Science and Engineering of Cutting - The Mechanics and Processes of Separating, Scratching and Puncturing Biomaterials, Metals and Non-Metals, Butterworth-Heinemann.

[82] Guo, Y. B., Wen, Q., and Horstemeyer, M. F., 2005, "An internal state variable plasticity-based approach to determine dynamic loading history effects on material property in manufacturing processes," International Journal of Mechanical Sciences, 47(9), pp. 1423-1441.

[83] Mulliken, A. D., and Boyce, M. C., 2006, "Mechanics of the rate-dependent elastic-plastic deformation of glassy polymers from low to high strain rates," International Journal of Solids and Structures, 43(5), pp. 1331-1356.

[84] Zhu, Y. P., Kannan, S., and Kishawy, H. A., 2004, "A model for orthogonal machining of metal matrix composite using finite element method," Proceedings of ASME 2004 International Mechanical Engineering Congress and Exposition (IMECE 2004), pp. 471-478

[85] Zhu, Y., and Kishawy, H. A., 2005, "Influence of alumina particles on the mechanics of machining metal matrix composites," International Journal of Machine Tools and Manufacture, 45(4-5), pp. 389-398.

[86] Li, Y., Ramesh, K. T., and Chin, E. S. C., 2004, "Comparison of the plastic deformation and failure of A359/SiC and 6061-T6/Al$_2$O$_3$ metal matrix composites under dynamic tension," Materials Science and Engineering A, 371(1-2), pp. 359-370.

[87] Li, Y., Ramesh, K. T., and Chin, E. S. C., 2007, "Plastic Deformation and Failure in A359 Aluminum and an A359-SiCp MMC under Quasistatic and High-strain-rate Tension," Journal of Composite Materials, 41(1), pp. 27-40.

[88] Dandekar, C. R., and Shin, Y. C., 2009, "Multi-step 3-D finite element modeling of subsurface damage in machining particulate reinforced metal matrix composites," Composites Part A: Applied Science and Manufacturing, 40(8), pp. 1231-1239.

[89] Jun, M. B. G., Liu, X., DeVor, R. E., and Kapoor, S. G., 2006, "Investigation of the Dynamics of Microend Milling---Part I: Model Development," Journal of Manufacturing Science and Engineering, 128(4), pp. 893-900.

[90] Malekian, M., Park, S. S., and Jun, M. B. G., 2009, "Modeling of dynamic micro-milling cutting forces," International Journal of Machine Tools and Manufacture, 49(7-8), pp. 586-598.

[91] Vogler, M. P., Kapoor, S. G., and DeVor, R. E., 2004, "On the modeling and analysis of machining performance in micro-endmilling, part II: Cutting force prediction," Journal of Manufacturing Science and Engineering, 126(4), pp. 695-705.

[92] Jun, M. B. G., DeVor, R. E., and Kapoor, S. G., 2006, "Investigation of the Dynamics of Microend Milling---Part II: Model Validation and Interpretation," Journal of Manufacturing Science and Engineering, 128(4), pp. 901-912.

[93] Kishawy, H. A., Kannan, S., and Balazinski, M., 2004, "An Energy Based Analytical Force Model for Orthogonal Cutting of Metal Matrix Composites," CIRP Annals - Manufacturing Technology, 53(1), pp. 91-94.

[94] Li, C., Lai, X., Li, H., and Ni, J., 2007, "Modeling of three-dimensional cutting forces in micro-end-milling," Journal of Micromechanics and Microengineering, 17(4), pp. 671-678.

[95] Perez, H., Vizan, A., Hernandez, J. C., and Guzman, M., 2007, "Estimation of cutting forces in micromilling through the determination of specific cutting pressures," Journal of Materials Processing Technology, 190(1-3), pp. 18-22.

[96] Wan, M., Zhang, W.-h., Tan, G., and Qin, G.-h., 2007, "New Cutting Force Modeling Approach for Flat End Mill," Chinese Journal of Aeronautics, 20(3), pp. 282-288.

[97] Wan, M., Zhang, W., Tan, G., and Qin, G., 2007, "New algorithm for calibration of instantaneous cutting-force coefficients and radial run-out parameters in flat end milling," Proceedings of the Institution of Mechanical Engineers, Part B: Journal of Engineering Manufacture, 221(6), pp. 1007-1019.

[98] Wan, M., Zhang, W. H., Qin, G. H., and Wang, Z. P., 2008, "Consistency study on three cutting force modelling methods for peripheral milling," Proceedings of the Institution of Mechanical Engineers, Part B: Journal of Engineering Manufacture, 222(6), pp. 665-676.

[99] Dang, J.-W., Zhang, W.-H., Yang, Y., and Wan, M., 2010, "Cutting force modeling for flat end milling including bottom edge cutting effect," International Journal of Machine Tools and Manufacture, 50(11), pp. 986-997.

[100] Newby, G., Venkatachalam, S., and Liang, S. Y., 2007, "Empirical analysis of cutting force constants in micro-end-milling operations," Journal of Materials Processing Technology, 192-193, pp. 41-47.

[101] Yun, W. S., and Cho, D. W., 2000, "An Improved Method for the Determination of 3D Cutting Force Coefficients and Runout Parameters in End Milling," The International Journal of Advanced Manufacturing Technology, 16(12), pp. 851-858.

[102] Uriarte, L., Azcarate, S., Herrero, A., Lopez De Lacalle, L. N., and Lamikiz, A., 2008, "Mechanistic modelling of the micro end milling operation," Proceedings of the Institution of Mechanical Engineers, Part B: Journal of Engineering Manufacture, 222(1), pp. 23-33.

[103] Bakkal, M., and Naksiler, V., 2009, "Cutting mechanics of bulk metallic glass materials on meso-end milling," Materials and Manufacturing Processes, 24(12), pp. 1249-1255.

[104] Afazov, S. M., Ratchev, S. M., and Segal, J., 2010, "Modelling and simulation of micro-milling cutting forces," Journal of Materials Processing Technology, 210(15), pp. 2154-2162.

[105] Altintas, Y., and Jin, X., 2011, "Mechanics of micro-milling with round edge tools," CIRP Annals - Manufacturing Technology, 60(1), pp. 77-80.

[106] Park, S., Kapoor, S. G., and DeVor, R. E., 2004, "Mechanistic Cutting Process Calibration via Microstructure-Level Finite Element Simulation Model," Journal of Manufacturing Science and Engineering, 126(4), pp. 706-709.

[107] Filiz, S., Ozdoganlar, O. B., and Romero, L. A., 2008, "An analytical model for micro-endmill dynamics," Journal of Vibration and Control, 14(8), pp. 1125-1150.

[108] Jun, M. B. G., Bourne, K., DeVor, R. E., and Kapoor, S. G., 2007, "Estimation of effective error parameters in high-speed micro-endmilling," International Journal of Machine Tools and Manufacture, 47(9), pp. 1449-1454.

[109] Dow, T. A., Miller, E. L., and Garrard, K., 2004, "Tool force and deflection compensation for small milling tools," Precision Engineering, 28(1), pp. 31-45.

[110] Al-Regib, E., Ni, J., and Lee, S.-H., 2003, "Programming spindle speed variation for machine tool chatter suppression," International Journal of Machine Tools and Manufacture, 43(12), pp. 1229-1240.

[111] Rahnama, R., Sajjadi, M., and Park, S. S., 2009, "Chatter suppression in micro end milling with process damping," Journal of Materials Processing Technology, 209(17), pp. 5766-5776.

[112] Mascardelli, B. A., Park, S. S., and Freiheit, T., 2008, "Substructure Coupling of Microend Mills to Aid in the Suppression of Chatter," Journal of Manufacturing Science and Engineering, 130(1), p. 011010.

[113] Li, J., Liu, J. and Xu, C., 2010, "Machinability Study of SiC Nano-Particles Reinforced Magnesium Nanocomposites During Micro-Milling Processes," Proceedings of ASME 2010 International Manufacturing Science and Engineering Conference (MSEC2010) 2, pp. 391-398

[114] Vogler, M. P., DeVor, R. E., and Kapoor, S. G., 2004, "On the Modeling and Analysis of Machining Performance in Micro-Endmilling, Part I: Surface Generation," Journal of Manufacturing Science and Engineering, 126(4), pp. 685-694.

[115] Wissmiller, D. L., and Pfefferkorn, F. E., 2009, "Micro end mill tool temperature measurement and prediction," Journal of Manufacturing Processes, 11(1), pp. 45-53.

[116] Hwang, J., Kompella, S., Chandrasekar, S., and Farris, T. N., 2003, "Measurement of Temperature Field in Surface Grinding Using Infra-Red (IR) Imaging System," Journal of Tribology, 125(2), pp. 377-383.

[117] Sahoo, P., 2008, "Fractal dimension modelling of surface profile and optimisation in CNC end milling using response surface method," International Journal of Manufacturing Research, 3(3), pp. 360-377.

[118] Thangavel, P., 2008, "An experimental investigation on the effect of turning parameters on surface roughness," International Journal of Manufacturing Research, 3(3), pp. 285-300.

[119] Manna, A., and Bhattacharayya, B., 2003, "A study on machinability of Al/SiC-MMC," Journal of Materials Processing Technology, 140(1–3), pp. 711-716.

[120] Zhang, Z. F., Zhang, L. C., and Mai, Y.-W., 1995, "Particle effects on friction and wear of aluminium matrix composites," Journal of Materials Science, 30(23), pp. 5999-6004.

[121] El-Gallab, M., and Sklad, M., 1998, "Machining of Al/SiC particulate metal-matrix composites. Part I: Tool performance," Journal of Materials Processing Technology, 83(1-3), pp. 151-158.

[122] Chawla, N., Deng, X., and Schnell, D. R. M., 2006, "Thermal expansion anisotropy in extruded SiC particle reinforced 2080 aluminum alloy matrix composites," Materials Science and Engineering: A, 426(1-2), pp. 314-322.

[123] Mabrouki, T., Girardin, F., Asad, M., and Rigal, J.-F., 2008, "Numerical and experimental study of dry cutting for an aeronautic aluminium alloy (A2024-T351)," International Journal of Machine Tools and Manufacture, 48(11), pp. 1187-1197.

[124] Özel, T., 2006, "The influence of friction models on finite element simulations of machining," International Journal of Machine Tools and Manufacture, 46(5), pp. 518-530.

[125] Childs, T. H. C., and Maekawa, K., 1990, "Computer-aided simulation and experimental studies of chip flow and tool wear in the turning of low alloy steels by cemented carbide tools," Wear, 139(2), pp. 235-250.

[126] Dirikolu, M. H., Childs, T. H. C., and Maekawa, K., 2001, "Finite element simulation of chip flow in metal machining," International Journal of Mechanical Sciences, 43(11), pp. 2699-2713.

[127] Shi, J., and Liu, C. R., 2004, "The influence of material models on finite element simulation of machining," Journal of Manufacturing Science and Engineering, 126(4), pp. 849-857.

[128] Litonski, J., 1977, "Plastic flow of a tube under adiabatic torsion," Bulletin de l'Académie Polonaise des Sciences. Série des Sciences Techniques, 25(1), pp. 7-14.

[129] Batra, R. C., 1988, "Steady state penetration of thermoviscoplastic targets," Computational Mechanics, 3(1), pp. 1-12.

[130] Lei, S., Shin, Y. C., and Incropera, F. P., 1999, "Material Constitutive Modeling Under High Strain Rates and Temperatures Through Orthogonal Machining Tests," Journal of Manufacturing Science and Engineering, 121, pp. 577-585.

[131] Johnson, G. R., and Cook, W. H., 1983, "A Constitutive Model and Data for Metals Subjected to Large Strains, High Strain rate, and Temperatures," International Symposium on BallisticsThe Hauge, The Netherlands, pp. 1-7.

[132] Bodner, S. R., and Black, J. T.,, 1975, "Constitutive Equations for Elastic-Viscoplastic Strain-Hardening Materials," Journal of Applied Mechanics, 56, pp. 385-389.

[133] Huang, J. M., and Black, J. T., 1996, "An Evaluation of Chip Separation Criteria for the FEM Simulation of Machining," Journal of Manufacturing Science and Engineering, 118(4), pp. 545-554.

[134] Zhang, L., 1999, "On the separation criteria in the simulation of orthogonal metal cutting using the finite element method," Journal of Materials Processing Technology, 89-90, pp. 273-278.

[135] Teng, X., and Wierzbicki, T., 2006, "Evaluation of six fracture models in high velocity perforation," Engineering Fracture Mechanics, 73(12), pp. 1653-1678.

[136] Zorev, N. N., 1963, "Inter-relationship between shear processes occurring along tool face and shear plane in metal cutting," International Research in Production Engineering, ASMENew York, pp. 42-49.

[137] Zhang, X., Wu, S., Wang, H., and Liu, C. R., 2011, "Predicting the Effects of Cutting Parameters and Tool Geometry on Hard Turning Process Using Finite Element Method," Journal of Manufacturing Science and Engineering, 133(4), p. 041010.

[138] Li, K., Gao, X. L., and Sutherland, J. W., 2002, "Finite element simulation of the orthogonal metal cutting process for qualitative understanding of the effects of crater wear on the chip formation process," Journal of Materials Processing Technology, 127(3), pp. 309-324.

[139] Shi, J., and Liu, C. R., 2006, "On predicting chip morphology and phase transformation in hard machining," The International Journal of Advanced Manufacturing Technology, 27(7), pp. 645-654.

[140] Shih, A. J., 1995, "Finite element simulation of orthogonal metal cutting," Journal of Engineering for Industry, Transactions of the ASME, 117(1), pp. 84-93.

[141] Ng, E.-G., and Aspinwall, D. K., 2000, "Hard part machining AISI H13 (approximately 50 HRC) using AMBORITE AMB90: A finite element modelling approach," Industrial Diamond Review, 60(587), pp. 305-310.

[142] Johnson, G. R., and Cook, W. H., 1985, "Fracture characteristics of three metals subjected to various strains, strain rates, temperatures and pressures," Engineering Fracture Mechanics, 21(1), pp. 31-48.

[143] Hillerborg, A., Modéer, M., and Petersson, P. E., 1976, "Analysis of crack formation and crack growth in concrete by means of fracture mechanics and finite elements," Cement and Concrete Research, 6(6), pp. 773-781.

[144] Atkins, A. G., 2003, "Modelling metal cutting using modern ductile fracture mechanics: quantitative explanations for some longstanding problems," International Journal of Mechanical Sciences, 45(2), pp. 373-396.

[145] Wilkins, M. L., Streit, R. D., and Reaugh, J. E., 1980, "Cumulative-strain-damage model of ductile fracture: simulation and prediction of engineering fracture tests," No. UCRL-53058, Lawrence Livermore National Laboratory, CA, USA.

[146] Wilkins, M. L., 1978, "Mechanics of penetration and perforation," International Journal of Engineering Science, 16(11), pp. 793-807.

[147] Bao, Y., and Wierzbicki, T., 2004, "A Comparative Study on Various Ductile Crack Formation Criteria," Journal of Engineering Materials and Technology, 126(3), pp. 314-324.

[148] Bil, H., Kılıç, S. E., and Tekkaya, A. E., 2004, "A comparison of orthogonal cutting data from experiments with three different finite element models," International Journal of Machine Tools and Manufacture, 44(9), pp. 933-944.

[149] Aurich, J. C., and Bil, H., 2006, "3D Finite Element Modelling of Segmented Chip Formation," CIRP Annals - Manufacturing Technology, 55(1), pp. 47-50.

[150] Ceretti, E., Lucchi, M., and Altan, T., 1999, "FEM simulation of orthogonal cutting: serrated chip formation," Journal of Materials Processing Technology, 95(1–3), pp. 17-26.

[151] Bao, Y., and Wierzbicki, T., 2004, "On fracture locus in the equivalent strain and stress triaxiality space," International Journal of Mechanical Sciences, 46(1), pp. 81-98.

[152] Bao, Y., and Wierzbicki, T., 2005, "On the cut-off value of negative triaxiality for fracture," Engineering Fracture Mechanics, 72(7), pp. 1049-1069.

[153] Bai, Y., and Wierzbicki, T., 2010, "Application of extended Mohr–Coulomb criterion to ductile fracture," International Journal of Fracture, 161(1), pp. 1-20.

[154] Edward M. Trent, P. K. W., 2010, Metal Cutting, Butterworth-Heinemann, Elsevier Inc.

[155] Ulacia, I., Salisbury, C. P., Hurtado, I., and Worswick, M. J., 2011, "Tensile characterization and constitutive modeling of AZ31B magnesium alloy sheet over wide range of strain rates and temperatures," Journal of Materials Processing Technology, 211(5), pp. 830-839.

[156] Ye, H., and Liu, X., 2004, "Review of recent studies in magnesium matrix composites," Journal of Materials Science, 39(20), pp. 6153-6171.